2014

NANOMETER-SCALE MEMBRANE ELECTRODE SYSTEMS FOR ACTIVE PROTEIN SEPARATION, ENZYME IMMOBILIZATION AND CELLULAR ELECTROPORATION

Zhiqiang Chen
University of Kentucky, chenzhiqiang86@gmail.com

STUDENT AGREEMENT:

I represent that my thesis or dissertation and abstract are my original work. Proper attribution has been given to all outside sources. I understand that I am solely responsible for obtaining any needed copyright permissions. I have obtained needed written permission statement(s) from the owner(s) of each third-party copyrighted matter to be included in my work, allowing electronic distribution (if such use is not permitted by the fair use doctrine) which will be submitted to UKnowledge as Additional File.

I hereby grant to The University of Kentucky and its agents the irrevocable, non-exclusive, and royalty-free license to archive and make accessible my work in whole or in part in all forms of media, now or hereafter known. I agree that the document mentioned above may be made available immediately for worldwide access unless an embargo applies.

I retain all other ownership rights to the copyright of my work. I also retain the right to use in future works (such as articles or books) all or part of my work. I understand that I am free to register the copyright to my work.

REVIEW, APPROVAL AND ACCEPTANCE

The document mentioned above has been reviewed and accepted by the student's advisor, on behalf of the advisory committee, and by the Director of Graduate Studies (DGS), on behalf of the program; we verify that this is the final, approved version of the student's thesis including all changes required by the advisory committee. The undersigned agree to abide by the statements above.

Zhiqiang Chen, Student

Dr. Dibakar Bhattacharyya, Major Professor

Dr. Fuqian Yang, Director of Graduate Studies

NANOMETER-SCALE MEMBRANE ELECTRODE SYSTEMS FOR ACTIVE PROTEIN SEPARATION, ENZYME IMMOBILIZATION AND CELLULAR ELECTROPORATION

DISSERTATION

A dissertation submitted in partial fulfillment of the requirements for the degree of Doctor of Philosophy in the College of Engineering at the University of Kentucky

By

Zhiqiang Chen

Lexington, Kentucky

Co-Directors: Dr. Dibakar Bhattacharyya, Professor of Chemical Engineering
and Dr. Bruce Hinds, Professor of Materials Engineering

Lexington, Kentucky

2014

ABSTRACT OF DISSERTATION

NANOMETER-SCALE MEMBRANE ELECTRODE SYSTEMS FOR ACTIVE PROTEIN SEPARATION, ENZYME IMMOBILIZATION AND CELLULAR ELECTROPORATION

Automated and continuous processes are the future trends in downstream protein purification. A functionalized nanometer-scale membrane electrode system, mimicking the function of cell wall transporters, can selectively capture genetically modified proteins and subsequently pump them through the system under programmed voltage pulses. Numerical study of the two-step pulse pumping cycles coupled with experimental His-GFP releasing study reveals the optimal 14s/1s pumping/repel pulse pumping condition at 10 mM bulk imidazole concentration in the permeate side. A separation factor for GFP: BSA of 9.7 was achieved with observed GFP electrophoretic mobility of 3.1×10^{-6} cm^2 s^{-1} V^{-1} at 10 mM bulk imidazole concentration and 14 s/1 s pumping/repel duration. The purification of His_6-OleD Loki variant directly from crude *E. coli* extracts expression broth was demonstrated using the pulse pumping process, simplifying the separation process as well as reducing biopharmaceutical production costs. The enzymatic reactions showed that His_6-OleD Loki was still active after purification.

A nanoporous membrane/electrode system with directed flow carrying reagents to sequentially attached enzymes to mimic nature's enzymes-complex system was demonstrated. The substrates residence time on the immobilized enzyme can be precisely controlled by changing the pumping rate and thereby prevent a secondary hydrolysis reaction. Immobilized enzyme showed long term storage longevity with activity half-life of 50 days at 4℃ and the ability to be regenerated. One-step immobilization and purification of His-tagged OleD Loki variant directly from expression broth, yielded 98% Uridine Diphosphate glycosylation and 80% 4-methylumbelliferone glycosylation conversion efficiency for the sequential reaction.

A flow-through electroporation system, based on a novel membrane/electrode design, for the delivery of membrane-impermeant molecules into Model Leukocyte cells was demonstrated. The ability to apply low voltage between two short distance electrodes

contributes to high cell viability. The flow-through system can be easily scaled-up by varying the micro-fluidic channel geometry and/or the applied voltage pulse frequency. More importantly, the system allows the electrophoretical pumping of molecules from the reservoir across the membrane/electrode system to the micro-fluidic channel for transfection, which reduces large amount of reagents used.

KEYWORDS: Nanoporous electrode, Dynamic membrane, Protein separation, Enzyme immobilization, Cell electroporation

Zhiqiang Chen

Student's Signature

July 25, 2014

Date

NANOMETER-SCALE MEMBRANE ELECTRODE SYSTEMS FOR ACTIVE PROTEIN SEPARATION, ENZYME IMMOBILIZATION AND CELLULAR ELECTROPORATION

By

Zhiqiang Chen

Dr. Dibakar Bhattacharyya and Dr. Bruce Hinds

Co-Directors of Dissertation

Dr. Fuqian Yang

Director of Graduate Studies

July 25, 2014

Dedicated to my families

ACKNOWLEDGEMENTS

First, I would like to thank my advisor, Prof. Bruce J. Hinds, for the opportunity to work in his lab on three projects that continually challenged and expanded my skills as a scientist. His insightful experience and assistance have always been helpful to my research. My appreciation for his unwavering support will not be forgotten.

I am also very grateful to my committee members Prof. Dibakar Bhattacharyya, Prof. Hainsworth Shin and Prof Yang-Tse Cheng for their excellent suggestions and guidance during my PhD study. I am also thankful for Prof. Anne-Frances Miller willing to serve as the outside examiner.

I would like to thank all the great people I have collaborated with- Prof. Hainsworth Shin, Prof. Jon Thorson, Prof. Chris Richards, Dr. Jianjun Zhang, Dr Shanteri Singh, Dr. Xinghua Sun, Michael Akenhead, Harrison Sapper, Ashley Fox and Ryan R. Hughes.

The help and discussion from our group mates Dr. Ji Wu, Dr. Xinhua Sun, Dr. Xin Su, Dr. Xin Zhan, Dr. Rupam Sarma, Tao Chen, Jingyuan Yao and Nicholas Linck are greatly appreciated.

Funding support from National Institutes of Health (NIH) is appreciated. I would also like to thank the training and facilities provided by Electron Microscopy Center and Center for Nanoscale Science and Engineering (CeNSE).

Finally, I would like to thank all the friends I made in Lexington to make my life in Lexington memorial.

TABLE OF CONTENTS

LIST OF TABLES

LIST OF FIGURES

Chapter 1 : Introduction

1.1 Synthetic Membranes

Synthetic membranes have found wide-ranging applications in water desalination, gas separations, drug delivery, and hemodialysis since the middle of last century [1]. The history of membrane industry is very short; however, the market is large and is growing more than 10% per year. The membrane market is about 15 billion in 2012 and is estimated to double by 2020. Basically, there are three major commercially available synthetic membranes types according to the production process; polymeric membranes, "track-etch" membranes and ceramic membranes. Polymeric membranes are the most widely used membrane in industry due to their high performance and low relative cost. Many different polymers such as cellulose acetate, polyvinylchloride (PVC), polytetrafluoroethylene (PTFE), polyvinylidene fluoride (PVDF), polyethylene (PE) have been used for polymeric membranes synthesis. These polymer-based membranes surfaces are often modified with different chemistry to further increase performance and used for various applications [2].

Water desalination is the major application of polymeric membranes in industry. Water is one of the most precious resources in the world. However, countries like Singapore have little access to water. Desalination of seawater is a good choice for such countries. Traditional desalination method is vacuum distillation. Many vacuum distillation plants have been built around the world though it is a relatively expensive desalination method. Desalination using membrane technology is an alternative approach, and in fact it's a more economical method [3]. Reverse osmosis membranes have been extensively used

for desalination [4]. Reverse osmosis (RO) works by applying a pressure to overcome osmotic pressure and push water pass through the semipermeable membrane. Only water can pass through the RO membrane, all other molecule and ions can't pass through the RO membrane. Polysulfone open support membranes coated with aromatic polyamides using an interfacial polymerization reaction to form a thin skin with 'free volume' that supports selective water transport. The next most significant application of polymeric membranes is in gas separation area where gasses are also selectively transported through 'free' volume of the polymer skin layer. The global warming calls for the capture of CO_2 in coal plant. Membrane technologies have been extensively studied for the capture of CO_2 from coal-fired power-plant flue gas [5]. Also, polymeric membranes have been used for food and pharmaceutical industry to remove impurities from products.

One disadvantage of polymeric membranes is their randomly distributed pore size, limiting their application in precise size-based filtration. "Track-etch" membranes, such as Polycarbonate track-etch (PCTE), are made from thin film material *via* track-etch method. A two-step method combining charged particle bombardment and chemical etching is used to create discrete pores in the "Track-etch" membranes. The pore sizes of "Track-etch" membranes are well-defined; however, the porosities are very low, limiting their applications in large-scale filtration. Ceramic membranes are made from inorganic materials (such as alumina oxides) can often tolerate extreme solvent conditions (extreme PH and temperature). Specifically, porous aluminum oxide membranes made from two-step anodization process have high pore density and high level of pore ordering. Typically the first step is carried out on ~1 μm thick aluminum films in 0.3M oxalic acid solution at room temperature using Pt as a counter electrode. The anodization was

conducted under a constant voltage mode (40 V) for approximately 4 min. Then the aluminum samples were etched in 0.3 M phosphoric acid in order to enlarge the pore depth [6]. The pore size of AAO membranes can be controlled by changing phosphoric etching time as shown in Figure 1.1.

The working mechanism of the synthetic membrane is very simple: A membrane acts as a selective barrier, separating two different regions and allowing some matter to pass through, but not others [2]. Traditional synthetic membranes carry out simple passive transport under different driving forces such as pressure, concentration gradient, temperature *etc.*, resulting in low selectivity and high energy consumption. Concentration polarization, which is concentration build-up phenomenon on the membrane surface caused by the different permeation rate of mixture components through the membrane, and membrane fouling are two other major challenges for these passive transport synthetic membranes [7].

1.2 Biological Membranes

Biological membranes, however, are highly complicated transporters that have the ability to actively pump specific chemicals or transport specific signals through the membrane channels at dramatic rate, which is very import for cellular function [8]. Biological membrane is composed of a bulk phospholipid bilayer with various imbedded protein in a fluid mosaic arrangement. The transmembrane potassium channels can specifically regulate the transport of potassium by changing voltage, which are of vital importance in the returning the depolarized cell to a resting state [9]. Another example is nuclear pore complex regulating the transport of mRNA and proteins across the nuclear[10].

Also, insects detect pheromones by transport stimulant odorant molecules through lipid-coated nanopores. The waxy fluid lipid coated nanopores act as receptor chemistry on the surface of insect antennae, capturing and concentrating the pheromones ligand and delivering them to the inner pore tubules dispenser which can facilitate the transport of pheromones [11, 12]. Figure 1.2 shows one example of active transport process in cell membrane [13]. First, the molecules attach to the binding point of the transport protein in the cell membrane. The bottom of the transport protein is closed so that no other molecule can pass through the membrane. Second, ATP attached to the bottom transport protein to open it and deposit the molecule inside the cell. Finally, the transport reset to original state for next transport process. From this active biological membrane transport process we can see that the keys to biological protein channels are (1) selective receptor chemistry at the pore entrance, (2) a mechanism for fast fluid flow or mass-transport, and (3) signal chemistry at the exit side of protein to activate the channel [14, 15]. In particular, can we develop a platform that allows the sequential actuation of gatekeeper molecules to give active transport?

1.3 Bio-inspired Membranes

The advances in nanotechnology and synthetic biology make it possible to study and mimic biological membrane through integration of engineering and biology, which in turn can facilitate the understand of biology systems. Key to mimic biological pore is a nano-scale pore scaffold that can be easily modified with different chemistry. Many different methods have been developed to create such nano-scale pore scaffold. Li and co-workers[16] successfully created single nanopores in thin silicon nitride membrane using ion beam sculpting. Storm and co-workers [17] used electron beams to create sub-

nanometer pore diameters. A 20 nm pore is initially created within silicon membrane using electron-beam lithography followed by anisotropic etching. The pore is then further treated with thermal oxidation to shrink the pore to a single-nanometer resolution. However, this method is hard to produce large quantity of pores within the silicon membrane.

Different types of bio-inspired nano-scale pores have been developed to mimic biological pores and channels. Single nanopore coated with lipid bilayer was recently reported to mimic lipid coated channels in olfactory system of insects, which can pre-concentrate odorant molecules from the environment and transport deposit them inside the coated nanochannel (Figure 1.3) [12]. There are several advantages of this lipid coated SiN nanopores. First, absorption of non-specific binding molecules to the lipid coated membranes is minimal compared to bare membrane; Second, Biotoin groups can be attached to the lipid bialyer to specifically capture avidin-functional molecules. Lastly, the translocation speed of the molecules through the nanopore can be controlled by changing the viscosity of the lipid-bilayer. The nuclear pore complex consists of a very large protein channel that can be found at all eukaryotic cells. Nuclear pore complex have the ability to transport single strand DNA at an enhanced speed under the help of transport carrier. Caspi and co-workers [18] modified porous membranes inside wall with polyisopro-pylacrylamide (pNIPAM) to mimic the nuclear pore complex, and demonstrated that single strand DNA moves much faster in the pNIPAM modified channel compared to bare channel.

Importantly, studies have also been carried out to mimic ion channels. Ionic channel consists of membrane proteins that have the ability to facilitate the ion transport across

the membrane by regulating transmembrane voltage and steric binding. The mechanism of ion transported through the channel is complicated. The ion channels consist of a single polypeptide that has four homologous domains. Every domain has six membrane spanning alpha helices including the voltage sensing helix, S4. The sensing helix has a high density of cationic peptides such that high positive potential (cation density) outside the cell repels the helix pushing it to block the channel. To open the channel, the helix will undergo a conformational change to allow ion flow when the cell interior is depolarized. Nevertheless, many different biomimetic ion channels have been developed. Tian and co-workers [19] modified polymeric nanochannel with zinc finger peptide. Upon adding zinc ion, the zinc fingers fold to finger-like conformations, resulting in a pore diameter increase (Figure 1.4). Study has also been carried on artificial pH-responsive ion channels. Yameen and co-workers [20] modified solid-state nanopores with pH-responsive poly(4-vinyl pyridine) brushes. The change of the solution pH will change the polymer conformation and thus resulting 'on' and 'off' state of these nanopores, which is monitored by current signal. This mimics the biological channel by switching from an "off" state to an "on" state in response to pH drop.

Carbon nanotube (CNT) membranes also offer an exciting platform to mimic natural protein channels due to (1) enhanced fluid flow within CNT, (2) ability to place receptor chemistry at the entrance to pores, and (3) being conductive allowing for electrochemical transformation and application of electric field [21, 22, 23, 24, 25]. Monolayer 'gatekeeper' activity to open and close pore entrances with charged 'paddles' demonstrated small ion rectification with applied trans-membrane bias, closely mimicking ion channels. Biochemical-reaction induced switching of ionic transport

through CNT membranes was also shown to mimic biological membranes [26]. In this study, the pore entrances of CNT membrane were covalently functionalized with a desthiobiotin derivative that bind to streptavidin protein at one of 4 well-defined sites. The ionic flux through CNT membranes decreased upon pore blockage by streptavidin protein. The ionic flux was recovered by the addition of biotin solution, which is a stronger binding agent than desthiobiotin towards streptavidin, and released the protein hindrance at the pore entrance. Hinds and coworkers [27] also showed that synthetic CNT membranes can be used to mimicking protein channels regulated by phosphorylation enzymatic (ATP cycle) reactions at the pore entrance.

1.4 Aluminum Oxide Membranes for Biopharmaceutical Applications

There are large-scale applications in mimicking active transport of biological membranes such as drug delivery, chemical separations and sensing. Although CNT membranes shows great promising in mimicking the active transport of biological membranes due to fast fluid core and monolayer gate-keeper chemistry, the low porosity (~0.01%) limits its use in large-scale chemical separations. Aluminum Oxide (AAO) Membranes are commercial available membrane with high porosity (50%) and tight pore size control (+/- 20%) within a range of 20-200 nm. The larger pore size of AAO compared to CNTs (1-7 nm i.d.) is a better size range when dealing with large proteins and other biomolecules ~10nm diameter. The membrane also exhibits low protein binding, has minimal auto-fluorescence, is nontoxic, and supports cellular growth (Whatman), thus offering an attractive platform for biopharmaceutical and biomedical applications.

Porous substrates such as AAO membranes have gained increased attentions for biosensor applications. Stephan and co-workers [28] recently reported a binding assay for small molecules based on the reflectivity change of a porous transparent film upon immobilization of absorbing substrates on the pore walls. Dhathathreyan [29] also reported the real-time monitoring of invertase activity immobilized in nanoporous AAO substrates. Immobilization of and trapping of invertase the porous wall structure was studied using confocal laser scanning microscopy showing excellent correlation with surface plasmon spectroscopy. The enzymatic reactions were carried out in a continuous flow cell apparatus with high enzyme activity (4.49×10^5 M^{-1} s^{-1})

AAO membranes have also been extensively studied for protein purifications. Osmanbeyoglu and co-workers [30] reported the successful fabrication of AAO membrane with narrow pore size distribution (20-30 nm diameters) by anodizing aluminums films on silicon substrates. This membrane showed the ability to separate similar size proteins based on electrostatic interaction with the anionic membrane surface. Porous membrane absorbers are also attractive platforms for efficient affinity protein purifications. However, one major disadvantage of these membrane absorbers is that their low surface area causes low binding capacity compared to chromatography columns with micro-scale porous bead packing. Bruening and co-workers [31] modified AAO membrane with poly (2-hydroxyethyl methacrylate) (PHEMA) brushes, followed by the adding of NTA-Ni^{2+} complex. This brush modified AAO membrane allows purification of polyhistidine-tagged ubiquitin (HisU) in less than half an hour with a binding capacity of 120 mg of HisU/cm^3 of porous alumina membrane.

Pore size control and surface modification would enable enormous applications of AAO membranes in bio-separation and biosensor. Gold electroless plating on AAO membranes show promise for use as highly selective filters for membrane-based separations. However, most of the work to date was focused on gold nanotubes fabrication by electroless deposition of gold within track-etched polymeric filtration membranes. Martin and co-workers have been exploring applications of gold nanotube membranes prepared via a template method [32, 33, 34, 35, 36]. These membranes were prepared by electroless deposition of Au within the whole channel of polycarbonate template membranes. Briefly, the template membrane was incubated with $SnCl_2$ first to deposit Sn on the membrane. The membrane was then treated with $AgNO_3$, followed by gold-plating solution. By carefully controlling the plating pH and plating duration, it's possible to obtain uniform gold nanotube within the polycarbonate membranes. The outside diameter of gold nanotube is determined by the inside diameter of the polycarbonate template. The inner diameter of gold nanotube can be controlled by changing the electro-less plating at will. Using this gold nanotube membranes, Martin and co-workers demonstrated the size-based protein separation in Poly (ethylene glycol)-Derivatized Gold Nanotubule Membranes33[33].

Despite the systematic study of gold nanotube within the track-etched polycarbonate filter, the track-etched suffered from very low porosity (<1%), resulting very low flux. In contrast, AAO membranes are very popular commercial available templates with high porosities (~50%). However, few studies [34] have been carried out on the electroless plating of gold within the pores of these membranes. This is because the current electroless plating method doesn't work within AAO walls. Gold electroless plating on

the AAO membrane pore entrance and exit, however, hasn't been studied [37]. Electro-less plating on the pore entrance of AAO membranes (Figure 1.5) has several benefits. First, the surface of gold can be easily functionalized with different chemistry including selective receptor chemistry. Second, voltage can be applied on this gold electrode to facilitate the ion transportation within the AAO membrane with relatively high electric fields across the 60um thick film. Third, the pore size of AAO membrane can be easily controlled by changing the electro-less plating time onto the initial sputtered Au seed layer. Of particular importance is to tune the size of pores to match expensive/important targets such as proteins and enzymes.

The functionalization of AAO membrane pore entrance would enable numerous applications. Although it is difficult to have a precise monolayer at the pore entrance (as can be done in CNT membranes), the Au can be localized to the top 20 nm of the membrane surface and pore entrances by evaporation thin film deposition. The gold Electro-less plating reactions will only form on the sputtered gold seed. Electro-less plating [38] was accomplished in 50 mM pH 7.0 phosphate buffer containing 1.6 mM sodium gold (I) thiosulfate and 2.68 mM ascorbic acid. The oxidization and reduction reactions are given by

$$C_6H_8O_6 \longrightarrow C_6H_6O_6 + 2e^- + 2H^+$$

$$Au(S_2O_3)_2^{3-} + e^- \rightleftharpoons Au + 2S_2O_3^{2-}$$

1.5 Protein purification methods

The history of protein purification can be dated back to 1789, when Antoine Foucroy first use precipitation method to separate substances from plants that are similar to egg

white. In 1840, Felix Hoppe-seyler reported the first crystallization of hemoglobin. Later in 1889, Franz Hofmeister also purified hen egg-white albumin through crystallization. Precipitation and Crystallization were the only available protein separation methods until the beginning of 20^{th} century [39]. These two methods still remain as important purification methods. Chromatography and electrophoresis methods were developed in the next decades. Chromatography is a separation and analysis method based on different interaction of substrates with the column matrix. Ionic exchange chromatography (IEC), hydrophobic interaction chromatography (HIC) and size exclusion chromatography (SEC) are three major chromatography methods used today for three-stage purification strategy (Capture, intermediate purification and polishing).

With the development of biotechnology, genetically engineered therapeutic proteins are becoming more important for bimolecular treatment. The ability to fuse affinity tag into the recombinant protein promotes the development of affinity chromatography (AC). Poly-histidine, as the most often used tag, is often fused into the recombinant protein for quick and efficient purification from cell crude lysate using immobilized metal ion affinity chromatography. In 1982, fast protein liquid chromatography (FPLC) was introduced by Pharmacia (Now GE healthcare), which greatly benefits the small-scale laboratory protein purification for various studies. Generic purification methods based on affinity tag fused into the protein has revolutionized protein purification, making today's protein purification easily and efficiently. However, for the clinical protein study, affinity chromatography alone cannot provide sufficient purity, and other polishing steps are needed such as IEC, HIC and SEC. Also, protein stability after purification needed to be

considered as this is very important for formulation study. In the following paragraphs, various chromatography methods will be discussed in detail.

1.5.1 Ionic Exchange Chromatography

Ionic exchange chromatography separates proteins based on the different surface charges [40]. Typically, targeted protein will bind to the charged chromatography media and be retained for subsequent release. However, impurity can bind to the charged chromatography media and need to be removed. Proteins consist of various amino acids which has different *pKa*. These amino acids will determine the finial structure of proteins and also contribute to the net surface charges. Proteins with different surface charges will have different interactions with the charged chromatography.

Every protein has different *isoelectric point (pI)* due to different component of amino acids. When the pH of the solution is higher than the *pI*, protein will show negative charge and can bind to positive charged chromatography. Here the IEC is called cation exchange chromatography. When the pH of the solution is lower than the *pI*, protein will show negative charge and can bind to negative charged chromatography. Here the IEC is called anion exchange chromatography. When the pH of the solution is equal to the *pI*, protein will have no change and will not interact with the chromatography medium.

There are usually four steps in an IEC process. First, the chromatography medium is equilibrated with start buffer; in the second sample loading step, charged proteins bind to the ionic groups of the medium and get concentrated. Impurities won't bind to the medium and are eluted after sample injection. Third, the ionic strength of the solution is

increased to compete with the bound proteins and release the protein. This can be achieved through gradient elution or step elution. Finally, the column is re-equilibrated.

IEC is a very powerful protein purification method that can be used in any part of multi-step purification procedure. In a three stage purification strategy, IEC is often used in the first step to remove any other impurities and opposite charged proteins followed by HIC and SEC.

1.5.2 Hydrophobic Interaction Chromatography

Hydrophobic interaction chromatography separates proteins based on interactions between protein and hydrophilic matric surface [41]. HIC is often used in the second step of the three-stage purification strategy (Intermediate purification). After the first stage-Capture (often with IEC), HIC is often used to remove other bulk contaminants.

There are also four steps during the HIC purification. First, the chromatography medium is equilibrated with start buffer; in the second sample loading/application step, proteins bind to the hydrophobic medium surface in high salt concentration (typically 1 to 2 M ammonium sulfate). Third, the ionic strength of the solution is lowered release the bound protein. This can be achieved through gradient elution or step elution. Finally, the column is re-equilibrated with low ionic strength buffer.

1.5.3 Size Exclusion Chromatography

Size exclusion chromatography separates proteins based on protein molecular size difference [42]. Unlike HIC and IEC, SEC is a non-binding separation method. Separation is based on the different travel rate through the chromatography medium. The

chromatography medium is composed of porous beads. Small protein can diffuse into these porous beads pore thus taking longer time to travel through the column. Large proteins can't diffuse into these porous beads pore thus taking lower time to travel through the column. As a result, large proteins elute first and small proteins elute last.

Due to the non-binding separation mechanism, the protein peak will get broad as they pass through the column. Sample injection volume need to be kept small to achieve high separation resolution. No buffer change is needed in SEC purification process. Only one buffer was used in the SEC separation process. SEC is often used for desalting and buffer exchanges. Also, SEC can be used in the last step of the three-stage purification strategy (polishing).

1.5.4 Immobilized metal ion affinity chromatography

Immobilized metal ion affinity chromatography (IMAC) separates proteins based specific affinity binding between target protein and metal ion (Ni^{2+}, $Cu2^{2+}$, Zn^{2+}, Co^{2+}) modified matrix [43]. Target protein will specifically bind with the matric surface through chelation binding, while other impurities will be washed away during the sample load step. In current therapeutic protein production, target protein can be genetically modified to include a poly-histidine tag at a terminal position away from active sites. Critically this allows an engineered marker that forms a strong chelation bonding with Ni^{2+}, to give a highly selective protein purification process among proteins of similar size and charge.

There are usually four steps in an IMAC process. First, the chromatography medium is equilibrated with ~20 mM imidazole buffer; in the second sample loading step, Poly-

histidine tagged protein bind to the metal ion groups of the medium and get concentrated. It should be noted that ~20 mM imidazole concentration is used in the loading sample solution to eliminate non-specific binding. Impurities won't bind to the medium and are eluted after sample injection. Third, 200-500 mM imidazole solution is used to elute the bound protein. This can be achieved through gradient elution or step elution. Finally, the column is re-equilibrated.

1.6 Enzyme immobilization

In addition to separations, membranes can be used as supports for catalyst giving simultaneous separations and reactions in a field known as 'membrane reactors'. Of particular importance are enzyme catalysts that have seen broad use in waste water treatment[44]. Biological enzymes can do far more complex chemistry than man-made systems due to their highly complicated structure. In spite of the great opportunity of biological enzyme in drug discovery, they are relatively fragile/unstable, expensive and hard to reuse. This prevents their wide use in industry processes. Immobilization of enzyme is one of the most important engineering strategies to address these limitations, but must not de-nature the activity of the enzyme when bound to the surface. Both carrier-free and carrier-based immobilization technology have been used for enzyme immobilization. Carrier-free immobilization, mostly cross-linking of an enzyme, can result in the loss of enzyme activity due to the intensive modification of residues by glutaraldehyde cross-linker [45,46]. Non-covalent adsorption on solid support is the easiest immobilization method. However, the supported-enzyme is prone to leach into bulk solution during the catalytic reaction. Carrier-based immobilization through covalent bond is much more stable. Generally, many lysine residues on the protein surface can be

tethered to the functionalized solid surface. These multipoint covalent bonds can increase the rigidity of the immobilized enzyme, which, on the other hand, increase the risk of changing the active sides of enzyme [47]. Enzyme immobilization using affinity tags is a better way to maintain enzyme stability on the solid support and retain the enzyme activity at the same time [48]. One example is the genetically modification of N-terminus of the enzyme with histidine tag, which has little influence on the activity of enzyme.

1.7 Cell electroporation

Another area of membrane application outside of separations and reactions, is the interaction with living cells. In particular the delivery of cDNA, siRNA, proteins or small drugs into living human cells plays a critical role in gene therapy, tissue engineering, recombinant protein expression and other bio-chemical treatments [49, 50]. However, current transfection methods have hindered their use for clinical and medical research applications due to their inefficiency in promoting target molecule uptake and toxicity. Chemical transfection using calcium phosphate precipitate, liposome and peptides have low efficiency and are often limited to certain cell types with specified cell size and shape [51, 52, 53]. Viral vector transfection is considered a more efficient transfection method [54, 55, 56]. However, viral vectors can cause serious immune response in the human body [57]. Moreover, the viral vector can't be effectively used in the patient again after a failed trial, because the body will recognize it. Due to the inefficiency, toxicity, immunogenicity and inflammatory response of current transfection methods, an effective and less invasive gene therapy and molecular delivery techniques are of great interest to biological and biomedical researchers [58].

As a safer and more efficient physical process, electroporation has been widely used

for introducing biomolecules into cells [59, 60, 61, 62]. Electroporation is the process of using an electric field to create temporary pores in the phospholipid-bilayer of the cell [63]. These temporary pores allow the passage of molecules through the cell membrane into the nucleus.

There are two kinds of electroporation technique-Irreversible electroporation and reversible electroporation. Irreversible electroporation is a tissue ablation technique using short and strong electric field to permanently damage the cell membrane. Reversible electroporation is the process of using an electric field to create temporary pores of the cell to allow the passage of molecules into the nucleus. Typically, electroporation threshold is between 150-400 V/cm.

Traditionally, cell electroporation is performed by placing two plate electrodes in a fixed-volume cuvette under high electric field [64]. However, this method can only perform limited amount of cells in each trial. Additionally, this approach requires high voltages (often >100V) to be applied across the electrodes to generate the desired electric field (150-424V/cm) [65] due to the long distance between the two electrodes in the cuvette. This high voltage applied often results in sudden changes in local pH and temperature around the cells leading to their necrotic death. Lastly, this approach requires large amount of expensive-to-produce transfection reagents that are diluted in the flow solution. Desired electroporation device should operate at a low voltage to get high viability, and operate in a flow-based continuous process to achieve high throughput. Particularly promising was the use of micro-patterned PDMS holes on Anodized Aluminum Oxide (AAO) membranes to concentrate electric fields within the hole between distant electrodes, thereby reducing effective electroporation voltage to 9V with

greater than 80% cell viability of adherent cells [66] However, there is very limited application for the genetic modification of adherent cells since the cells would have to be removed, transfected, and returned into the patient. More promising is to target mobile circulating cells, such as white blood cells. In this case a micro-fluidic channel would have to be thin enough to promote intimate contact of the cell with the electrode as it flowed across the membrane surface, which would serve to minimize the distance between target molecules and the cell membrane during electroporation.

1.8 Dissertation outline

The primary goal of this dissertation is to invent new active membranes based on nm-scale electrode geometries at membrane pore entrances and exits for biopharmaceutical applications. This is divided into three major topic areas: 1) protein separation with voltage pulse cycles, 2) enzyme immobilization and activation at pore/electrode surfaces and 3) cellular electroporation and electrophoretic injection at membrane pore electrode entrances. Chapter 2 and 3 will discuss protein purification using active membrane electrode system with voltage pulse cycles. Chapter 4 will present enzyme immobilization and activation at the membrane electrode surface. Chapter 5 will cover the cell electroporation using membrane electrode-microfluidic system. Chapter 6 provides the conclusion for this dissertation.

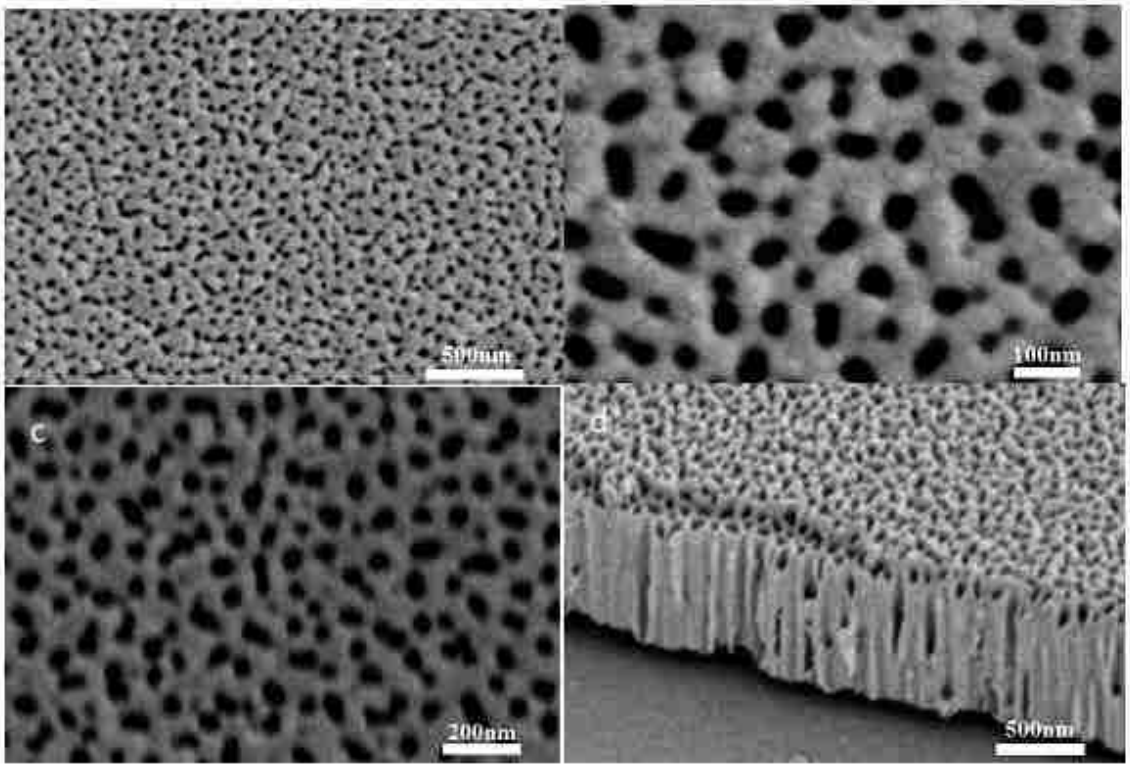

Figure 1.1 SEM image of the AAO membrane with 0.1M H_3PO_4 at different etching time. (A) 60min (B)75min (C)90min (D) Cross section of C. (Reprinted with permission from Ref. [6])

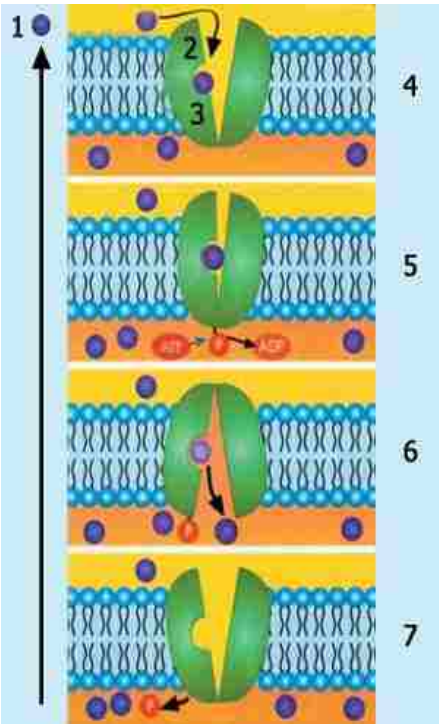

Active transport process

1. Soluble molecules
2. Transport protein
3. Binding region

4. Soluble molecules attach to the binding point of the opened transport protein in the cell membrane.
5. ATP transmits phosphate to the transport protein.
6. The phosphorized transport protein opens and changes shape so as to deposit the soluble molecules inside the cell.
7. The phosphate separates from the protein by assuming its original form. The stage is now set for another soluble molecule to be transported.

Figure 1.2 Active Transport process through cell that shows sequential actuations of gatekeeper chemistry. (Reprinted from ref. [13])

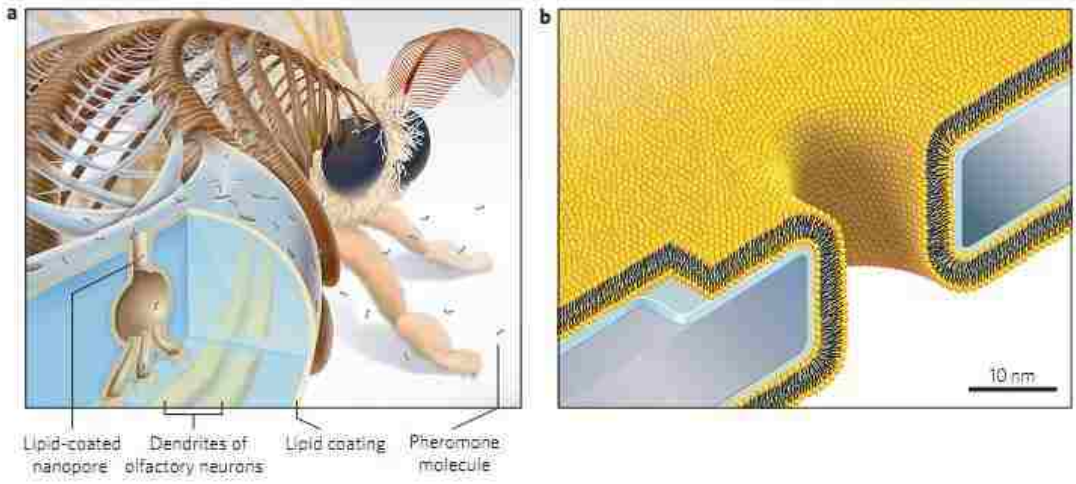

Figure 1.3 Bio-inspired synthetic nanopores with bilayer-coated fluid walls.(a) Cross-section of one sensillum in the antenna of the silk moth Bombyx mori. (b)Drawing to scale, showing a synthetic, lipid-coated nanopore in a silicon nitride substrate. (Reprinted with permission from Ref. [12])

Figure 1.4 Illustration of the zinc fingers immobilized single nano-channel. In the absence of Zn^{2+}, the zinc fingers in the nano-channel present unfolding structures; after Zn^{2+} binding, the zinc fingers gold to finger-like conformations, yielding an increase of the effective channel diameter. (Reproduced with permission from Ref. [19])

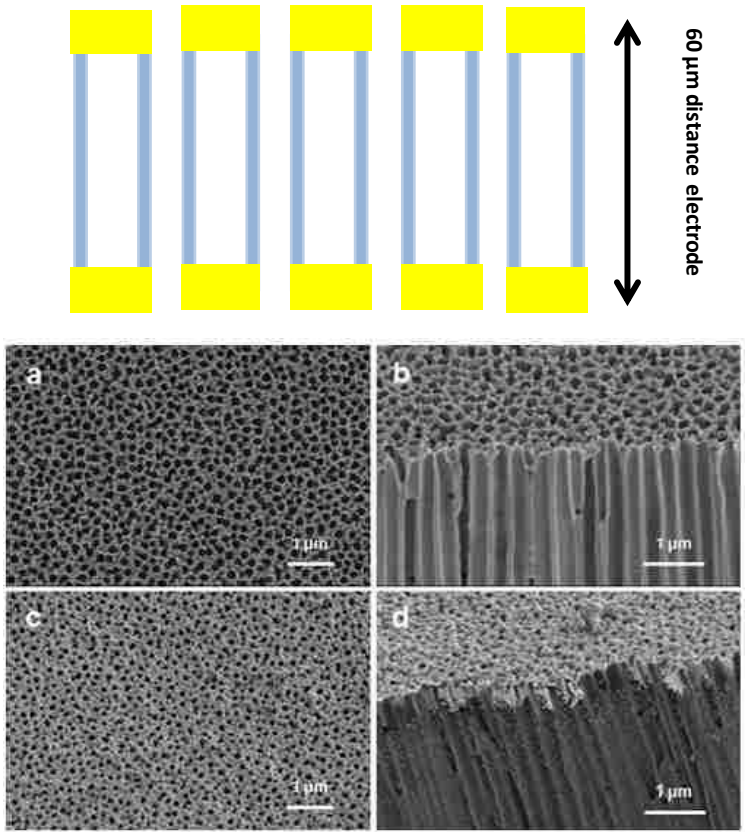

Figure 1.5 SEM images of bare AAO membrane and gold plating AAO membrane (a) Top view of bare membrane. (b) Cross section of bare membrane. (c) Top view of gold-coated membrane. (d) Cross section of gold-coated membrane. The achievable electric field can be calculated by E=V/L, where V is the applied voltage on the membrane surface and L =60 µm is the membrane thickness.

Chapter 2 : Dynamic Electrochemical Membranes for Continuous Affinity Protein Separation

This chapter is based on the manuscript: Zhiqiang Chen, Tao Chen, Xinghua Sun, Bruce. J. Hinds. 'Dynamic Electrochemical Membranes for Continuous Affinity Protein Separation', Advanced Functional Materials, in press

2.1 Introduction

Genetic modification of a host cell to produce complex biomolecules is the critical route to bio-pharmaceutical production [67, 68, 69]. However, the separation of the desired protein from the myriad in living systems is the most costly and complicated step. The high cost of downstream purification of genetic protein expression hinders the wide-spread use of therapeutic protein treatments with an example prophylactic replacement therapy being greater than $100,000 per patient per year. Even with current advances in automated separation technology, 80% of the total cost of urokinase production is in purification [70]. The ability to genetically add poly-histidine tags to recombinant proteins enables affinity purification by immobilized metal ion affinity chromatography (IMAC) [71], which is the dominate separation method. However, IMAC suffers from limitations of long intra-particle diffusion time, high pressure drops, difficulties in packing large columns, column regeneration, non-specific binding, high cost and long binding/purge cycles [72]. The ideal separation method would be to have a selective membrane that could actively pump selected proteins across a barrier in a continuous process. Traditional polymeric ultrafiltration membranes have been studied for protein separation/purification [73, 74], however pore size is difficult to control and manipulate,

leading to modest selectivity between similar proteins. Track-etching membranes and porous alumina membranes have precise pore size [75, 76] and Au plating has been successfully used to tune pore size surface chemistry, and electrochemical activity [32, 33]. In complex mixtures, many classes of proteins have similar size and surface charge, making selectivity an ongoing challenge. Indiscriminate flow induced fouling is still a major limitation in pressure driven membrane separation that needs to be addressed [77]. Applied electric field, instead of pressure across the thick nanoporous membranes [78, 79] have shown enhanced rates and rough charge density based separation. Ultrathin silicon membranes with ~10 nm thickness and 5 nm pore size have even been developed and show potential for protein separation [80] due to short path length and tight pore size distribution. However separations based principally on the basis of size and/or charges are not sufficient to isolate specific proteins from complex cell extracts. Affinity nanoporous membranes with immobilized ligands within the pores have the ability to capture highly specific proteins from cell extracts. However the operation is similar to IMAC, requiring binding/release cycles. Compared to IMAC, the membrane have more efficient flowing mass transport to binding sites but several orders of magnitude less binding area [81].

Biological membranes are capable of selectively transporting chemicals at dramatically enhanced rates with precise chemical selectivity and thus bio-inspired membranes have various applications in sensing, drug delivery and chemical separations [8, 82]. To mimic this natural biological system, the membrane platform should have receptor chemistry at the pore entrances acting as gatekeeper that can specifically capture and concentrate the affinity protein, and a driving force to pump protein across the

membrane barrier. Here we report an active membrane system based on nm-scale electrodes that allow voltage pulses for sequential affinity protein binding and release/pumping cycles. In particular the pore entrance is designed to have specific bound proteins, during both cycles, which block the pore from undesired protein transport across the membrane.

2.2 Experimental details

2.2.1 Reagents and Materials.

20nm Anodic Aluminum Oxide (AAO) membranes (60 μm thick) were obtained from Whatman (GE Healthcare). These AAO membranes are asymmetric with a bulk pore structure comprised of 200 nm diameter straight channels and a thin porous layer at the top with a diameter of 27 nm. The porosity was ~40-60%. Gold (I) thiosulfate (Alfa Aesar) was used to electro-less deposit gold electrodes at the entrance and exits of these membranes. $NiCl_2$, Nα, Nα-Bis(carboxymethyl)-L-lysine (NTA, Sigma Aldrich) and Ascorbic acid (EM Science) were used as received. Bovine serum albumin (BSA, pI=4.9, MW=67 000) was purchased from Sigma Aldrich and used as received. Texas red conjugated BSA was purchased from Life Technologies Aldrich and used as received. His-tagged green fluorescence protein (His-GFP, pI=5.7, MW=28 000) was obtained from Millipore and used as received. Purified water was prepared using a Millipore Milli-Q water purification system with 18.0 MΩ.cm resistivity. Regenerated cellulose membranes (molecular weight cutoff 3500) were purchased from Spectrum Laboratories, Inc. These regenerated membranes were rinsed with water for 1 h to remove glycerine before use.

2.2.2 Gold Electrodes/AAO membrane Preparation

Gold sputtering was first performed to create gold seed for the gold electro-less plating. Sputtering was performed with a Cressington Coating System (Ted-Pella) with calibrated quartz crystal monitor with background pressure of 0.02 mbar at 100W power supply. No intermediate wetting layer (i.e. Ti/TiO_2) on Al_2O_3 was needed for seeding the Au layer. 5 nm gold was sputtered on both the entrance and exit of AAO membranes at 1nm/min gold sputtering rate, which would deposit the diameter (20nm for the entrance and 200nm for the exit) distance down the pore. The gold Electro-less plating reactions will only form on the sputtered gold seed. Electro-less plating [38] was accomplished in 50 mM pH 7.0 phosphate buffer containing 1.6 mM sodium gold (I) thiosulfate and 2.68 mM ascorbic acid. The oxidization and reduction reactions are given by

$$C_6H_8O_6 \longrightarrow C_6H_6O_6 + 2e^- + 2H^+$$

$$Au(S_2O_3)_2^{3-} + e^- \rightleftharpoons Au + 2S_2O_3^{2-}$$

The pore size can be tuned by controlling the electro-less plating time. The AAO membrane pore entrance size was measured by the analysis of images from a Hitachi S-4300 Scanning Electron Microscope (SEM).

2.2.3 Gold Electrodes/AAO Membrane Functionalization

As-prepared gold/AAO membranes were covalently grafted with N_α, N_α-Bis(carboxymethyl)-L-lysine (NTA, Sigma Aldrich) by electrochemical oxidation [83]. The electrochemical grafting was performed in 0.1 M $LiClO_4$ ethanol solution with 10 mM NTA (Figure 2.11). Five cycles' cyclic voltammograms scan from 0 V to 1.2 V with a 0.83 V oxidation peak of was carried out at 10 mV/s. After electrochemical oxidation

grafting, a cyclic voltammograms of 0.1 M in $K_3Fe(CN)_6$ in 0.1M PHOSPHATE solution (PH=7) was carried out to show increased surface resistance from grafting (Figure 2.12). The membrane was then thoroughly rinsed using de-ionized water and ethanol to dissolve any byproducts after the electrochemical oxidation grafting. The membrane was finally incubated in 0.1 M $NiCI_2$ (Sigma Aldrich) for 30 min to form conjugate Ni-NTA surface. The chelate binding between Ni-NTA and His-tagged GFP is diagrammed in Figure 2.2.

2.2.4 Bulk mobility of GFP and mobility of imidazole across the AAO membrane

The bulk mobility of GFP (7×10^{-5} cm^2s^{-1} V^{-1}) at PH 7 was measured by using a particle-size and zeta-potential analyzer (Beckman Coulter Delsa(TM) Nano C Particle Analyzer) at 25℃. The experimental mobility of imidazole across the AAO membrane was studied using the setup in Figure 2.13 without the waveform generator. First a four-point standard curve of imidazole was drawn based on the 280nm UV-vis adsorption of imidazole at different concentrations. The imidazole mobility (μ) at PH 7 then can be determined by $\mu = \frac{J}{E\times C}$, where J is the imidazole flux across the AAO membrane; E is the electric field across the AAO membrane and C is the feed imidazole concentration. The calculated imidazole mobility through AAO membrane is 14.4×10^{-5} $cm^2s^{-1}V^{-1}$.

2.2.5 Protein Separation Experiments

Two model proteins used for separation are His-GFP and BSA. His-tagged GFP has Eleven strands on the outside of cylinders form the walls of the structure. The cylinders have a diameter of 30 Å and a length of 40 Å. BSA is also a cylinder with a diameter of 55 Å and a length of 90 Å. The setup for protein pumping process was shown in Figure 2.13. In direct electrophoretic pumping, only the potentiostat (EA164 QuadStat, eDAQ

Pty Ltd), which is controlled by an e-corder 410 (eDAQ Pty Ltd) with Chart^{TM} software, was used and placed on the outer cell. Two Pt wires (one connected to the working electrode and the other one connected to the counter and reference electrode) were connected to the potentiostat and inserted into the outer electrolyte phosphate buffer (50 mM, PH=7) solutions. Two regenerated cellulose membranes (3500) were used in the experiment. BSA (67 000) and GFP (28 000) were restricted in the feed and permeate solution by the regenerated cellulose membranes (3500), which kept the proteins from oxidation or reduction by high voltages (6 V) generated at the Pt electrodes. At PH 7, both GFP and BSA were negative charged. The anode was in the Phosphate buffer adjacent to the permeate solution so that the negative charged proteins will be electrophoretically pumped to the permeate solution and the positively charged imidazole will be electrophoretically pumped to the feed solution from the permeate solution. When a 6 V was applied by the potentiostat, the voltage drop directly measured across the gold electrodes/AAO membrane was 0.3 V. Water underwent electrolysis and generated H^+ in the anode and OH^- in the cathode at 6 V in the outer compartments and phosphate Buffer was changed frequently to maintain the PH during the water electrolysis process. The volume of feed solution was ~1mL and the permeate solution was ~0.5 mL. The feed solution contained 7 μg/ml Texas red conjugated BSA and His-tagged GFP and the permeate solution contained 0.1-10 mM imidazole. In the pulse electrophoretic pumping process, a waveform generator (keithley 3390 50 MHz arbitrary waveform generator) was also used to generate 0.05 V on the gold/electrodes/AAO membrane during the binding cycle. The potentiostat was used to generate 0.3 V on the gold/electrodes/AAO membrane during the release/pumping cycle. The feed solution contained (1) 7 μg/ml

Texas red conjugated BSA and His-tagged GFP or (2) 1000 μg/ml BSA and 10 μg/ml His-tagged GFP; and the permeate solution contained 10 mM imidazole.

2.2.6 Protein assay methods

The fluorescence intensity of His-GFP was measured using a fluorescence spectrophotometer (PerkinElmer LS 55 Fluorescence spectrometer), with an excitation filter of 395 nm and an emission filter of 509 nm. The fluorescence intensity of Texas red conjugated BSA was measured with an excitation filter of 596 nm and an emission filter of 615 nm. The fluorescence intensities of the experimental samples were compared to the five–point standard curves of His-GFP and Texas red conjugated BSA. In the 1000ug/ml BSA and 10ug/ml His-tagged GFP purification experiment, the total protein in the feed and permeate solution was expressed in mg/mL and compared with total protein concentrations expressed as BSA at λ = 280 nm in a spectrophotometer. The BSA standard curve for the permeate solution was drawn based UV-vis adsorption of BSA at the 280 nm in 10 mM imidazole solution since the UV-vis adsorption of 10 mM imidazole in the permeate solution will interfere with BSA. The total protein concentrations in the permeate solution ranged from 50 to 1000 μg/mL, and the comparative relationship between total proteins and BSA was made through the five-point calibrated BSA standard curve.

2.2.7 COMSOL Simulation

COMSOL 4.3 package (COMSOL, Inc, Burlington, MA) was used to model the electric field distribution across the asymmetric AAO membrane. A stationary 2D "Electric Current" mode under AC/DC model was created for the simulation. The model geometry is described as isosceles trapezoids with 0.2 μm bottom base and 0.02 μm top

base separated by 0.5 μm Al_2O_3 wall with a thickness of 60 μm. Phosphate-buffered saline is filled within the geometry pore and 2um above/below the membrane surface. The electric conductivity of the phosphate-buffered saline is 0.127 S/m. The electric conductivity of Al_2O_3 is 10^{-5} S/m. The boundary conditions used in our calculations were a constant potential drop (0.3 V) between the top phosphate-buffered saline solution (2um above the top membrane surface) and bottom phosphate-buffer saline solution (2um below the bottom membrane surface). The geometry was built with fine element mesh and computed.

2.2.8 Numerical Modeling of Protein Pumping Membrane System

Microsoft Excel with Visual Basic Macros was used to numerically calculate concentrations in the model system. A matrix of 240 x-values (0-120 μm, 0.5 μm steps) was initialized with boundary conditions and starting profiles. A new matrix was made for the new time (previous time + time step). Flux to/from neighbor cells into new matrix were calculated using Equation (1). The concentration change in the cell can be calculated from Equation (2) using the values in the matrix of the prior time step. After calculating each new concentration at x location, the prior time step matrix is overwritten with the newly calculated matrix and the cycle repeated until desired total time is reached using 'For/Next' loops in Visual Basic. Time steps were chosen to be such that $(D\Delta t)^{0.5}$ + $cE\mu\Delta t$ (characteristic diffusion length + electrophoretic distance) was much less than Δx (typically $0.1*\Delta x$) to ensure numerical accuracy and stability.

Detail physical parameters in the model:

His-GFP bulk mobility: 7.5E-05 $cmV^{-1}s^{-1}$

His-GFP bulk diffusion coefficient: 8.7E-07 cm^2/s [84]

His-GFP diffusion mobility within the pore: 2.5E-06 $cmV^{-1}s^{-1}$

His-GFP diffusion coefficient within the pore: 6.25-08 cm^2/s (Einstein relation)

Imidazole mobility: 1.44E-04 $cmV^{-1}s^{-1}$

Imidazole diffusion coefficient: 3.6E-06 cm^2/s (Einstein relation)

Time step(Δt): 5E-5 s

(Dt)^0.5+ cEut = 4.3E-6cm (must be less than Δx)

Distance step(Δx): 5E-5 cm

Electric field within the membrane during pumping cycle: 50 V/cm

Electric field outside the membrane during the pumping cycle 0.5V/cm

Electric field within the membrane during repel cycle: 0.83 V/cm

Electric field outside the membrane during the repel cycle 0 V/cm

Bulk pore porosity (30.5 μm to 90 μm): 60%

Porosity at the top thin porous electrode layer (30.0 to 30.5 μm): 10%

Porosity at the top thin porous electrode layer after protein blocking (30.0 to 30.5 μm): 3%

Initial conditions**:**

0-30 μm: 10 ug/ml His-GFP

30-120 μm: 0 ug/ml His-GFP

0-90 μm: 0 mM imidazole

90-120 μm: 10 mM imidazole

Boundary conditions:

Constant 10 μg/ml His-GFP at distance 0 μg for bulk feed solution.

Constant 0 mM imidazole at distance 0 μg for bulk feed solution.

Constant 0 μg /ml His-GFP at distance 30-30.5 μm (above membrane surface) for binding cycle

Cumulative amount of protein flux is saved as a variable stepwise

The absorbed protein on the membrane surface is released in 200 time steps (0.01s) at t=12 s of pumping/release cycle

Constant 10 mM imidazole at distance 120 μm of bulk permeate

2.2.9 Numerical model validation

To validate whether our numerical model is correct, we did a comparison of one dimension diffusion results solved by our numerical model and compared to the known analytical solution of Fick's second law. A simple case of diffusion with time t in one dimension from a boundary located at position x=0 with a constant concentration n(0)=10 μg/mL is

$$n(x,t) = n(0)\mathrm{erfc}(\frac{x}{2\sqrt{Dt}})$$

where erfc is the complementary error function, D= 8.70×10^{-7} cm^2/s is the diffusion coefficient. One dimension diffusion plot solved by numerical model and complementary error function was shown in Figure 2.14. As shown in Figure 2.14, the results solved by numerical model and complementary error function overlap showing the accuracy of the numerical method with time and distance step. The deviation of total cumulative flux (Q, area under curve) calculated numerically to the analytical solution was 6E-3%.

2.3 Results and Discussion

The primary active area of this protein separation system is the nm-diameter electrode coated pore at the supported membrane pore entrance matched to the dimensions of proteins (~4nm). This allows bound his-tagged proteins to block the pore from non-selective protein transport. Shown in Figure 2.1 is a scanning electron microscopy image of porous anodic aluminum oxide (AAO) membrane. Cross-sectional SEM images shows that the bare AAO membranes are asymmetric with a bulk pore structure comprised of 200 nm diameter straight channels and a thin porous layer at the top with a diameter of 27 nm [85]. The top and bottom membrane surfaces are coated with 5nm of Au using sputtering deposition. This Au acts as a seed layer for the following Au electro-less plating at the pore entrance region to reduce pore diameter to 10nm by controlling plating time [Figure 2.10]. The distance of the gold electrode down into the pore is also important since if the affinity chemistry is along the entire length of the pore, protein transport would be blocked by bound proteins. The sputtering process, though not line-of-sight, would be expected to deposit Au roughly 20 nm (pore diameter) distance down the pore allowing 3-5 layer proteins to be bound along the channel. Nα, Nα-Bis(carboxymethyl)-L-lysine (NTA) was covalently grafted onto the gold electrode by electrochemical oxidation of the primary amine as depicted in Figure 2.2 [86], which is more resilient than thiol-Au analog [87]. Cyclic-voltamograms of grafting process showed increased surface resistance [Figure 2.11, 2.12] confirming successful grafting. To demonstrate selective pore blockage by his-tagged green fluorescence protein (His-GFP) and subsequently releasing of His-GFP by imidazole, the electrophoretic fluxes of BSA before His-GFP binding, with bound His-GFP and after imdizaole releasing were

studied and shown in Figure 2.3. BSA was used to simulate complex protein mixtures, since having the same polarity as His-GFP represents the biggest challenge in electrophoretic-based separations. A seven-fold decrease of BSA flux was seen in the blocked case and recovered to 95% of the original flux after imidazole release. Table 2.1 shows the flux of His-GFP and BSA mixture (1:1) as a function of imidazole release agent. At high imidazole concentrations (10mM) no binding/blocking was seen and both proteins are pumped through and no preferential separation was seen. At 1mM imidazole partial blockage was seen with reduction in flux and modest selectivity. With the lowest imidazole (0.1 mM) concentration both GFP and BSA fluxes were markedly reduced (factor of 3.4 and 30 respectively) and a selectivity of 7.7 was seen. Two important inferences can be made from these series: 1) more than one layer of his-GFP is blocking the pore entrance since, with an open pore there would be a 50% chance of His-GFP binding or BSA passage. This would give a maximum separation factor of 1.5 while 7.7 was observed; 2) selective binding of His-GFP within pore, though enriching His-GFP, dramatically slows the flux, giving an inherent trade-off in flux vs selectivity that is only exasperated with dilute target concentrations found in common separations.

The ideal separation system would be a two-cycle process with binding step followed by transport step, mimicking the function of cell wall transporters. This can be achieved with electrophoretic pulses described in Figure 2.4 with 2 two-electrode pairs system (Figure 2.13). During the first binding cycle, a small positive bias was applied on top Ni-NTA/gold surface to attract anionic His-GFP and repel imidazole from the binding surface and pumps it to the permeate side. The second electrode pair, outside of the regenerated cellulose membrane, applies a large voltage to pump cationic imidazole from

permeate side to the binding sites as well as pump the released anionic His-GFP across the membrane to the permeate side. Figure 2.5 shows the fluorescence spectra of feed and permeate solutions, showing selective transport of His-GFP and a near background level signal of BSA. The results of the pumping study are summarized in Table 2.2. The first data column shows the control experiment with no binding chemistry and using only electrophoretic pumping (step 2). In this case both proteins have high flux, comparable mobility, and lack of selectivity due to open channels. In the second case, there is binding chemistry at the entrance and a 10mM supplementary of cationic imidazole in the permeate side that is pumped towards the binding site. In this case the pumping rate decreased due to binding chemistry at the pore entrance thus reduced pore size but no selectivity is seen since both proteins are electrophoretically pumped through the membranes. For the pulse pumping experiments in Table 2.2 we used a 0.05 V, 1s pulse for binding and a 0.3 V, 14 s pulse for pumping. In this case a significant increase in His-GFP flux was seen and a selectivity of 9.2 was observed. It should be pointed out that this experiment had 100 fold higher BSA concentrations than His-GFP to more accurately simulate separations. In such a case there is a 100-fold higher probability of BSA entering an open pore entrance after His-GFP is released. The high separation factor indicates that the pore remains largely blocked, stopping BSA flux during the pumping cycle. In the fourth data column, a 1:1 ratio of BSA/His-GFP is used to reduce the probability of BSA entering opened pore and selectivity is thus raised to 16 showing the validity of the active pumping separation system. The pumping cycle time of 14s was chosen based on a conservative estimate of the required amount of imidazole would be the molar equivalent of 150mM routinely used in IMAC to elute His-GFP times the AAO

membrane volume (1.9×10^{-3} cm^3). With a 0.3 V measured potential drop across membrane electrodes (60 μm) and the experimental observed imidazole mobility of 14.4×10^{-5} $cm^2s^{-1}V^{-1}$ (see experimental section) a imidazole flux of 7.2×10^{-8} $molcm^{-2}s^{-1}$is calculate from the 10mM permeate solution, thus requiring 12.5 s to give 150mM equivalent in the pore volume. To improve efficiency of pumping cycle a valid model needs to be developed.

The active membrane system is best modeled with a three-step process of 1) diffusion of target 2) pumping of imidazole to release target and 3) electrophoretic pumping of target to the permeate. The three processes can be simulated numerically in 1 dimension by a combination of Fick's 1st law of diffusion and electrophoretic pumping shown in Equation (1).

$$J = D\frac{\Delta c}{\Delta x} + uEc \qquad [1]$$

Where J is flux per unit area, c is concentration, D is diffusion coefficient, and u is mobility, E is the electric field and Δx is the step width of simulation cell size (0.5um).

The concentration change in the calculation cell is given by Equation (2)

$$\Delta c = J_{in} \times \Delta t \times \varepsilon_{rel}/\Delta x - J_{out} \times \Delta t \times \varepsilon_{rel}/\Delta x \qquad [2]$$

Where Δt is numerical simulation time step ($5x10^{-5}$s). J_{in} is flux (/unit area) in from neighbor cells and J_{out} flux out to neighbors calculated from Equation (1). Here ε_{rel} is the relative porosity of calculation cell with respect to neighbor cell. AAO membranes are asymmetric with 3% porosity at the protein bound site and 60% porosity in the membrane open pore structure. Pore size is shrinking as we approach the 20nm active pores and would thus expect increasing electric field due to increased resistance of smaller conducting cross-sectional area (see Figure 2.7, 2.8, 2.9). However, due to the

electrophoretic pumping of imidazole into a smaller volume, the ion concentration increases the conductivity of the solution thereby reducing electric field. Therefore we used constant electric field across the membrane in this simplified model. At the boundaries between feed solution, protein binding site, and open membrane channels, the difference of net protein flux, due to changes in porosities, leads to the accumulation of imidazole at the binding site during electrophoretic pumping. Details of the Visual Basic simulation parameters can be found in the experimental section. Shown in Figure 2.6A-C are simulation of feed solution (0-30 μm), binding site (30.0-30.5 μm), bulk membrane (30.5-90 μm), and the permeate solutions (90-120um). Figure 2.6A shows the 1 second binding cycle depleting the target protein from feed solution following Ficks law. This results in 0.0033 μg of protein absorbed onto the 0.32 cm^2 membrane area per 1s cycle. Figure 2.6A also shows the repulsion of imidazole at the binding site allowing target protein binding. The initial concentration of imidazole (t=0) was the steady state profile after 1 cycle. Figure 2.6B shows the numerical simulation of the release/pumping cycle. The imidazole is quickly pumped to a steady-state profile of high concentrations at the binding site. According to Equation (2), the concentration increase at the binding side is primarily due to reduction in porosity from bulk pore side (60%) to the binding site (3%). The drop in imidazole concentration into the feed (at 0.003 cm) is primarily a result of the abrupt change in porosity. This simplified model used 0mM imidazole at 0 um as a boundary condition to represent a bulk solution sink, but the concentration at this point would increase with pumping time to near the imidazole source concentration. However, most important is the imidazole concentration near the pore entrance (sub-micron scale). In the binding cycle, the imidazole is electrostatically pushed away from pore entrance

(figure 2.6(A)) and does not require a strong concentration gradient to the bulk value 0 mM to achieve this.

For the protein pumping, the pore is blocked by bound proteins at pore entrance and only pumping of bulky target towards the permeate (to the right) can occur. Depending on the release rate after imidazole accumulation, the concentration of protein in pores can exceed feed solution. In this case, the protein was released at 12 s and electropohoretically pumped into the channel. During the next pumping cycle, that peak would be pumped to the permeate for the full 14s of the cycle. Figure 6C shows the predicted concentration profiles after 10 full cycles at the end of release/pumping cycle. Most important is that the first protein peak is pumped away from the binding site with cycle 2 and a steady state profile develops. With its higher mobility, the imidazole concentration profile achieves steady state by the end of the first cycle.

For the third step of pumping protein across the membrane, the observed His-GFP mobility across AAO membrane was 1.92×10^{-6} $cm^2 s^{-1} V^{-1}$, roughly 75 fold slower than imidazole (14.4×10^{-5} $cm^2 s^{-1} V^{-1}$). Under 50V/cm field, the protein transit time across 60um thick membrane is 62.5 s. However, it is important to point out that the target protein does not have to exit the membrane during each cycle but be removed far enough from the binding site so as to not be pumped back during the binding cycle as seen in Figure 2.6C. The pumping distance of the target protein within the pore channel is directly proportional to the electric field times pumping duration. In our case a factor of 6 for electric field and 14 for pumping time would decrease the backwards pumping length during binding cycle by a factor of 84 compared to the forward pumping cycle. Our 1 s/14 s binding/pump cycle times was chosen from the estimates of the first two

steps. Decreasing the overall cycle time can increase pumping rate proportionally, however require the knowledge of release rate kinetics, which is the object of future study. At present this technique is not suitable for cationic proteins with extreme pI. Large increases in pH (>pI), to render the protein anionic, would likely agglomerate protein mixtures. An alternative binding system with anionic release agent would have to be used for cationic proteins to ensure opposite electrophoretic pumping direction. Also with complex Cell lysate mixtures additional pre-filtering would likely be required to prevent non-specific binding or agglomerate fouling.

Overall pumping efficiency can be calculated from the observed His-GFP (4.5 μg) collected in permeate divided by the calculated His-GFP captured (0.0033 μg) times number of 1s binding cycles (2640 cycles) giving 51.7% efficiency. This is also consistent with the premise that bound protein at the entrance is required to block the pore during pumping of released target. This non-optimized system can be directly compared to commercial IMAC columns where this system requires 0.75cm^2 of membrane area to have the same through put as a 1 cm^3 IMAC column used for laboratory scale separations. Ni-NTA Superflow Cartridge is a QIAGEN product for efficient affinity protein purification. Ni-NTA Superflow is comprised of Ni-NTA coupled to Superflow resin. QIAGEN Ni-NTA Superflow Cartridges are pre-filled with 1 ml Ni-NTA Superflow and are ready to use for purification of 6xHis-tagged proteins using a liquid chromatography system (such as the ÄKTAdesign™ or FPLC™ System). The bead diameter is 60-169 μm and the recommended flow rate is 1 mL/min with maximum pressure around 5 bar. To purify 1ml 1000 μg/mL BSA and 10ug GFP mixtures using an Automated Chromatography System equipped with Ni-NTA Superflow Cartridge we

would use three steps, equilibration (10 min), loading/washing (20 min) and elution (10 min) during the chromatography process. With a loading volume 50 μL, 20 runs are needed to separate 1ml volume of feed solution taking 10.3h. In our pulsed experiment, GFP flux across the membrane is 1.29 $\mu g.cm^{-2}\ h^{-1}$. In order to separate 10 μg GFP from the 1ml mixtures in 10.3 h, the needed membrane area is 10 μg /(1.29 $\mu g\ .cm^{-2}\ h^{-1}$ ×10.3 h)=0.75 cm^2. With optimization of binding/release pulse and electrode geometry a promising active separation system from continuously producing bio-systems can be realized.

2.4. Conclusion

In conclusion, commercial available AAO membranes were successfully functionalized to mimic biological membranes for efficient protein separation. His-tagged proteins bound to the pore entrance block other proteins in a sequential/hopping manner, allowing selective transport. Electrophoretic pumping eliminates fouling associated with pressure flow, while pores closed by gatekeeper prevent fouling by other charged proteins. Pulsed electrophoresis binding/release/pumping cycle allows for a continuous protein separation process with low cost and high productivity. This would revolutionize protein separations where expressed proteins can be directly removed from fermentation baths with this membrane separation system.

Table 2.1Electrophoretic flux and Mobility of Texas red conjugated BSA and His-GFP through Ni-NTA-Gold/AAO membrane with different imidazole concentration in permeate side

Imidazole concentration (mM)	10	1	0.1
BSA flux ($\mu g\ h^{-1}\ cm^{-2}$)	0.30	0.12	0.01
His-GFP flux ($\mu g\ h^{-1}\ cm^{-2}$)	0.28	0.19	0.082
BSA effective mobility ($10^{-6} cm^2\ s^{-1}\ V^{-1}$), u_b	1.97	0.79	0.07
His-GFP effective mobility ($10^{-6} cm^2\ s^{-1}\ V^{-1}$), u_g	1.88	1.27	0.54
Selectivity, $S=u_g/u_b$	0.95	1.6	7.7

Table 2.2 Electrophoretic mobility and flux of BSA and His-tagged GFP proteins as a function of electrophoretic pumping cycle

Pumping type	Gold/AAO membrane, direct pumping [a)]	Ni-NTA-Gold/ AAO membrane, direct pumping [a)]	Ni-NTA-Gold/AAO membrane, pulse pumping [a)]	Ni-NTA-Gold/AAO membrane, pulse pumping [b)]
BSA flux ($\mu g\ h^{-1}\ cm^{-2}$)	112.56	48.32	14.07	0.02
His-GFP flux ($\mu g\ h^{-1}\ cm^{-2}$)	0.73	0.34	1.29	0.32
BSA effective mobility ($10^{-6} cm^2\ s^{-1}\ V^{-1}$), u_b	6.24	2.64	0.78	0.16
His-GFP effective mobility ($10^{-6} cm^2\ s^{-1}\ V^{-1}$), u_g	4.08	1.92	7.2	2.54
Selectivity, $S=u_g/u_b$	0.65	0.73	9.23	16

[a)] Feed solution contains 1000 μg/mL BSA and 10 μg/mL His-tagged GFP; [b)] Feed solution contains 7 μg/mL Texas red conjugated BSA and 7 μg/mL His-tagged GFP. The imidazole concentration in the permeate side is 10 mM.

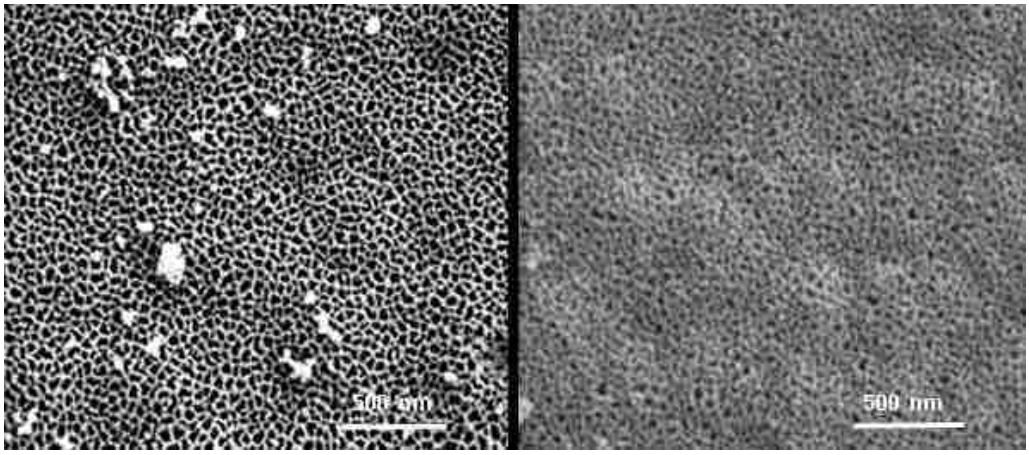

Figure 2.1SEM images of AAO membrane (left) and with electro-less plated Au on top surface (right) to control the pore entrance sizes

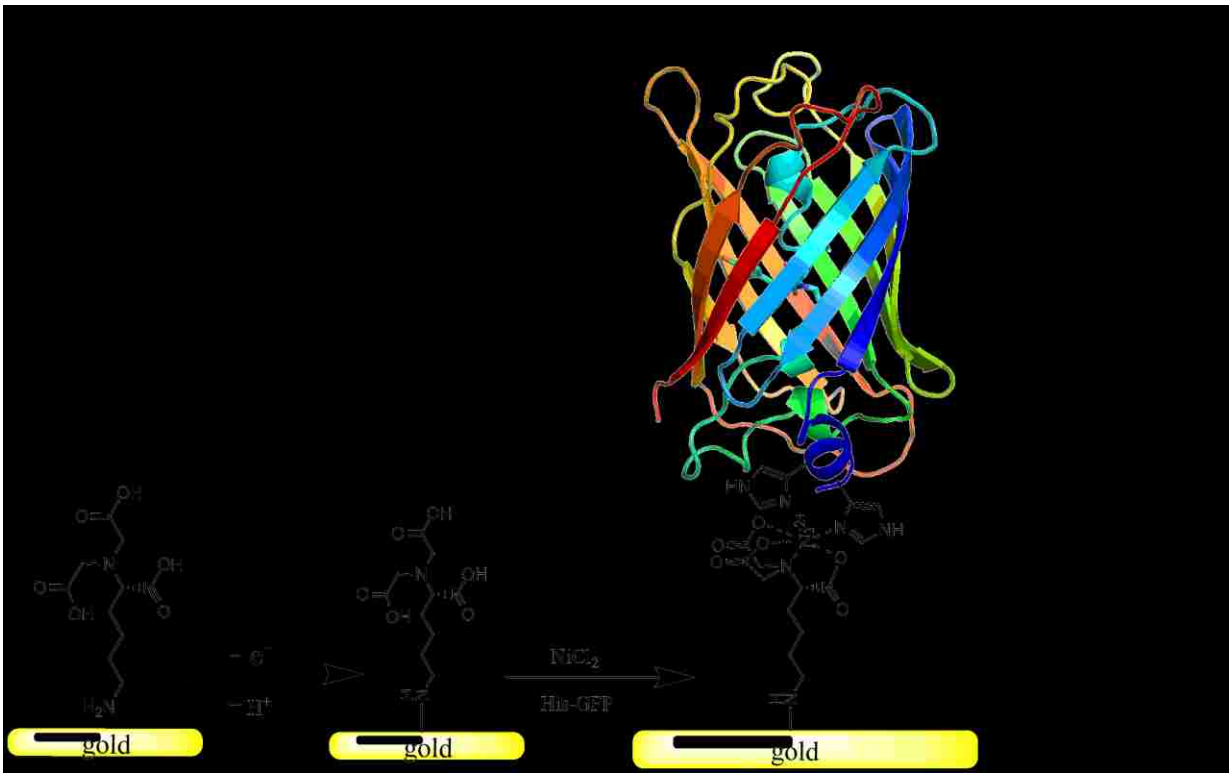

Figure 2.2 Schematic of N_α, N_α-Bis(carboxymethyl)-L-lysine electrochemical oxidation to functionalize gold layer and chelation bonding between NTA-Ni^{2+} and His-GFP

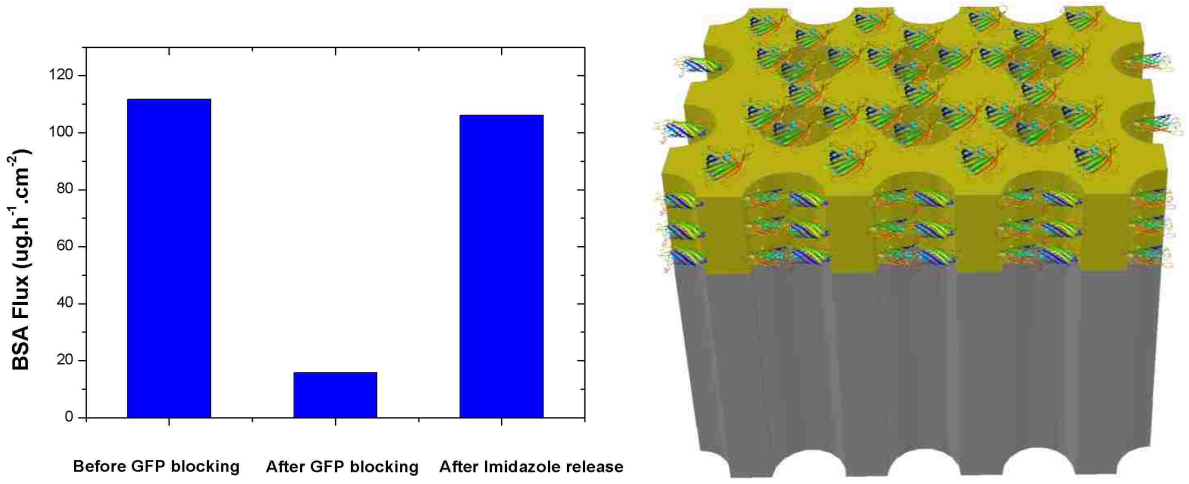

Figure 2.3 Electrophoretic pumping flux of BSA through functionalized AAO membrane before, after his-tagged GFP blocking and after imidazole release of His-GFP (1000 µg/ml BSA feed concentration) (a); Schematic of AAO membrane blocked by his-tagged GFP pore and protein size drawn to appropriate scale (b)

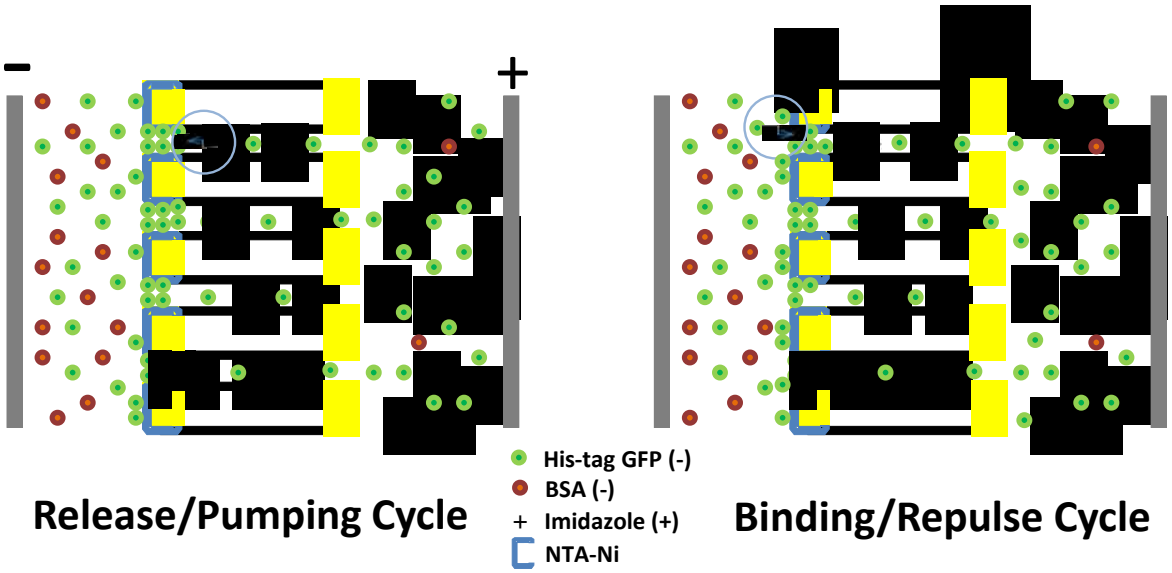

Figure 2.4 Schematic of pulsed electrophoresis process to pump His-tagged proteins across functionalized anodic aluminum membrane

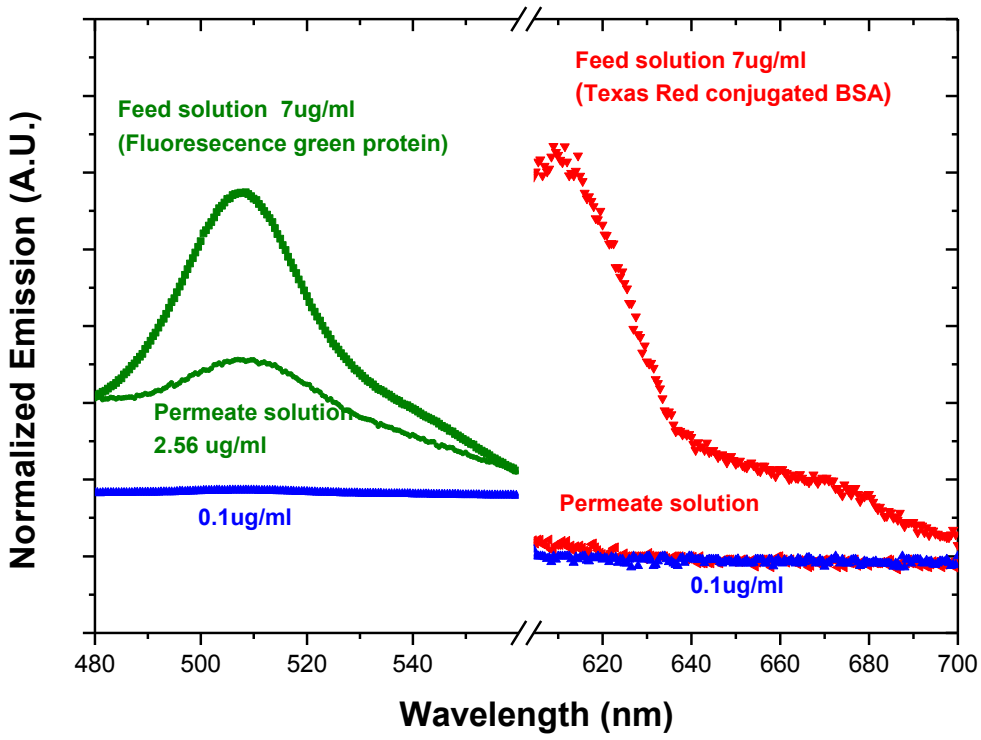

Figure 2.5 Fluorescence spectra showing the emission intensity of the baseline solutions, feed solutions and permeate solutions after pulse electrophoresis

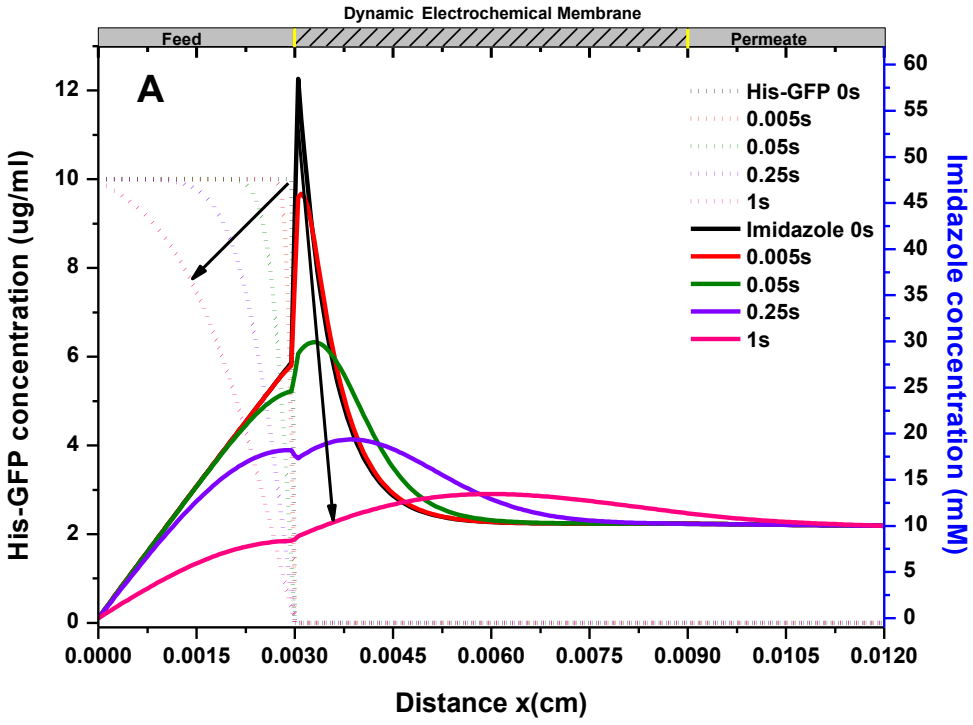
Dynamic Electrochemical Membrane
Feed
Permeate
A
His-GFP 0s
0.005s
0.05s
0.25s
1s
Imidazole 0s
0.005s
0.05s
0.25s
1s
His-GFP concentration (ug/ml)
Imidazole concentration (mM)
Distance x(cm)
0
2
4
6
8
10
12
0
5
10
15
20
25
30
35
40
45
50
55
60
0.0000
0.0015
0.0030
0.0045
0.0060
0.0075
0.0090
0.0105
0.0120

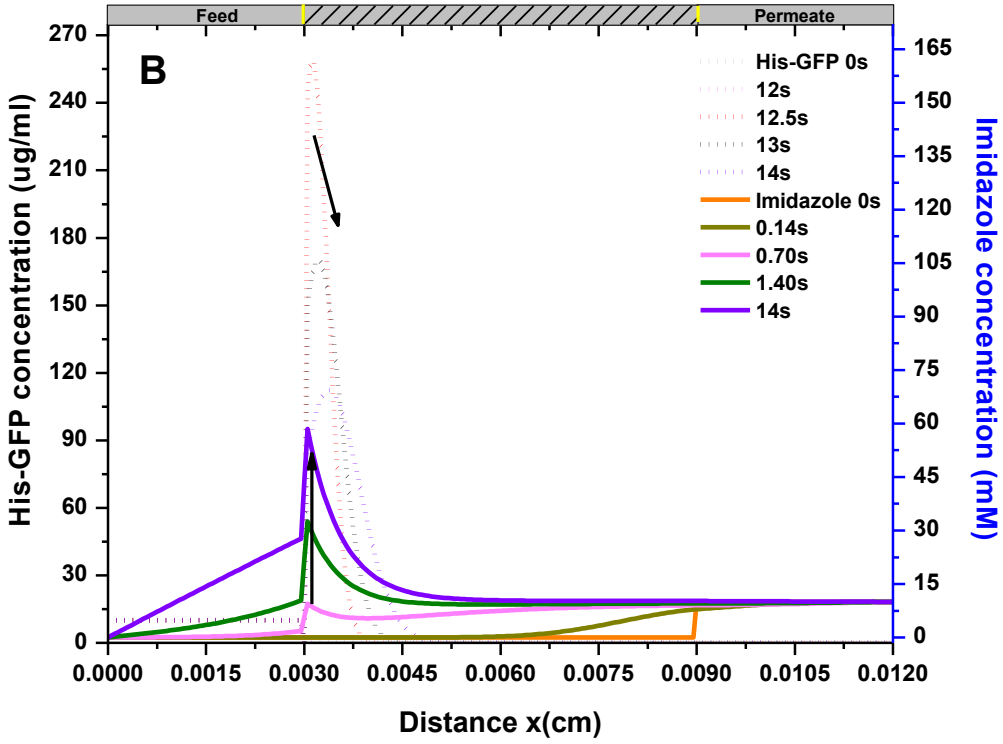
Feed
Permeate
B
His-GFP 0s
12s
12.5s
13s
14s
Imidazole 0s
0.14s
0.70s
1.40s
14s
His-GFP concentration (ug/ml)
Imidazole concentration (mM)
Distance x(cm)
0.0000
0.0015
0.0030
0.0045
0.0060
0.0075
0.0090
0.0105
0.0120

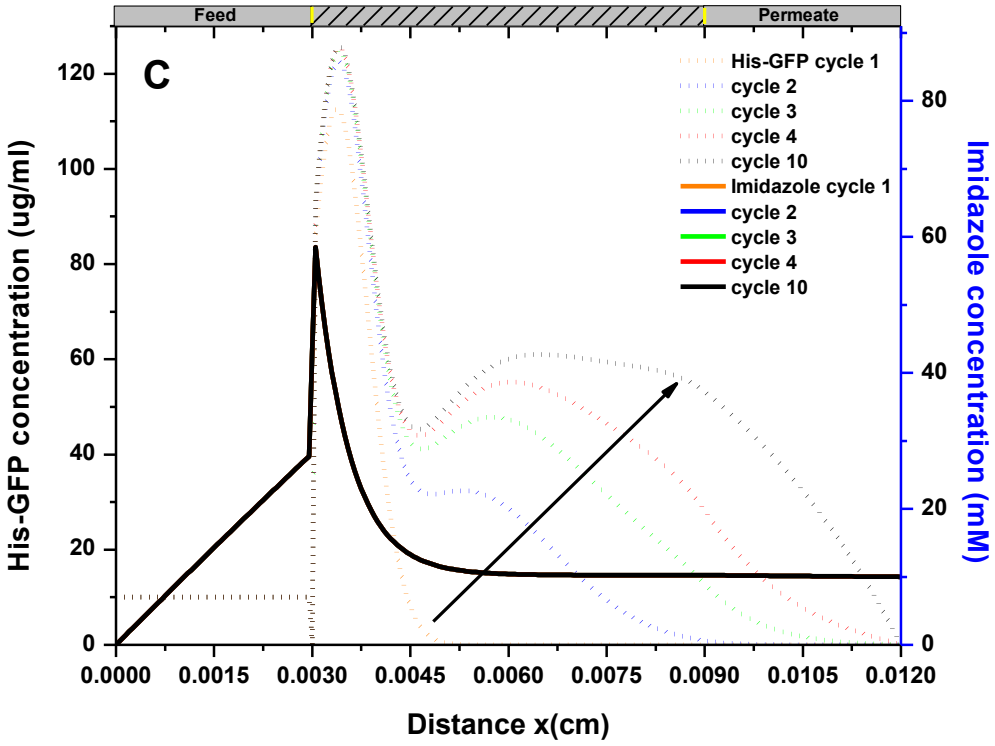

Figure 2.6 Numerical simulation results of the pulse pumping cycles: (A) His-GFP binding and imidazole repulsion concetration during the 1s diffusion/repel cycle +0.05V at top electrode (x=30 μm); (B) His-GFP pumping and imidazole accumulation concentration profile during the 14s releasing/pumping cycle (50 V/cm across simulation); (C) His-GFP and imidazole concentration profile at the end of pumping/releasing cycle as a function of total cycle number. Imidazole profiles all overlap under cycle 10.

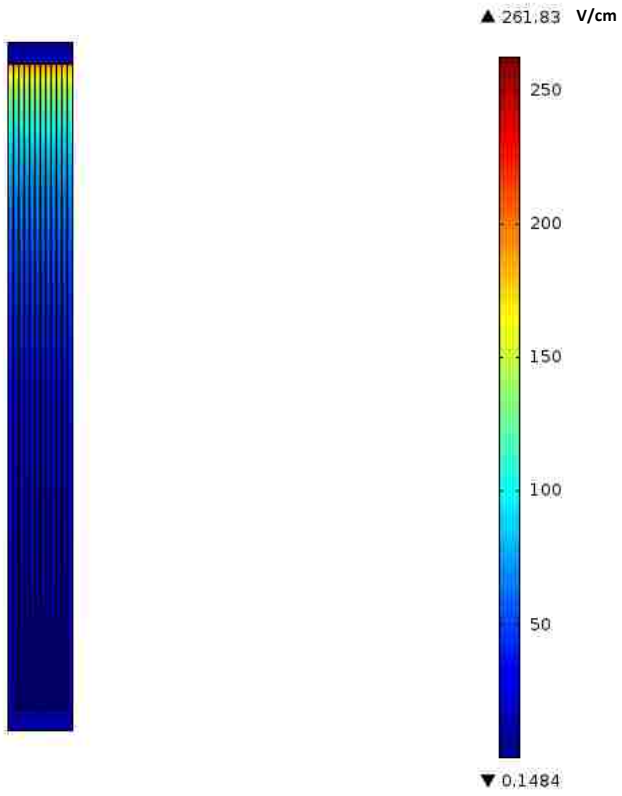

Figure 2.7 COMSOL simulation of electric field (EF) distribution across AAO membranes with 20 nm pores on top and 200 nm pores on the bottom. 2 μm gaps for top and bottom electrodes to simulate 300 mV voltage drop across the membrane with the external transmembrane electrodes present

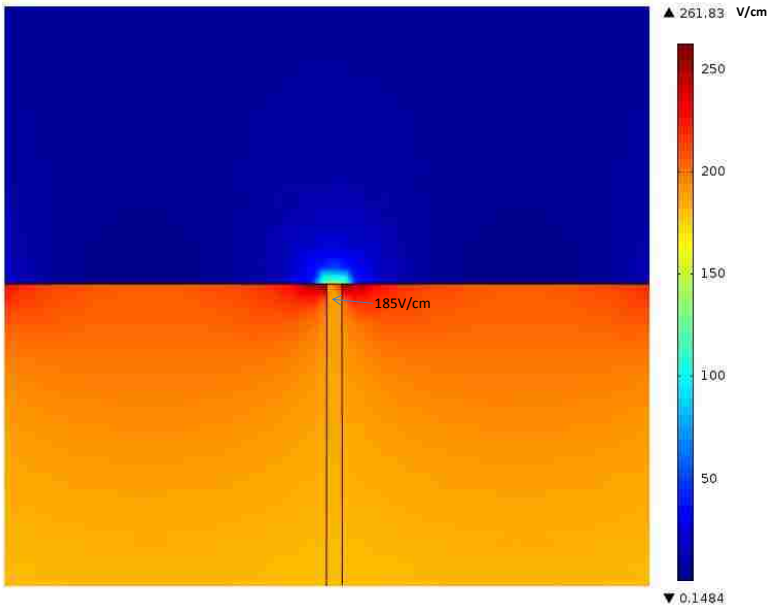

Figure 2.8 COMSOL simulation of electric field (EF) distribution of the top narrow pore (20nm), magnification of Figure 2.7

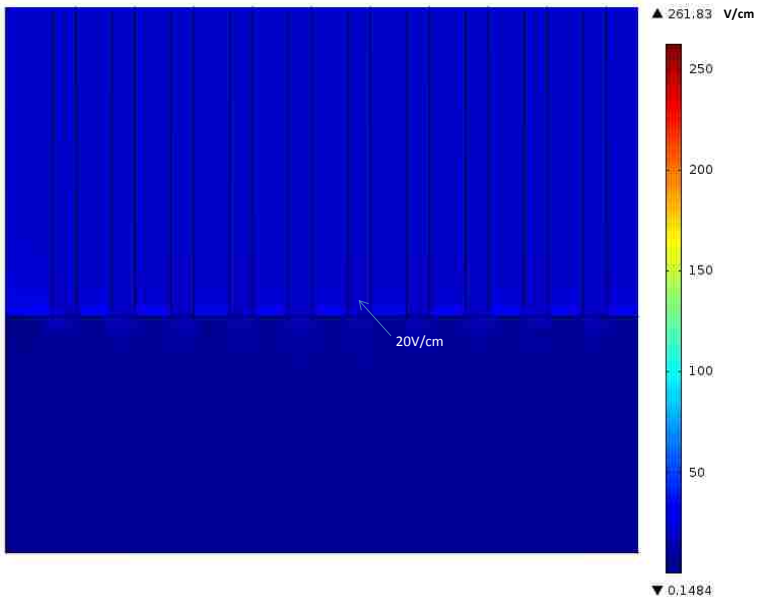

Figure 2.9 COMSOL simulation of electric field (EF) distribution of the bottom large pore (200 nm), magnification of Figure 2.7

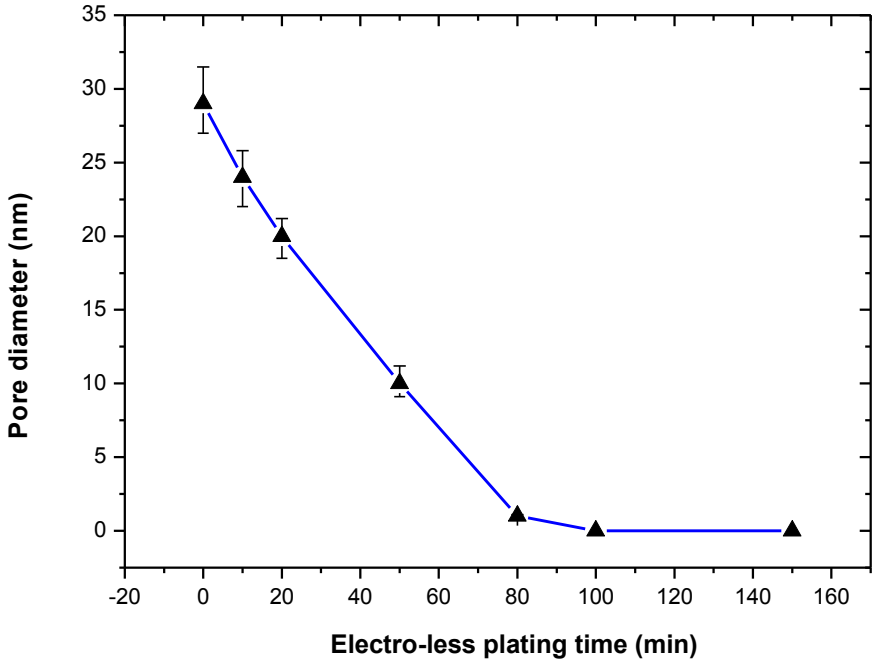

Figure 2.10 The average pore diameter of AAO membrane as a function of electro-less plating time

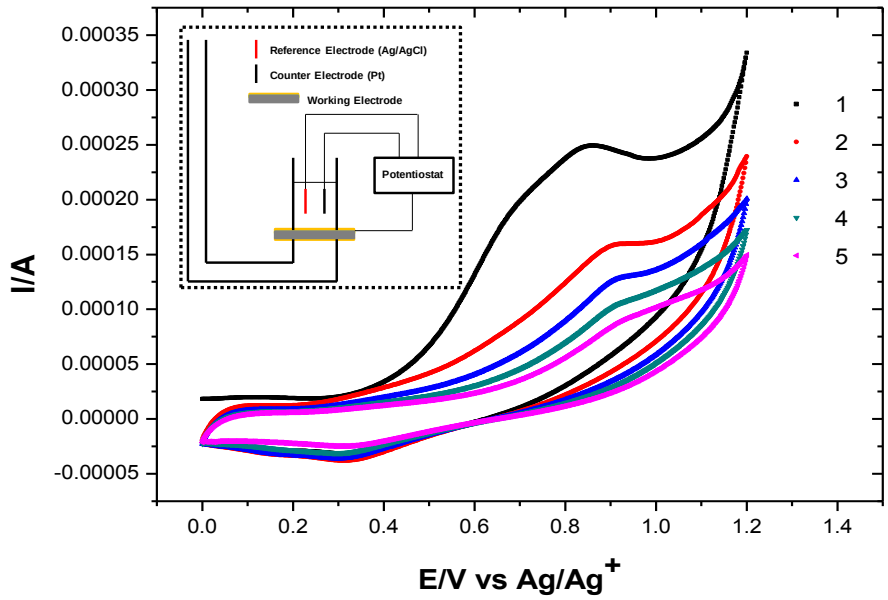

Figure 2.11 Cyclic Voltammograms on freshly gold/AAO membrane in 0.1 M LiClO4 ethanol solution with10 mM NTA for the 1) first, (2) second, (3) three, (4) fourth, and (5) fifth cycles. Scan rate is 10 mv/s. Inserted is the apparatus for grafting

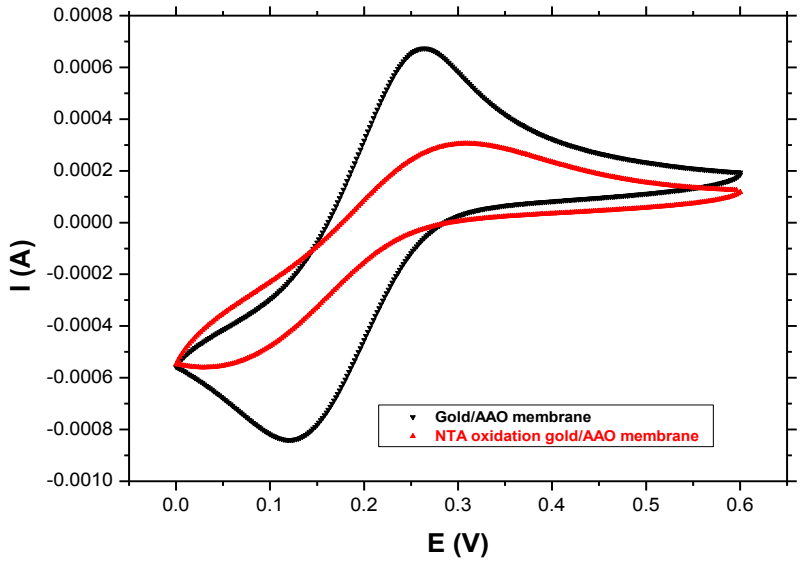

Figure 2.12 Cyclic Voltammogram of 0.1M $K_3Fe(CN)_6$ buffered by PH=7 PHOSPHATE solution on gold/AAO membrane before and after N_α, N_α-Bis(carboxymethyl)-L-lysine oxidation. Reference electrode is Ag/AgCl. Scan rate is 100mv/s.

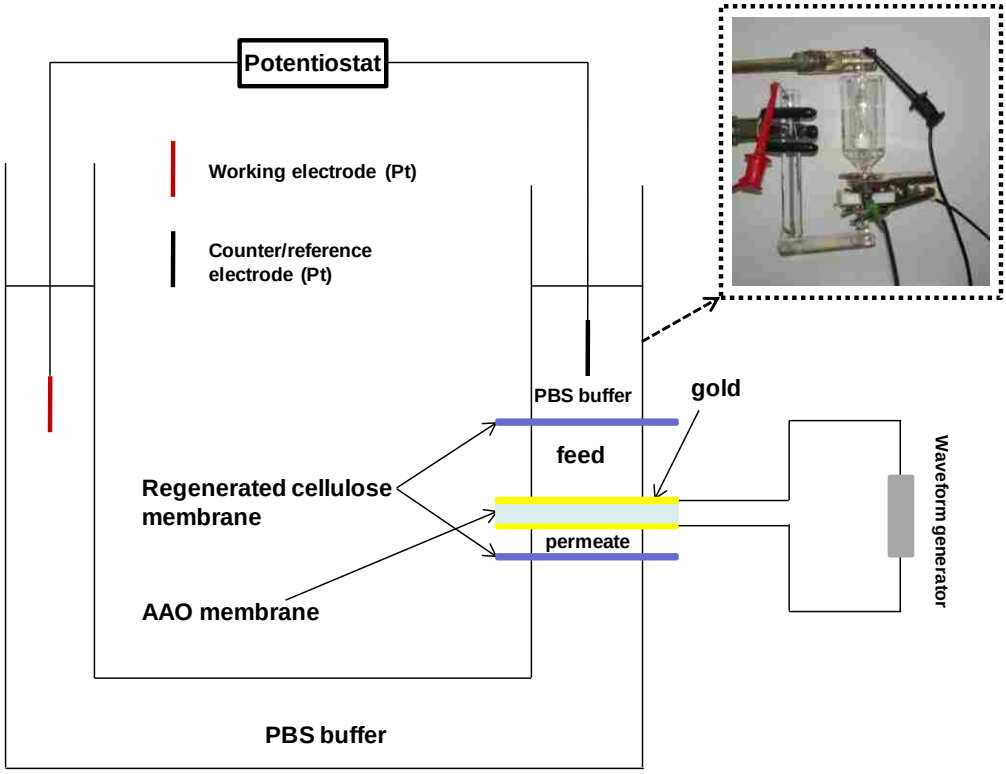

Figure 2.13 Schematic of Electrophoretic pumping cell

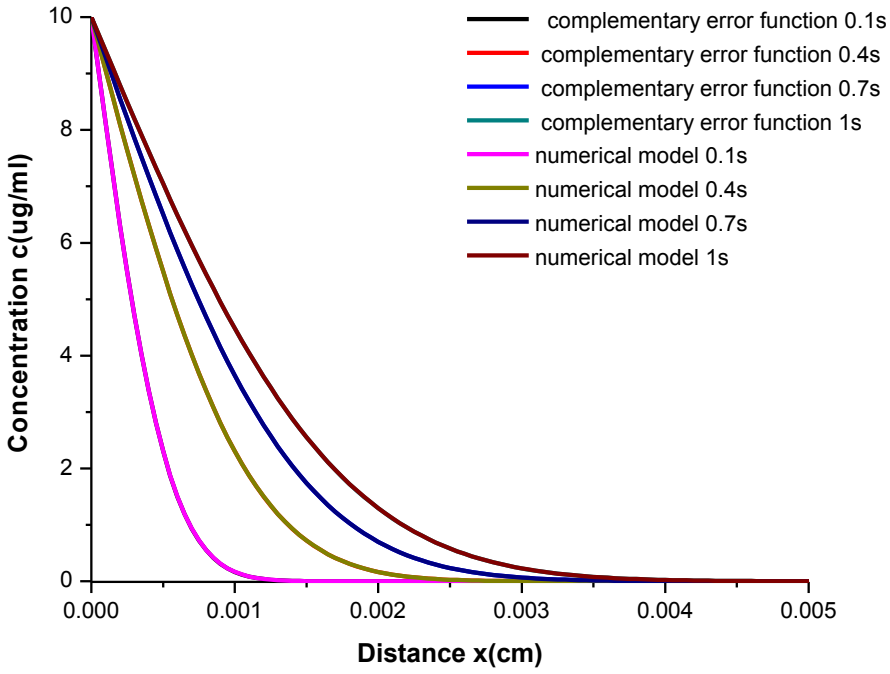

Figure 2.14 One dimension diffusion plot solved by numerical method and the analytical solution using complementary error function.

Chapter 3 : Numerical study of Two-step Continuous Affinity Protein Separation with Nanometer-Scale Membrane Electrode Systems

3.1 Introduction

There is increased demand for more efficient recombinant protein purification methods due to the rapid advances in genetic engineering [88, 89]. More than 150 recombinant proteins have been produced for pharmaceutical use by recombinant DNA technology since the first well-known human insulin approved by Food and Drug Administration (FDA) in 1982 [90]. In order to simplify recombinant protein purification and detection, affinity tags such as polyhistidine or glutathione-S-transferrase (GST) are often fused to the recombinant protein [91]. As the most wildly used tags, polyhistidine can form specific chelation bond with Ni^{2+} complex, enabling affinity purification by immobilized metal ion affinity chromatography (IMAC)[92, 93]. In a typical IMAC process, recombinant protein with His_6-tag is retained within the Ni^{2+} functionalized resin while other proteins are washed away. The bound recombinant protein is then eluted with concentrated imidazole. As dominate recombinant protein purification method, IMAC is favorable due to its mild operation condition [94]. However, IMAC suffers from limitations of long intra-particle diffusion time, high pressure drops, column regeneration, high cost and long binding/purge cycles [95, 96].

Recently, extensive studies have been carried out on membrane chromatography [97, 98] owe to its enhanced mass transport rate across the membrane pore compare to IMAC. However, the major challenge for membrane chromatography is low binding capacity due to low membrane surface area. Bruening and other researchers functionalize porous membranes with polymer brushes with multiple protein-binding sites to greatly increase

the binding capacity [99, 100]. However the operation of membrane chromatography is similar to IMAC, requiring multiple-step binding/release cycles.

The needed process would be an automated and efficient recombinant protein purification process. In our previous paper [101], we developed a pulse pumping technique for the continuous separation of His-GFP from the BSA and His-GFP mixtures based on alternate binding/repel and releasing/pumping cycles. During the binding cycle, a small positive bias was applied on top Ni-NTA/gold surface to attract anionic His-GFP and repel imidazole from the binding surface and pumps it to the permeate side; During the releasing/pumping cycles, concentration of imidazole is controlled to keep the pore blocked while releasing proteins at the bottom edge of the electrode by applying a opposite bias in the outside compartments. However, the GFP releasing kinetic study and imidazole pumping process are needed to further optimize this pulse pumping system to increases protein separation efficiency and protein purity.

This work describes the study of the pulse pumping conditions through the examination of GFP releasing kinetic and the numerically study of imidazole concentration during the pulse pumping cycles. The imidazole induced His-GFP releasing kinetic was first studied under a real-time fluorescence microscopy. His-GFP releasing kinetic data was then coupled with the numerically simulated imidazole concentration during the pulse pumping cycle to get the optimal pumping conditions, followed by experimental validation of the numerical study. A separation factor for GFP: BSA of 9.7 was achieved with observed GFP electrophoretic mobility of $3.1 \times 10^{-6}\ cm^2\ s^{-1}\ V^{-1}$ at 10 mM bulk imidazole concentration and 14s/1s pumping/repel duration. At higher bulk imidazole concentration (20 mM) and lower pumping duration (7s/1s pumping/repel

duration), high GFP electrophoretic mobility and low protein selectivity was seen due to inefficient pore blocking; At lower bulk imidazole concentration (5 mM) and higher pumping duration (23s/1s pumping/repel duration), low GFP electrophoretic mobility and high protein selectivity was seen due to longer pumping duration thus lower efficiency. The purification of His_6-OleD Loki variant directly from crude *E. coli* extracts expression broth was demonstrated using the pulse pumping process, simplifying the separation process as well as reducing biopharmaceutical production costs. The enzymatic reactions showed that His_6-OleD Loki was still active after purification.

3.2 Experimental details

3.2.1 Materials

20 nm Anodic Aluminum Oxide (AAO) membranes (60 um thick) were obtained from Whatman (GE Healthcare). These AAO membranes are asymmetric with a bulk pore structure comprised of 200 nm diameter straight channels and a thin porous layer at the top with a diameter of 27 nm. The porosity was ~40-60%. Gold (I) thiosulfate (Alfa Aesar) was used to electro-less deposit gold electrodes at the entrance and exits of these membranes. $NiCl_2$, N-[Nα,Nα-Bis(carboxymethyl)-L-lysine]-12-mercaptohexadecanamide (NTA) (Sigma Aldrich) and Ascorbic acid (EM Science) were used as received. Bovine serum albumin (BSA, pI=4.9, MW=67 000) was purchased from Sigma Aldrich and used as received. Texas red conjugated BSA was purchased from Life Technologies Aldrich and used as received. His-tagged green fluorescence protein (His-GFP, pI=5.7, MW=28 000) was obtained from Millipore and used as received. Uridine Diphosphate (UDP), UDP- α - D –glucose, 2-chloro-4-nitro-phenyl-β-

D-glucopyranoside (PNP-Glc),4-methylumbelliferone (4-Me-Umb), Vancomycin aglycon were purchased from were purchased from Sigma-Aldrich (St. Louis, MO, USA) or New England Biolabs (Ipswich, MA, USA). Purified water was prepared using a Millipore Milli-Q water purification system with 18.0 MΩ.cm resistivity. Regenerated cellulose membranes (molecular weight cutoff 3500) were purchased from Spectrum Laboratories, Inc. These regenerated membranes were rinsed with water for 1h to remove glycerine before use.

3.2.2 His-GFP releasing kinetic study

Glass cover slips pre-cleaned with KOH were immersed in 0.01% acetic acid containing 2% (vol/vol) 3-glycidyloxypropyl-trimethoxysilane (Sigma-Aldrich) for 3h at 90 ℃ and washed with water. The glass was incubated in 0.01 M $NaHCO_3$ (pH 10.0) containing 50 mM Nα,Nα-Bis(carboxymethyl)-L-lysine hydrate (Sigma-Aldrich) for 16 h at 60 ℃ and washed with water. Then, the glass was incubated in 10mM $NiCl_2$ and 5mM glycine (pH 8.0) for 2 h at room temperature, washed with water, and stored in water until use. UV activated glue was used to adhere the functionalized coverslips to a 35mm Petri dish with an opening in the center to construct a dish with the functionalized coverslip as the glass bottom. 10 g/mL of GFP containing a 6xHis tag was added to the coverslips and allowed to incubate for 30 minutes. The dish was then rinsed with phosphate buffered saline to remove unbound GFP. After removal of excess GFP, a small amount of buffer was added to each dish to keep solution on the coverslip. Samples were imaged with objective style total internal reflection fluorescence (TIRF) microscopy. GFP bound to the surface of the functionalized coverslip via nickel NTA were excited with a 488 nm DPSS laser (1.05 W/cm^2) through the objective (Olympus, 1.49NA 60xoil

immersion). Excitation light was directed toward the objective using the appropriate dichroic and the same dichroic directed emission light through the appropriate filter to an electron multiplying charge coupled device (EMCCD) (Andor iXon Ultra 897). To obtain total internal reflection (TIR), the laser was focused on the back aperture of the objective lens and the angle was adjusted using a stepper motor to translate the beam laterally across the objective lens. An auto-focus (Olympus, Model: IX2-ZDC2) was employed to keep the focus constant and minimize focal drift. A buffered solution of imidazole was added at time zero and then the fluorescence intensity was measured continuously for 120 seconds with a 200 ms frame rate. Fluorescence intensity was collected independently for each coverslip which were exposed to varying concentrations of imidazole. The decay curve of intensity versus time was constructed to determine the rate of departure of GFP from the surface. The photobleaching rate was determined by continuously collecting images of the fluorescence intensity in the absence of imidazole during laser excitation. The decay in the fluorescence intensity due to photo bleaching was used to correct the fluorescence decay curve due to departure of GFP from the substrate surface.

3.2.3 Gold Electrodes/AAO membrane Preparation

The membrane/electrode preparation was same as previous study [101]. Briefly, gold sputtering was first performed to create gold seed for the gold electro-less plating. Sputtering was performed with a Cressington Coating System (Ted-Pella) with calibrated quartz crystal monitor with background pressure of 0.02 mbar at 100W power supply. No intermediate wetting layer (i.e. Ti/TiO_2) on Al_2O_3 was needed for seeding the Au layer. 5 nm gold was sputtered on both the entrance and exit of AAO membranes at 1nm/min gold sputtering rate, which would deposit the diameter (20 nm for the entrance and 200

nm for the exit) distance down the pore. The gold Electro-less plating reactions will only form on the sputtered gold seed. Electro-less plating[38] was accomplished in 50 mM pH 7.0 phosphate buffer containing 1.6 mM sodium gold (I) thiosulfate and 2.68 mM ascorbic acid. The oxidization and reduction reactions are given by

$$C_6H_8O_6 \longrightarrow C_6H_6O_6 + 2e^- + 2H^+$$

$$Au(S_2O_3)_2^{3-} + e^- \rightleftharpoons Au + 2S_2O_3^{2-}$$

The pore size can be tuned by controlling the electro-less plating time. The AAO membrane pore entrance size was measured by the analysis of images from a Hitachi S-4300 Scanning Electron Microscope (SEM).

3.2.4 Gold Electrodes/AAO Membrane Functionalization

NTA Self-assembled [102] monolayer was prepared by incubation of gold with 1 mM NTA ethanol solution at room temperature for 24h followed by rinsing with ethanol for 3 min and dried under N_2 stream. The membrane was incubated with a 0.5M $NiCl_2$ aqueous solution for 24 h at room temperature followed by rinsing with Milli-Q water for 3min and dried under N_2 stream.

3.2.5 Protein Separation Experiments

Two model proteins used for separation are His-GFP and BSA. His-tagged GFP has Eleven strands on the outside of cylinders form the walls of the structure. The cylinders have a diameter of 30 Å and a length of 40 Å. BSA is also a cylinder with a diameter of 55 Å and a length of 90 Å. The setup for protein pumping process was shown in Figure

3.15. In direct electrophoretic pumping, only the potentiostat (EA164 QuadStat, eDAQ Pty Ltd), which is controlled by an e-corder 410 (eDAQ Pty Ltd) with Chart^{TM} software, was used and placed on the outer cell. Two Pt wires (one connected to the working electrode and the other one connected to the counter and reference electrode) were connected to the potentiostat and inserted into the outer electrolyte phosphate buffer (50mM, PH=7) solutions. Two regenerated cellulose membranes (3500) were used in the experiment. BSA (67 000) and GFP (28 000) were restricted in the feed and permeate solution by the regenerated cellulose membranes (3500), which kept the proteins from oxidation or reduction by high voltages (6 V) generated at the Pt electrodes. At PH 7, both GFP and BSA were negative charged. The anode was in the Phosphate buffer adjacent to the permeate solution so that the negative charged proteins will be electrophoretically pumped to the permeate solution and the positively charged imidazole will be electrophoretically pumped to the feed solution from the permeate solution. When a 6 V was applied by the potentiostat, the voltage drop directly measured across the gold electrodes/AAO membrane was 0.3 V. Water underwent electrolysis and generated H^+ in the anode and OH^- in the cathode at 6 V in the outer compartments and phosphate Buffer was changed frequently to maintain the PH during the water electrolysis process. The volume of feed solution was ~1ml and the permeate solution was ~0.5 mL. The feed solution contained 5 g/mL Texas red conjugated BSA and His-tagged GFP and the permeate solution contained 0.1-10 mM imidazole. In the pulse electrophoretic pumping process, a waveform generator (keithley 3390 50 MHz arbitrary waveform generator) was also used to generate 0.05 V on the gold/electrodes/AAO membrane during the binding cycle. The potentiostat was used to generate 0.3 V on the gold/electrodes/AAO

membrane during the release/pumping cycle. The feed solution contained 5 g/ml Texas red conjugated BSA and His-tagged GFP.

3.2.6 Protein assay methods

The fluorescence intensity of His-GFP was measured using a fluorescence spectrophotometer (BioTek® Synergy H1 Hybrid Reader), with an excitation filter of 395 nm and an emission filter of 509 nm. The fluorescence intensity of Texas red conjugated BSA was measured with an excitation filter of 596 nm and an emission filter of 615 nm. The fluorescence intensities of the experimental samples were compared to the five–point standard curves of His-GFP and Texas red conjugated BSA.

3.2.7 Protein Expression

Protein purification protocol was the same as previous published methods[101]. Briefly, cell pellets from standard heterologous overproduction of OleD Loki in E. coli were collected by centrifugation (6,000 xg at 4 ℃ for 20 min), resuspended in 2.5 mL of chilled lysis buffer (20 mM phosphate buffer, pH 7.4, 0.5 M NaCl, 10 mM imidazole), and lysed by sonication (5 pulses of 1 minute each) in an ice bath. Cell debris was removed by centrifugation (10,000 g at 4 ℃ for 20 min) and in the resulting crude extracts was loaded into pumping system.

3.2.8 HPLC method

HPLC was conducted with an Agilent 1260 system equipped with a DAD detector with a 250 mm x 4.6 mm Gemini-NX 5μm C18 column (Phenomenex, Torrance, CA, USA) and using a linear gradient of 1% B to 71% B over 30 min, 71% B for 5 min, 71%

B to 1% B over 1 min, 1% B for 4 min (Solvent A = 50 mM PO_4^{2-}, 5 mM tetrabutylammonium bisulfate, 2% acetonitrile [pH adjusted to 6.0 with KOH]; Solvent B = acetonitrile; flow rate = 1 ml min^{-1}; A254 nm;). Regardless of method, HPLC peak areas were integrated with Star Chromatography Workstation Software (from Varian, Palo Alto, CA, USA) and the percent conversion calculated as a percent of the total peak area.

3.2.9 Physical parameters for the numerical simulation

His-GFP bulk mobility: 7.5E-05 $cmV^{-1}s^{-1}$

His-GFP bulk diffusion coefficient: 8.7E-07 cm^2/s

His-GFP diffusion mobility within the pore: 2.5E-06 $cmV^{-1}s^{-1}$

His-GFP diffusion coefficient within the pore: 6.25-08 cm^2/s (Einstein relation)

Imidazole mobility: 1.44E-04 $cmV^{-1}s^{-1}$

Imidazole diffusion coefficient: 3.6E-06 cm^2/s (Einstein relation)

Time step(Δt): 5E-5 s

(Dt)^0.5+ cEut = 4.3E-6cm (must be less than Δx)

Distance step(Δx): 5E-5 cm

Electric field within the membrane during pumping cycle: 50 V/cm

Electric field outside the membrane during the pumping cycle 1V/cm

Electric field within the membrane during repel cycle: 8.3 V/cm

Electric field outside the membrane during the repel cycle 0 V/cm

Bulk pore porosity (10.5 μm to 70 μm): 50%

Porosity at the top thin porous electrode layer (10.0 to 10.5 μm): 10%

Porosity at the top thin porous electrode layer after protein blocking (10.0 to 10.5 μm): 2%

Initial conditions:

0-10 μm: 5 μg /ml His-GFP

10-70 μm: 0 μg/ml His-GFP

0-70 μm: 0 mM imidazole

70-80 μm: 10 mM imidazole

Boundary conditions:

Constant 5 μg/ml His-GFP at distance 0 μm for bulk feed solution.

Constant 0 mM imidazole at distance 0 μm for bulk feed solution.

Constant 0 μg/ml His-GFP at distance 10-10.5 μm (above membrane surface) for binding cycle

Cumulative amount of protein flux is saved as a variable stepwise

During the pumping, imidazole reaches steady state concentration cycle in 3s.

46% of absorbed protein on the membrane surface is then first quickly released in 2s.

12% of the absorbed protein on the membrane surface is finally slowly released in 9s.

Constant 10 mM imidazole at from 70-80 μm of bulk permeate

3.3 Results and Discussion

Nanometer-scale membrane electrode is the primary active area for the pulse pumping system. Gold sputtering followed by gold electro-less plating at the pore entrance was used to fine-tune the initial 27 nm AAO membrane pore size to protein-scale pore size (~10 nm). This is important that His-GFP bound to the electrode can effectively block these protein-scale pores during the binding cycle (Figure 3.1), stopping other protein mixtures entering the electrode pore. Unlike previous electrochemical grafting of Nα, Nα-Bis(carboxymethyl)-L-lysine onto the gold electrode, self-assembled monolayer technique was used to form more dense and uniform NTA on the electrode

surface. Ni^{2+} ligand that specifically captures His-GFP was then bound to the monolayer NTA for pulse pumping cycles. During the binding/repel cycles, a small voltage was directly applied on the electrodes surface to repel the imidazole from the electrode surface and capture the His-GFP at the same time; during the pumping/releasing cycles, a larger voltage was applied on the outside compartment to pump imidazole from the permeate side to the feed electrode surface to release the bound His-GFP and subsequently pump the His-GFP to the permeate side (Figure 3.2). To obtain the optimal pumping/releasing duration, it is necessary to study the His-GFP releasing kinetic by different concentration imidazole.

To study the imidazole induced His-GFP releasing kinetic, a real-time fluorescence microscopy was used to record the His-GFP that is bound on Ni-NTA-Glass surface. The NTA chemistry was immobilized over glass surface according to established protocols [102] with minor modifications followed by Ni^{2+} attachment (Figure 3.3).

His-GFP will then form covalent bond with the NTA-Ni chemistry on the glass. The amount of His-GFP bound on the Ni-NTA-glass can be determined by the fluorescent intensity recorded using the real-time fluorescent microscopy. When different concentration imidazole solution is poured into the glass container surface, His-GFP will be released from the Ni-NTA-glass surface at different rate and diffuse into bulk solution, which will be recorded as fluorescent intensity reduction under the fluorescent microscopy. The imidazole induced His-GFP releasing kinetic was shown in Figure 3.4, which is similar to the previous reported data [103]. Specifically, from Figure 3.4 we can see that 2 mM imidazole concentration is not high enough to release the bound His-GFP. As the imidazole concentration increases to 27 mM, it takes about 20s to the release half

His-GFP from the Ni-NTA-glass surface. Further increasing imidazole concentration will further lower the releasing time of His-GFP from the glass surface. It takes about 11s, 4s and 1s to release 60% of His-GFP from the glass surface using 54 mM, 109 mM and 169 mM imidazole concentration respectively. To more realistically simulate the protein release process, the His-GFP releasing kinetic is manually divided into two parts-fast linear releases within the first 2 s and slow linear release after 2 s, as shown in Figure 3.5. The fast and slow release rates were estimated from Figure 3.4 using linear approximation within the first 2 s and after 2 s respectively.

The imidazole concentration distribution during the pumping/releasing cycle is important to determine the pulse pumping condition. AAO membranes are asymmetric structure with a thin top layer of 27 nm diameters and bulk pore structure comprised of 200 nm channel. The electro-less plating and bound of His-GFP on the top electrode entrance will shrink the original porosity from 50% to 10% and a final estimated 2% porosity after protein blocking, which will leads to the accumulation of imidazole at the binding site during electrophoretic pumping (Figure 3.2). Detailed imidazole concentration distribution during the pumping process can be by solving a combination of Fick's 1st law of diffusion and electrophoretic pumping shown in Equation (1) using Microsoft Excel with Visual Basic Macros.

$$J = D\frac{\Delta c}{\Delta x} + uEc \qquad [1]$$

Where J is flux per unit area, c is concentration, D is diffusion coefficient, and u is mobility, E is the electric field and Δx is the step width of simulation cell size (0.5 μm).

The concentration change in the calculation cell is given by Equation (2)

$$\Delta c = J_{in} \times \Delta t \times \varepsilon_{rel}/\Delta x - J_{out} \times \Delta t \times \varepsilon_{rel}/\Delta x \quad [2]$$

Where Δt is numerical simulation time step ($5x10^{-5}$ s). J_{in} is flux (/unit area) in from neighbor cells and J_{out} flux out to neighbors calculated from Equation (1). Here ε_{rel} is the relative porosity of calculation cell with respect to neighbor cell. $\Delta c = J_{in} \times \Delta t \times \varepsilon_{rel}/\Delta x - J_{out} \times \Delta t \times \varepsilon_{rel}/\Delta x$ A matrix of 160 x-values (0-80 μm, 0.5 μm steps) was initialized with boundary conditions and starting profiles. A new matrix was made for the new time (previous time + time step). Flux to/from neighbor cells into new matrix was calculated using Equation (1). The concentration change in the cell can be calculated from Equation (2) using the values in the matrix of the prior time step. After calculating each new concentration at x location, the prior time step matrix is overwritten with the newly calculated matrix and the cycle repeated until desired total time is reached using 'For/Next' loops in Visual Basic. Time steps were chosen to be such that $(D\Delta t)^{0.5}$ + $cE\mu\Delta t$ (characteristic diffusion length + electrophoretic distance) was much less than Δx (typically $0.1*\Delta x$) to ensure numerical accuracy and stability. Detail physical parameters in the model can be found in the experiment section.

Figure 3.6 shows the imidazole concentration distribution at different time during the pumping cycle. The imidazole concentration at the 50% porosity cell next to the 2% porosity cell is calculated by Equation (3)

$$C_{new}(j) = C_{old}(j) + [(C_{old}(j+1) - C_{old}(j))/\Delta x \times D + C_{old}(j+1) \times \mu \times e_1] \times \Delta t \times/\Delta x - [(C_{old}(j) - C_{old}(j-1))/\Delta x \times D + C_{old}(j) \times \mu \times e_1] \times \Delta t \times (\frac{0.02}{0.5})/\Delta x \quad [3]$$

where C_{old} is old cell concentration, C_{new} is new cell concentration after time-step, $e_1 = 50\ \mathrm{V/cm}$ is the electric field within the membrane during the imidazole pumping

cycle, D is the diffusion coefficient and μ is the electric mobility. Imidazole concentration in the permeate side is set to be constant 10 mM during the pumping process. As we can see from Equation 3, the incoming imidazole flux is much higher than the outgoing imidazole flux due to the porosity difference at the intersection, leading to imidazole accumulation at this area. With a 10 mM bulk imidazole concentration, the accumulated imidazole concentration is around 54 mM at the pore entrance electrode. The imidazole concentration reaches steady-state 54 mM in 3s. The high concentration imidazole at the entrance electrode is good for the quick releasing of bound protein. It should be noted that the boundary conditions during the simulation have great effect on the simulation results. Figure 3.16 is the imidazole simulation results with constant imidazole concentration at distance 120 μm and 5 unit 2% cells at the electrode entrance. Once bound protein is released from the entrance electrode, the high concentration imidazole needs to be repelled away for the subsequent His-GFP binding cycle. An opposite small voltage directly applied on two electrode surface is used to repel the high concentration imidazole to bulk concentration.

Figure 3.7 shows the imidazole concentration distribution at different time during repel cycle right after imidazole accumulated cycle. The imidazole concentration during the repel cycle is calculated by Equation (4)

$$C_{new}(\mathrm{j}) = C_{old}(\mathrm{j}) + [(C_{old}(\mathrm{j}-1) - C_{old}(\mathrm{j}))/\Delta x \times D + C_{old}(\mathrm{j}-1) \times \mu \times e_2] \times \Delta t \times/\Delta x - [(C_{old}(\mathrm{j}) - C_{old}(\mathrm{j}+1))/\Delta x \times D + C_{old}(\mathrm{j}) \times \mu \times e_2] \times \Delta t \times/\Delta x \quad [4]$$

Where $e_2 = 8.3\ \mathrm{V/cm}$ is the electric field within the membrane during the imidazole repelling cycle. As shown in Figure 3.7, the imidazole concentration at the electrode/membrane entrance is rapidly repelled to a concentration lower than bulk

imidazole concentration in 0. 5s. Steady-state imidazole concentration during the repel cycle at the electrode entrance is shown in Figure 3.8.

Combined the imidazole numerical simulation data with the His-GFP releasing kinetic data, it is now possible to predict the optimal pulse pumping conditions. Steady-state imidazole concentration during the pumping cycle at the electrode entrance is shown in Figure 3.9. The highest imidazole concentration at the membrane/electrode interface is roughly 5.4 times higher than the bulk imiadzole concentration. By changing the bulk imidazole concentration, the accumulation imidazole concentration at the electrode point will change accordingly. This simulated imidazole concentration at the electrode entrance can be coupled with the His-GFP releasing kinetic (Figure 3.3) to predict the optimal pumping durations. At low imidazole concentration, it will take longer time for the GFP releasing from the electrode, resulting low protein pumping efficiency; at high imidazole concentration, it will take shorter time for the GFP releasing from the electrode, resulting high protein pumping efficiency. However, if the imidazole concentration is too high, His-GFP can't block the pore efficiently and other protein mixtures will enter the pore, resulting low purity His-GFP.

Specifically, if the bulk imidazole concentration is 10 mM, the resulting imidazole concentration at the entrance would reach steady-state 54 mM concentration in 3 s. From Figure 3.3 we can see that it takes about 5 s, 11s and 20s respectively to release 50%, 60% and 70% of bound His-GFP from the Ni-NTA-Glass. So the estimated pumping duration would be 8 s, 14 s and 23 s since it takes about another 3 s to reach the steady-state concentration.

Table 1 summarized different pulse pumping conditions and the resulting protein separation efficiency and selectivity. When 10 mM bulk imidazole concentration was used, 8 s/1 s, 14 s/1 s and 23 s/1 s pumping/repel condition was experimental studied. A separation factor of 10.6 was seen with 8s/1s pumping/repel duration, however, the His-GFP effective mobility was low (1.69×10^{-6} cm^2 s^{-1} V^{-1}) due to insufficient release of His-GFP (50%) from the electrode entrance. A separation factor as low as 3.1 was seen with 23 s/1 s pumping/repel duration, due to over release of His-GFP (70%) thus inefficient pore blocking. Both relative high His-GFP effective mobility and protein separation factor was seen when the pumping/repel duration was 14s/1s. At this pumping condition, 60% of bound His-GFP was released, which was neither too high that the pore will be open nor too low that the insufficient release causes low efficiency. Triple experiments was carried out in this pumping condition with an average $3.1\times10^{-6}$$cm^2$ s^{-1} V^{-1} His-GFP effective mobility and 8.3 separation factor. Increasing the repel duration to 2s didn't increase the separation factor (Table 3.1) due to the already rapidly repelled imidazole within 1s.

To further explore optimal pulse pumping conditions, different concentration bulk imidazole was also studied under the condition of releasing 60% of bound His-GFP. 7s/1s pumping/repel duration with 20 mM bulk imidazole (this will give about 108 mM imidazole concentration at the electrode entrance) concentration gave mild separation selectivity (5.3) and high mobility (5.8×10^{-6} cm^2 s^{-1} V^{-1}). This is probably because at 20 mM bulk imidazole concentration, His-GFP can't be bound to the membrane surface very efficiently, resulting inefficient blocking and releasing. Further increasing the bulk imidazole concentration to 30 mM will leads wide open pore and almost no selectivity

due to high imdazole competing with His-GFP at the electrode entrance. With 5 mM bulk imidazole concentration (this will give about 27 mM imidazole concentration at the electrode entrance), only 50% of bound His-GFP can be released from the electrode surface even after 20 s. A low GFP effective mobility (2.1×10^{-6} cm^2 s^{-1} V^{-1}) was seen when the pumping/repel duration was 23 s/1 s in 5 mM bulk imidazole concentration due to long releasing duration. 10 mM bulk imidazole concentration with 14s/1s pumping/repel conditions seems to be the best pumping conditions since both high separation factor and high His-GFP effective mobility can be obtained.

Protein binding, releasing and subsequently pumping through the membrane was also studied using numerical approach. His-GFP concentration during the protein binding cycle is calculated by Equation (5)

$$C_{new}(\mathrm{j}) = C_{old}(\mathrm{j}) + [(C_{old}(\mathrm{j}-1) - C_{old}(\mathrm{j}))/\Delta x \times D_P] \times \Delta t \times/\Delta x - [(C_{old}(\mathrm{j}) - C_{old}(\mathrm{j}+1))/\Delta x \times D_P] \times \Delta t \times/\Delta x \quad [5]$$

where D_P is the protein diffusion coefficient. As shown in Figure 3.10, during the binding cycle, protein diffused from the bulk solution and was specifically captured by the Ni-NTA chemistry at the membrane electrode/surface. His-GFP concentration at the electrode surface unit was set be to 0 μg/ml since the His-GFP was captured and immobilized on the electrode surface. During the release cycle, imidazole from the permeate sides will be pumped to the feed entrance to release the bound His-GFP. The imidazole will reach steady-state high concentration in 3s, after which bound His-GFP will be first released at high release rate during for 2s and low release rate for the rest 9s. Specially, 46% of the absorbed His-GFP (0.0019 μg) was quickly released in 2s with release rate R_1=0.000437 μg/s and 12% of the absorbed His-GFP was slowly released in

9s with release rate R_1 = 2.5×10^{-5} μg /s. His-GFP concentration during the protein releasing cycle is calculated by Equation (6)

$$C_{new}(\mathrm{j}) = C_{old}(\mathrm{j}) + C_r + [(C_{old}(\mathrm{j}-1) - C_{old}(\mathrm{j}))/\Delta x \times D_P + C_{old}(\mathrm{j}-1) \times u_p \times e] \times \Delta t \times/\Delta x - [(C_{old}(\mathrm{j}) - C_{old}(\mathrm{j}+1))/\Delta x \times D + C_{old}(\mathrm{j}) \times u_p \times e] \times \Delta t \times/\Delta x \quad [6]$$

where C_r is the added protein concentration due to the protein releasing per unit time and u_p is protein mobility within the membrane. C_r can be calculated by Equation (7)

$$C_r = \mathrm{R} \times \Delta t/(\Delta x \times S) \quad [7]$$

Where S is membrane area and R is protein release rate. Figure 11 shows His-GFP pumping concentration profile during the 14s pumping cycle with 10Mm bulk imidazole concentration.

Figure 3.12 shows His-GFP concentration profile at the end of pumping/releasing cycle as a function of different pumping cycles. His-GFP is continuously pumped from the feed side to the permeate side as the pulse pumping cycle repeat. Although during the repel cycle, His-GFP within the pore is moving backward to the feed side, however, this moving distance (1s repel with 8.3 V/cm electric field) is smaller compared to pumping distance (14s forward pumping with 50 V/cm electric field).

In an effort to demonstrate the ability to purify recombinant protein directly from cell lysate, we tried to purify the recently reported His_6-OleD Loki variant directly from *E. coli.* crude lysate. His_6-OleD Loki variant [104, 105, 106, 107] can use aromatic glycosides as efficient donors in glycosyltransferase (GTs)-catalyzed reactions for both sugar nucleotide formation (*i.e.*, the 'reverse' of a conventional GT-catalyzed reaction) and subsequent sugar nucleotide-mediated glycoside formation wherein the use of 2-

chloro-4-nitrophenyl glycoside donors also offered a convenient colorimetric screen to enable the directed evolution of enhanced GTs with broad substrate permissivity. *E. coli.* crude lysate was directly used as feed solution with 14s/1s pumping/repel duration and 10 mM imidazole in the permeate side. The final protein purity in the permeate side was determined *via* SDS-PAGE (Figure 3.13), which revealed more purified His_6-OleD Loki variant compared to crude lysate. In order to test the His_6-OleD Loki variant activity after pulse pumping purification, the enzyme specific activity was tested and compared to pure enzyme as shown in Figure 3.14. The His_6-OleD Loki variant after pulse pumping purification still keeps its enzymatic activity comparable to purified enzyme.

3.4 Conclusion

In conclusion, numerical simulation of the pulse pumping cycles coupled with His-GFP releasing kinetic was used to further optimize pulse pumping technology, enabling mimic biological membranes for efficient protein separation. His-tagged proteins bound to the pore entrance block other proteins in a sequential/hopping manner, allowing selective transport. Pulsed electrophoresis binding/release/pumping cycle allows for a continuous protein separation process with low cost and high productivity. This pulse pumping process can successfully purify His_6-OleD Loki variant directly from crude *E. coli* extracts expression broth, simplifying the separation process as well as reducing biopharmaceutical production costs. More importantly, His_6-OleD Loki was still active after purification confirmed by enzymatic reactions.

Table 3.1 Pulse pumping experiments summary

Pumping condition	10 mM imidazole; 14s/1s pumping/repel	10 mM imidazole; 14s/1s pumping/repel	10 mM imidazole; 14s/1s pumping/repel	10 mM imidazole; 8s/1s pumping/repel	10 mM imidazole; 23s/1s pumping/repel	10 mM imidazole; 14s/2s pumping/repel	20 mM imidazole; 7s/1s pumping/repel	30 mM imidazole; 4s/1s pumping/repel	5 mM imidazole; 23/1s pumping/repel
BSA effective mobility $[10^{-6}cm^2\ s^{-1}\ V^{-1}]$, u_b	0.32	0.5	0.32	0.16	0.59	0.52	1.1	2.87	0.28
His-GFP effective mobility $[10^{-6}cm^2\ s^{-1}\ V^{-1}]$, u_g	3.1	3.53	2.6	1.69	1.82	3.7	5.8	5.69	2.1
Selectivity, $S=u_g/u_b$	9.7	7.1	8.1	10.6	3.1	7.1	5.3	2.0	7.5

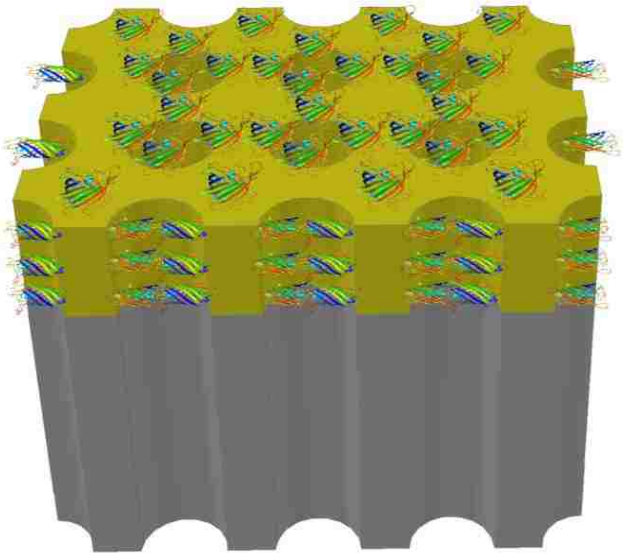

Figure 3.1 Schematic of AAO membrane blocked by his-tagged GFP pore and protein size drawn to appropriate scale

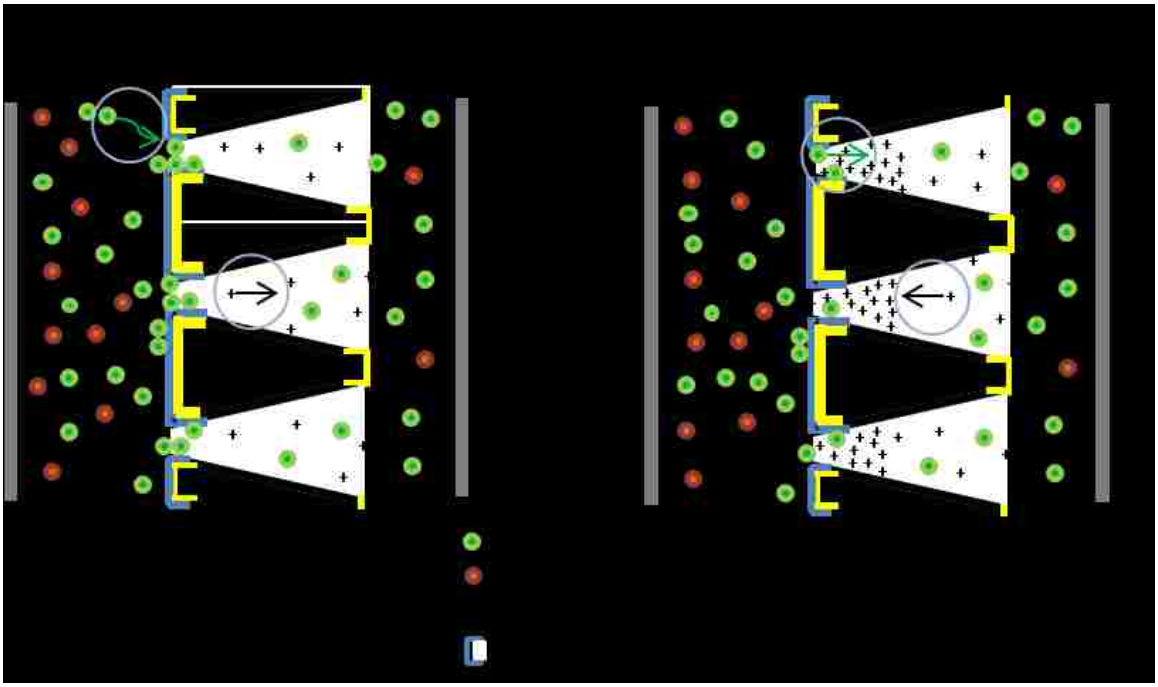

Figure 3.2 Schematic of two-step pulse pumping processes

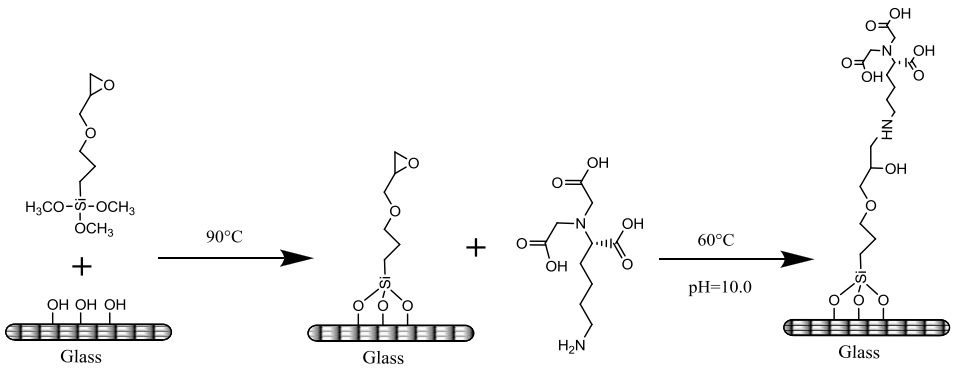

Figure 3.3 Glass surface silanization and functionalization of Nα,Nα-Bis(carboxymethyl)-L-lysine hydrate

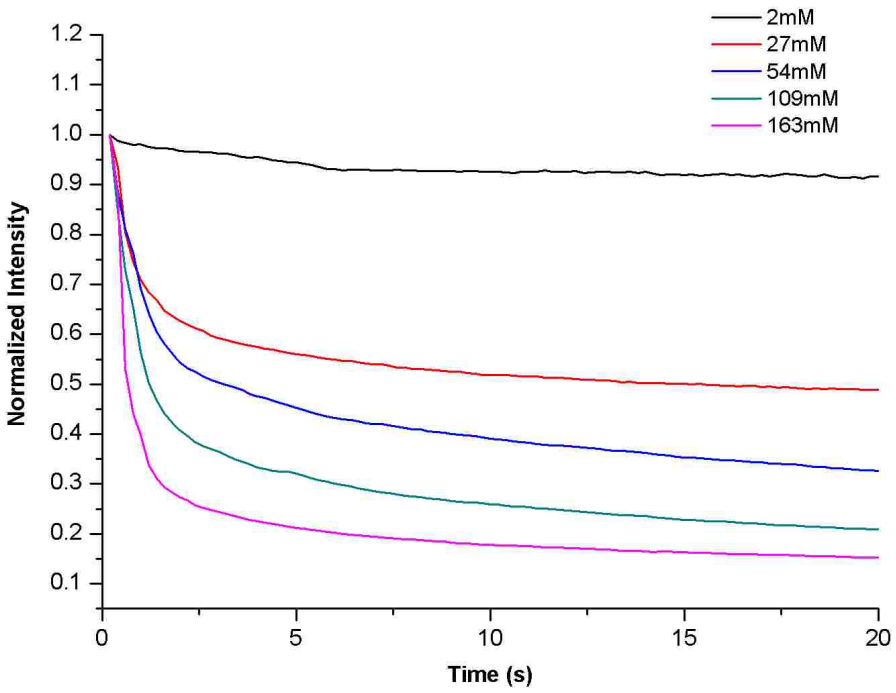

Figure 3.4 His-GFP releasing kinetic by different concentration of imidazole on the Ni-NTA-Glass surface

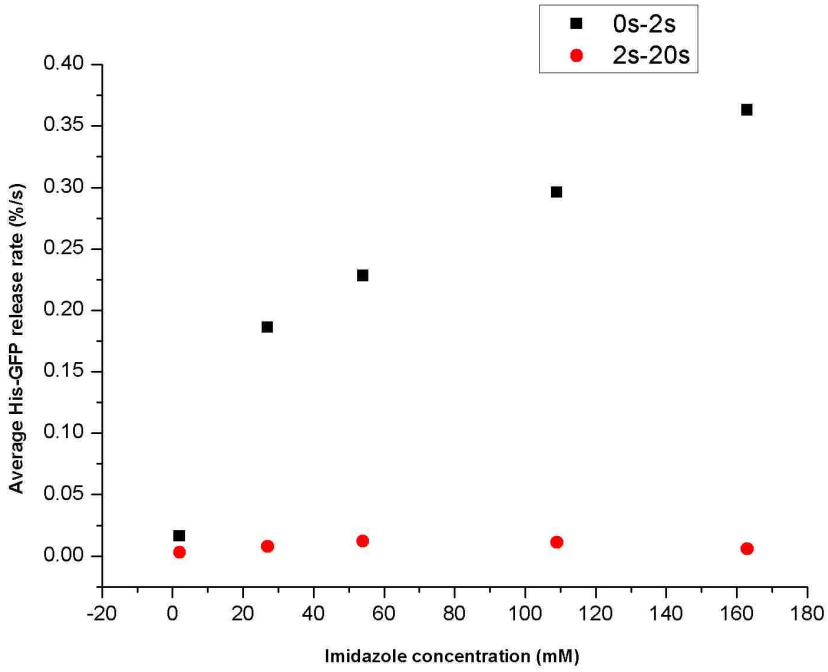

Figure 3.5 His-GFP releasing rate by different concentration imidazole

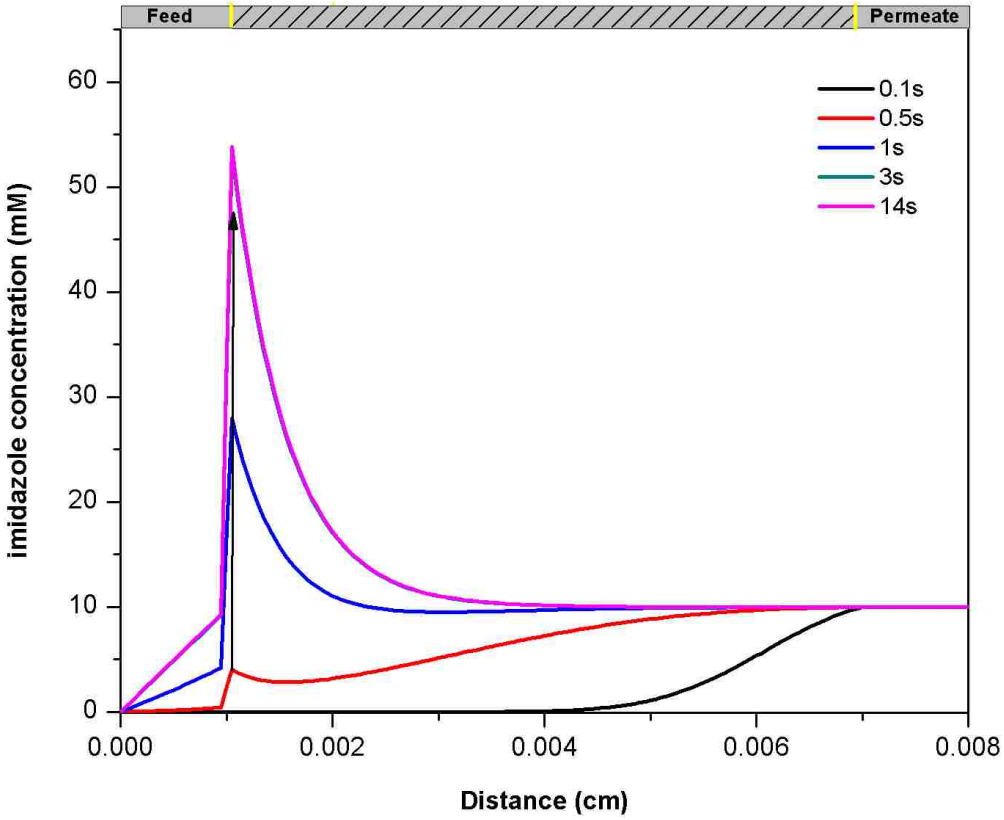

Figure 3.6 Imidazole accumulation during the protein release cycle

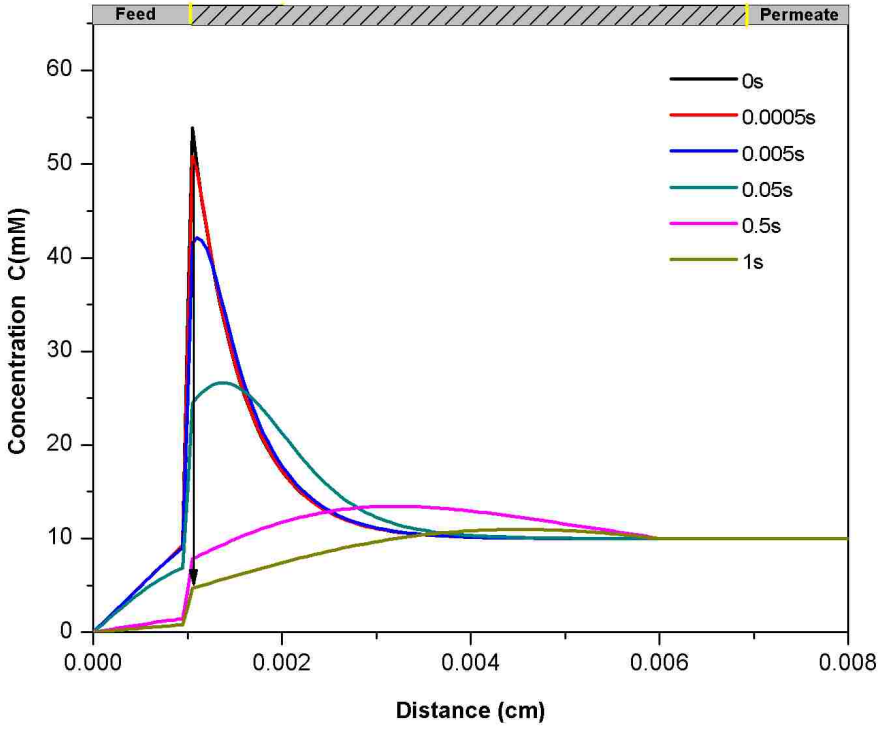

Figure 3.7 Imidazole repel during the protein binding cycle; the boundary condition here is constant 10 mM imidazole concentration in the permeate solution.

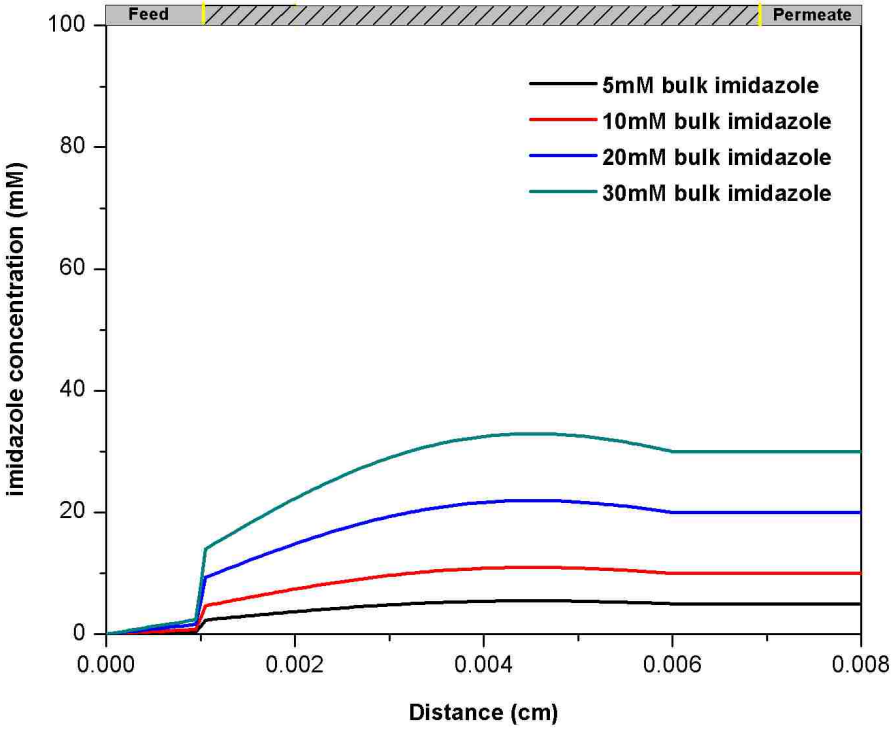

Figure 3.8 Steady state imidazole concentration at different location after 1s imidazole repel cycle; the imidazole concentration at the pore entrance is lower than the bulk imidazole concentration after 1s repel.

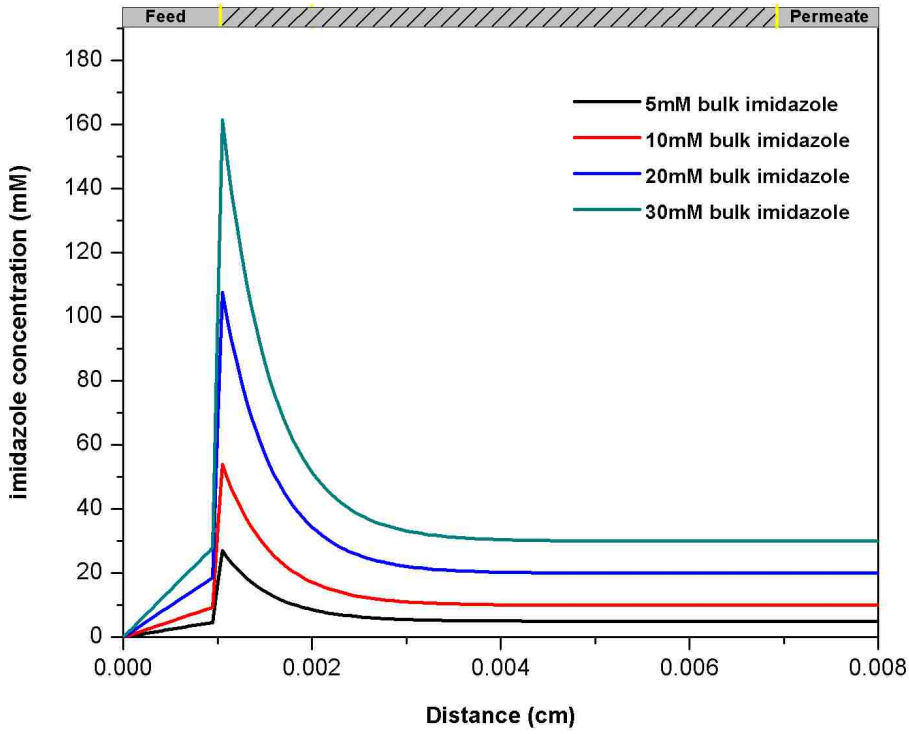

Figure 3.9 Steady state imidazole concentration at different location during the imidazole accumulation/pumping cycle

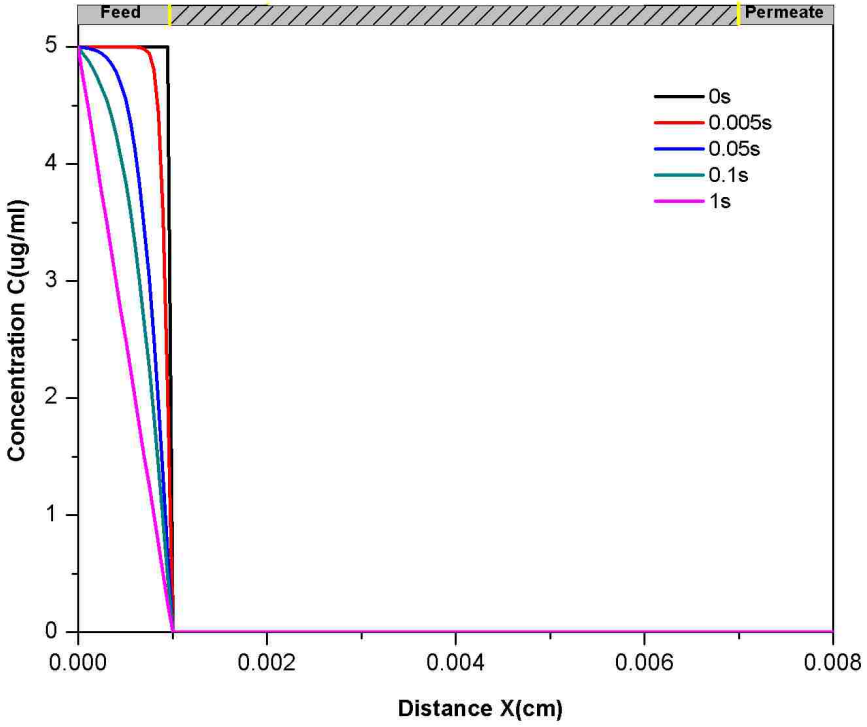

Figure 3.10 His-GFP binding concentration during the 1s binding cycle; His-GFP diffuses into the electrode surface and was actively captured by the NTA-Ni surface during the binding cycle

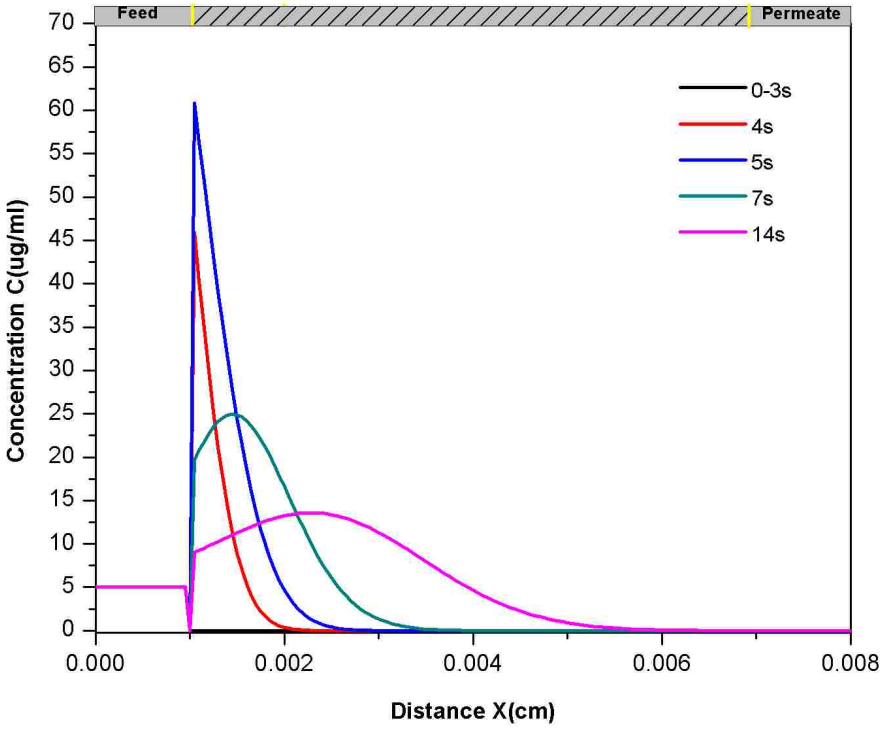

Figure 3.11 His-GFP pumping concentration profile during the 14s protein releasing/pumping cycle with 10Mm bulk imidazole concentration

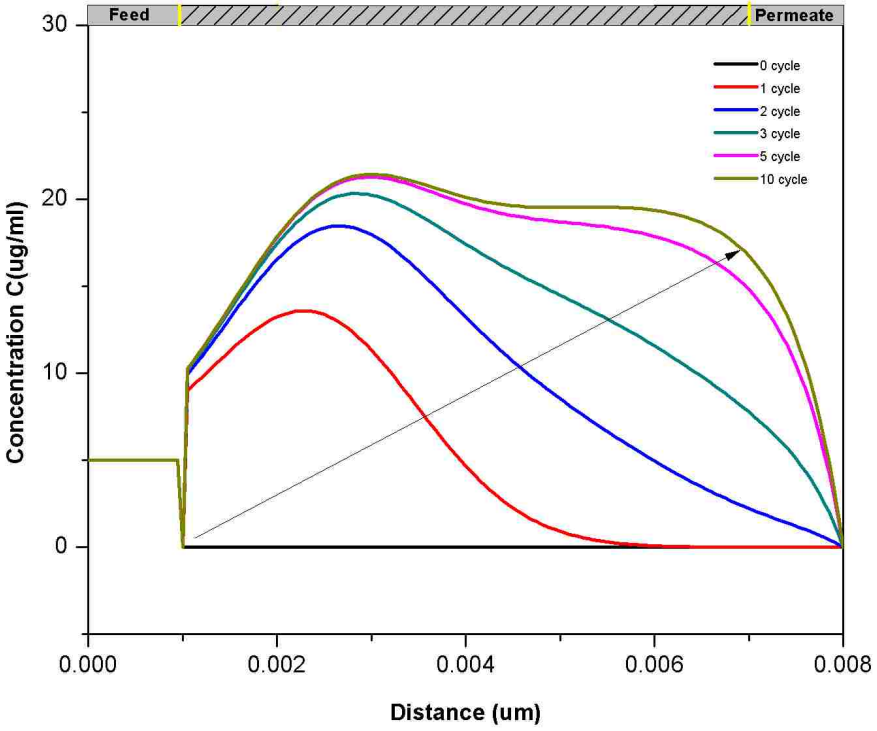

Figure 3.12 His-GFP concentration profile at the end of pumping/releasing cycle as a function of total cycle number

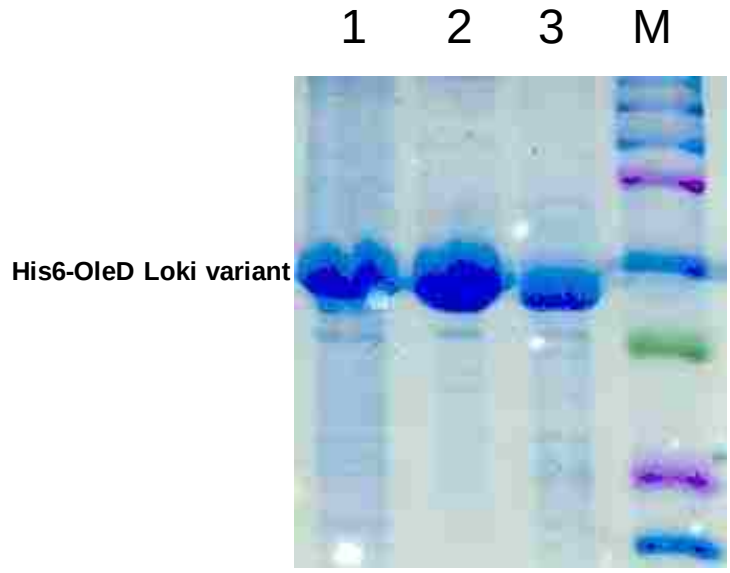

Figure 3.13 Reprehensive SDS-PAGE of OleD Loki variant purified using pulse pumping process directly from crude cell broth; Lanes: 1) 6 µg Crude lysate; 2) 6 µg His_6-OleD Loki variant purified using pulse pumping process; and 3) 6 µg pure His_6-OleD Loki variant; M) standard molecular weight markers

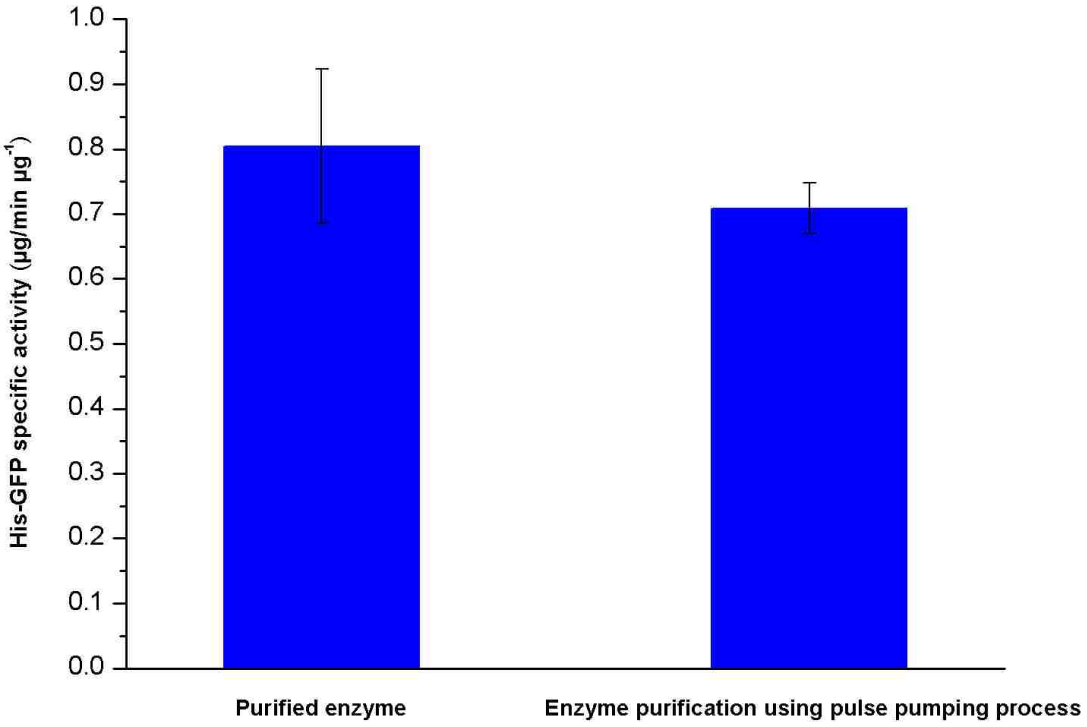

Figure 3.14 Specific activity of enzyme purified using the pulse pumping system

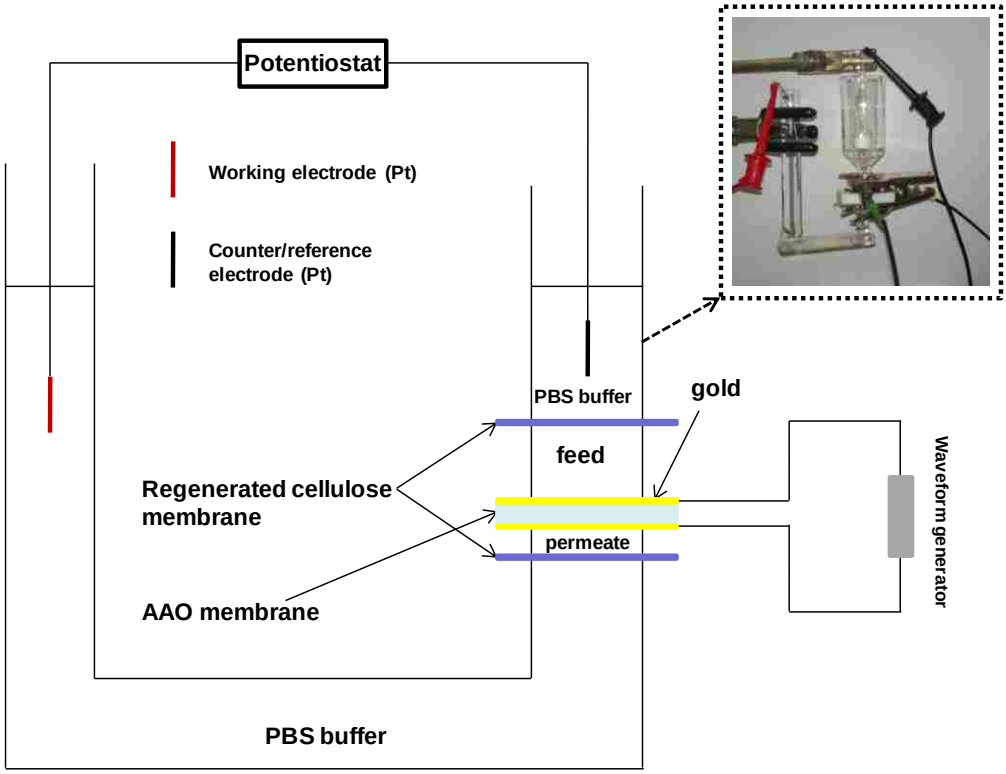

Figure 3.15 Schematic of Electrophoretic pumping cell

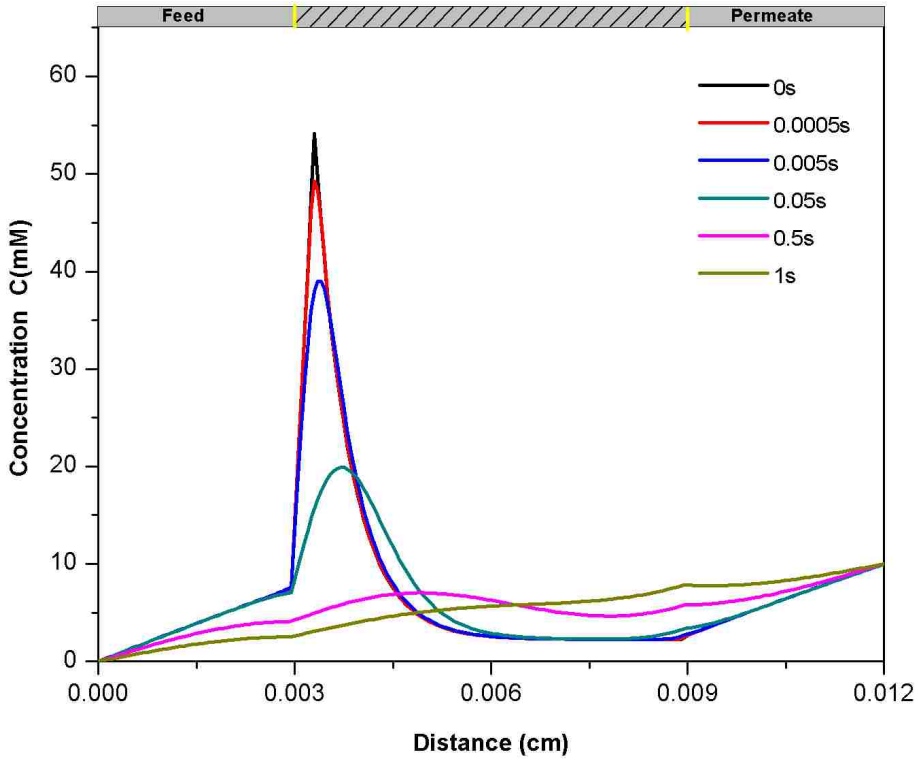

Figure 3.16 Imidazole repel during the protein binding cycle; the boundary condition here is constant 30 mM imidazole concentration at distance0.012cm. .

Chapter 4 : A functionalized anodic aluminum oxide membrane-electrode system for enzyme immobilization

This chapter is based on the manuscript submitted to ACS NANO: Zhiqiang Chen, Jianjun Zhang, Shanteri Singh, Pauline Peltier-Pain, Jon S. Thorson, Bruce. J. Hinds. 'A functionalized anodic aluminum oxide membrane-electrode system for enzyme immobilization', in minor revision

4.1. Introduction

Enzymes are biocatalysts capable of accelerating a range of chemical transformations relevant to materials production, pharmaceutical development and renewable energy and often present an attractive 'green' alternative to conventional synthetic strategies [108]. In their natural cellular/tissue environment, enzymes often assemble and/or co-localize to form multi-enzyme complexes or serial networks to expedite multi-step processes in part *via* minimization of substrate/product loss *via* diffusion [109, 110, 111, 112] and/or to maintain exquisite control of highly reactive intermediate species[113 , 114 , 115]. Additionally, the reliance upon sequential multi-enzyme processes and/or enzyme complexes enables metabolic control of an overall process via focused allosteric and/or competitive regulation of key gate-keeper enzymes within the process by substrate/product/cofactor concentrations [116]. Inspired, in part, by nature's logic, enzyme immobilization platforms offer the potential to mimic natural multi-enzymes systems [117, 118, 119, 120, 121], particularly in systems where convective flow can be used to efficiently direct products and intermediates in sequential manner rather than depending upon Fickian diffusion.

A variety of immobilization formats for multi-enzyme processes have been developed. For example, simple nitrilotriacetate immobilization of His_6-tagged enzymes, as exemplified by the 'superbead' approach reported by Wang and coworkers, offered improvements in enzyme stability and product isolation in the context of multi-enzyme sugar nucleotide synthesis and utilization processes[122,123]. However, such random immobilization strategies lack systematic control and rely on stochastic transport within the dense surface layer that is mechanistically analogous to homogenous solution. Kunitake and coworkers [124] constructed alternating layers of glucose oxidase and peroxidase with layer-by-layer film adsorption on a quartz slide and subsequently demonstrated sequential activity. Though discrete enzymatic reactions were spatially separated into layers in this example, the system lacked convective flow for directing the overall sequence of reactions. Bhattacharyya and coworkers recently developed reactive stacked membranes with a top membrane containing immobilized glucose oxidase and bottom membrane containing ferrihydrite/iron oxide nanoparticles for the degradation of toxic organic in water [125]. This membrane system has the advantage of using convective flow to direct the potentially damaging peroxide produced at the enzyme away to the Fe catalyst activation sites in the lower membrane layer. Building from these examples, an idealized structure is anticipated to derive from membrane pore bearing immobilized enzymes in a sequential order at nm-scale proximity. In this context, porous aluminum oxide (AAO) membranes offer an attractive platform due to its high pore density, uniform pore size and good resistance to non-specific protein adsorption [126, 127, 128]. The precise placement of gold electrodes on an AAO membrane would also make it possible for tunable immobilization of sequential enzyme cascades. Gold plating

has been successfully used to tune pore size and add surface chemistry on AAO membranes. Thus, multiple enzymes could feasibly be immobilized, in a sequential manner, on these two nm-scale electrodes to perform multi-step reactions at the membrane entrance and exit respectively to mimic natural multi-enzyme sequential processes.

As a simple model to demonstrate multi-step immobilized enzyme-catalyzed catalysis using AAO membranes, we have selected the recently reported glycosyltransferase-catalyzed transglycosylation process reported by Thorson and coworkers [106, 107]. This system is based upon the development of simple aromatic glycosides as efficient donors in glycosyltransferase (GTs)-catalyzed reactions for both sugar nucleotide formation (*i.e.*, the 'reverse' of a conventional GT-catalyzed reaction) and subsequent sugar nucleotide-mediated glycoside formation wherein the use of 2-chloro-4-nitrophenyl glycoside donors also offered a convenient colorimetric screen to enable the directed evolution of enhanced GTs with broad substrate permissivity [129]. Thus, this system offers a convenient model of a simple two-step enzyme catalyzed process - 2-chloro-4-nitrophenyl glycoside-driven sugar nucleotide formation and sugar nucleotide-mediated glycoside formation – for immobilization studies. Herein we report the successful immobilization of the His_6-tagged engineered glycosyltransferase OleD Loki variant on nm-scale electrodes at the pore entrance and exit of AAO membrane through Ni-NTA [130], which improves both enzyme activity and stability while eliminating unwanted hydrolytic side reactions known to occur at higher enzyme concentrations in the solution phase. In addition, discrete control of each independent step of the two-step sequential reaction was demonstrated via selective reagent feedstock composition exposure of the

top and/or bottom surface of immobilized membrane/electrode system. Finally, a convenient one-step immobilization and purification of *N*-His_6-OleD Loki variant directly from crude *E. coli* extracts expression broth was demonstrated to enable rapid immobilized catalyzed regeneration. Cumulatively, this study highlights the utility of the AAO membrane/electrode system as a support architecture for controlling multi-step enzymatic processes.

4.2. Experimental details

4.2.1 Materials

AAO membranes were purchased from Whatman. Gold (I) thiosulfate was purchased from Alfa Aesar (Ward Hill, MA) and ascorbic acid was purchased from EM Science (Gibbstown, NJ). Vancomycin aglyconand 2-chloro-4-nitrophenyl glucoside were prepared as previously reported [107, 131]. All other chemicals were purchased from Sigma Aldrich (Milwaukee, WI) and all chemicals were used as received unless otherwise noted. Swinnex 47mm filter holders was purchased from Millipore (Billerica, MA).

4.2.2 Membrane/electrode fabrication

Sputtering was performed with a Cressington Coating System (Ted-Pella) with calibrated quartz crystal monitor with background pressure of 0.02 mbar. No intermediate wetting layer (*i.e.*, Ti/TiO_2) on Al_2O_3 was needed for seeding the Au layer. Gold (5 nm) was sputtered on the both top and bottom of AAO membranes followed by electro-less plating. Electro-less plating was performed in 50 mM phosphate buffer, pH 7.0,

containing 1.6 mM sodium gold (I) thiosulfate and 2.68 mM ascorbic acid . The oxidization and reduction reactions were given by

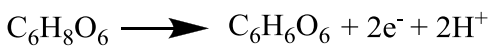

Pore size before and after electro-less plating was analyzed via scanning electron microscopy (SEM) using a Hitachi S-4300 scanning electron microscope.

4.2.3 Enzyme immobilization and Regeneration

N-[Nα,Nα-Bis(carboxymethyl)-L-lysine]-12-mercaptododecanamide (NTA) self-assembled monolayer was prepared by incubation of gold with 10 mL 1 mM NTA ethanol solution at 25 ^{o}C for 24h followed by rinsing with 10 mL ethanol for 3 min and drying under N_2 stream. The membrane was incubated with 10 mL 0.5M $NiCl_2$ aqueous solution for 24 h at 25 ^{o}C followed by rinsing with 10 mL Milli-Q water for 3 min and dried under N_2 stream. The production and purification of OleD Loki [129] and GtfE [132] followed previously reported methods. One side or both sides of the membranes were incubated with an excess of purified enzyme in 10 mL 50 mM Tris-HCl buffer, pH 8.5, for 24 h at 4 ^{O}C and washed with an equal volume of buffer for three times to remove unbound protein prior to use**..**Immobilized protein was released by 500 mM imidazole (10 mL, 50 mM Tris-HCl buffer, pH 8.5) followed by filtering to remove imidazole. The amount of released protein was determined via standard Bradford assay. The OleD Loki-loaded membrane can be regenerated by simply soaking in 0.5 M EDTA (10 mL, 50 mM Tris-HCl buffer, pH 8.5), followed by $NiCl_2$ reattached as described before.

4.2.4 Protein capture from *E. coli* lysates

Following standard protocol [129], cell pellets from standard heterologous overproduction of OleD Loki in *E. coli* were collected by centrifugation (6,000 x*g* at 4 ℃ for 20 min), resuspended in 2.5 mL of chilled lysis buffer (20 mM phosphate buffer, pH 7.4, 0.5 M NaCl, 10 mM imidazole), and lysed by sonication (5 pulses of 1 minute each) in an ice bath. Cell debris was removed by centrifugation (10,000 g at 4 ℃ for 20 min) and NTA-Ni modified membranes were then incubated in the resulting crude extracts (10 mL) for 24 h at 4 ^{O}C and the membranes subsequently washed with 5 mL50 mM Tris-HCl buffer, pH 8.5 for three times to remove unbound protein.

4.2.5 HPLC method

HPLC was conducted with an Agilent 1260 system equipped with a DAD detector with a 250 mm x 4.6 mm Gemini-NX 5µ C18 column (Phenomenex, Torrance, CA, USA) and using a linear gradient of 1% B to 71% B over 30 min, 71% B for 5 min, 71% B to 1% B over 1 min, 1% B for 4 min (Solvent A = 50 mM PO_4^{2-}, 5 mM tetrabutylammonium bisulfate, 2% acetonitrile [pH adjusted to 6.0 with KOH]; Solvent B = acetonitrile; flow rate = 1 mL min^{-1}; A254 nm;). Regardless of method, HPLC peak areas were integrated with an Agilent (Santa Clara, CA) 1260 workstation and the percent conversion calculated based upon peak area of the products and unreacted starting materials.

4.3 Results and Discussion

The primary membrane design challenge is to localize enzyme functionality at pore entrances and exits to enable directional flow of substrates/products over the enzyme active sites in an efficient manner. Commercially available 20 nm nominal diameter AAO membranes are asymmetric with a thin porous layer at the top with a diameter of 27 nm and a bulk pore structure mainly comprised of 200 nm diameter straight channel monoliths. The depth that gold sputtering can reach within the top pore neck is around 20 nm and gold electro-less plating occurs only on that deposited gold seed layer. The pore diameter of AAO membranes can be controlled by changing electro-less plating time as shown in Figure 4.1. Fifty minutes of electro-less plating time gave the desired average pore diameter of 10 nm match the GT of dimer length of 9.2 nm [133]. With this geometry GT_1 (the first GT as shown in Figure 4.3) , on the 10 nm pore entrance will block the pore, thus excess solution GT_1 can't pass through the pore to the other side of AAO membrane after binding. This allows a second distinct enzyme, GT_2, to be immobilized on the 200 nm pore side of AAO membrane to enable a directional sequential series of reactions. The process for *N*-His_6-OleD immobilization on a gold surface (Figure 4.2) enabled immobilization of a total amount of 30 g of enzyme per monolayer coating based upon Bradford assay to afford a surface 'concentration' of 3 g/mL immobilized enzyme within the 9.8×10^{-6} mL electrode volume .

To demonstrate the immobilized activity of the enzyme on the membrane system we first compared GT-catalyzed UDP-Glc production (Figure 4.3, Reaction 1) in a standard solution-phase reaction to that of the membrane-supported format. The solution-phase reaction contained 2.6 mM glycoside donor, 1 mM UDP, 100 μg/mL OleD Loki in a total

volume of 200 μL l Tris-HCl (50 mM, pH 8.5) and was incubated at 25 ℃ for 12 h. The much higher than standard (typically 0.5-2.0 g/mL) enzyme concentrations employed in this solution-phase comparator reaction were utilized to better reflect the high local concentration of immobilized system (estimated as 3g/ml as previously described). The corresponding immobilized reaction utilized an identical reagent/reaction mixture (lacking enzyme) pumped through the OleD Loki loaded membrane at 1 mL/h over 4 h at 25 ℃. UDP-Glc production in the solution-phase reaction and the collected eluent from the solid-phase reaction was determined by HPLC (Supplementary Methods). As controls, identical reactions wherein OleD Loki was replaced by *N*-His_6-tagged CalC (an enediyne self-resistance protein devoid of GT activity) [134, 135] were utilized to distinguish any potential non-enzymatic contributions to UDP-Glc production.

Figure 4.4 highlights the outcome of this initial reaction 1 comparison and reveals a total 40% yield of UDP-Glc in the membrane-bound enzyme format compared to 12% in the solution phase and no reaction in the comparator CalC-based negative controls. Interestingly, significant amounts of PNP-Glc were still present in the membrane-bound eluent suggesting the 1 mL/h flow rate to be too fast for optimal residence time. In contrast, PNP-Glc was exhausted in the solution-phase reaction and corresponding low UDP-Glc yield was attributed to undesired PNP-Glc and UDP-Glc hydrolysis that unexpectedly occurred at high enzyme concentrations and extended reactions times (Figures 4.11 and 4.12). While a reduction of enzyme concentration and shorter reaction times in the solution phase format can circumvent this unwanted effect, the immobilized format offers the opportunity to fine-tune residence time via adjusting the flow rate to afford optimal UDP-Glc production in reaction 1 at high concentrations without allowing

the subsequent hydrolysis reaction. Within this context, the substrate residence time can be calculated based upon [(pore area x electrode thickness)/volume flow rate]. Thus we expect to achieve the best reaction yields via matching an optimal flow rate with an enzyme's specific kinetics where slower enzymes might require an additional increase in path length.

For the current model system, the kinetics of the solid-phase system can be estimated based upon enzyme loading per surface area (*i.e.*, concentration) and flow rates. Specifically, the loading of OleD Loki on the nm-scale electrode was 30 g, giving a local concentration of about 3 g/mL based on the pore volume of the solution adjacent to the 20-nm thick gold electrode. Using the average turnover number of OleD Loki (10 min^{-1})[129], the theoretical calculated UDP-Glc yield vs. flow rate (Figure 4.5) predicts 0.4 mL/h as the optimal flow rate for continuous UDP-Glc production. Consistent with this model, Figure 4.5 illustrates the impact of flow rate upon UDP-Glc formation with a maximum yield observed experimentally at a flow rate of 0.5 mL/h. This is also consistent with a model wherein unwanted hydrolysis, which occurs under very high enzyme concentrations in the solution-phase over extended periods, does not significantly impact upon product formation under optimal solid-phase conditions. Specifically, nearly quantitative UDP glycosylation (98%, square dot shown in Figure 4.5) was observed experimentally at a flow rate 0.5 mL/h, illustrating the potential of the immobilized system to reduce unwanted side reactions and thereby optimize product output.

Continuous production is another important merit of an immobilized platform. UDP glycosylation reaction was continuously carried out at pumping rate 0.4ml/h with 2.56Mm PNP-Glu and 1Mm UDP using the immobilized enzyme system as shown in

Figure 4.6. Low UDP glycosylation yield is observed Day 1 due to dead-volume at the filter holder. The glycosylation yield reaches highest point at Day 3 and then decreases a little bit. The enzyme reserves very strong activity (almost no decrease) even after 5 day, which is good for long-term enzyme uses and scale-up. Based on 0.4mL/h continuously pumping for 120 h and average 95.72% glycosylation yield, the total production of UDP-Glc over the 30 μg Loki immobilized enzyme system is 4.6×10-5 mol UDP-Glc. This is compared to 0.2 mL of the homogeneous solution protocol with 20 μg of Loki for a total of 2.4x10-8 mol. The membrane flow reactor gave a 1917 fold improvement in enzyme utilization based on 120 h reaction. In fact, the membrane is still very active (as shown in figure 1) and can process much more reagents.

Two-step sequential reactions on the membrane immobilized enzymes system were then carried out to mimic multi-enzyme processes, and compare their performance to solution-based single-glycosyltransferase coupled reactions. We selected two model GTs (GtfE and OleD Loki) that catalyze glucosyltransfer from UDP-Glc to model acceptors (vancomycin aglycon and 4-methylumbelliferone, respectively) with differing proficiencies. Specifically, the turnover rates for GtfE [132] and Loki [129] are 0.005 and 10 min^{-1}. For the sequential reaction platform, the reaction sequence was physically separated into two discrete steps with the first (UDP-Glc formation – reaction 1) occurring on the top face of the membrane (entry) and the second (aglycon glucosylation – reaction 2) on the bottom face (exit) To afford this physical separation of reactions, the required reagents for reaction 2 were introduced by cross-flow to the bottom surface as illustrated in Figure 4.7. This format allows for sequential transfer of intermediates by having separate reagents flowing through the top and supplied orthogonally to the bottom

of the membrane. Thus, for the kinetically matched pairing where both GT_1 and GT_2 (Figure 4.3) are OleD Loki, the UDP-Glc formed in reaction 1 enters the reaction 2 sequence via directional flow wherein the acceptor 4-methylumbelliferone (4Me-UMB) is only present in the lower reaction vessel at the membrane exit.

For this analysis, solution-phase and membrane-supported reactions were conducted in parallel using similar conditions to offer a potential comparison of overall utility to afford the desired glycosylated product. For the kinetically matched pairing where both GT_1 and GT_2 (Figure 4.3) were OleD Loki, the solution-phase reaction contained 2.56 mM PNP-Glc, 1 mM UDP, 0.56 mM 4Me-UMB and 100 μg/mL OleD Loki variant in a total volume of 200 μl 50 mM Tris-HCl (pH 8.5) incubated for 12 h at 25 ℃. The corresponding immobilized system employed the same reagents/concentrations where PNP-Glc and UDP were introduced from the top of the membrane using a syringe pump (reaction 1) while 4Me-UMB was separately fed across the bottom of the membrane in orthogonal cross-flow using a second syringe pump (Figure 4.10), both at a flow rate of 0.5 mL/h. Product formation in the solution-phase reaction and the eluent from the bottom solid-phase reactor face were analyzed by HPLC.

Figure 4.8 highlights the distribution of reactants/products in the lower eluent of the solid-phase OleD Loki-based sequential reaction series revealing a yield of the desired product (4Me-UMB glucoside) 71%. The corresponding solution-phase yield of 4Me-UMB was 16% (Figure 4.13) wherein potential GT-catalyzed reaction reversibility and UDP-Glc hydrolysis under longer reaction times are likely major contributors to the reduction of the overall yield. While this supports our initial premise that the membrane immobilized format serves as a potential platform for mimicking Nature's control of

multi-enzyme sequential reactions, one limitation derives from a need to pair the corresponding enzyme catalytic efficiencies with flow rates. Consistent with this, while a solution-phase sequential OleD/GtfE-catalyzed reaction was previously demonstrated[132], the kinetically mismatched (10 min^{-1} vs 0.005 min^{-1}) OleD Loki (top)/GtfE (bottom) pair failed to afford the final desired product due to an inability to reduce the flow rate to sufficiently compensate for the slow turnover rate of GtfE without succumbing to back diffusion and unwanted OleD Loki-catalyzed hydrolysis of UDP-Glc (Figure 4.18). In such cases, a possible solution may be to increase the active path length (membrane/electrode thickness) to increase residence time or increase enzyme loading of the slower enzyme.

The design of the membrane platform presented suggests that, like a standard nickel nitrilotriacetic acid resin-based column, this membrane should be able to 'capture' active enzyme directly from crude lysates thereby circumventing the need for protein purification as part of membrane preparation (Figure 4.14). To assess this, membrane was exposed to 5 mL of crude lysate from a standard OleD Loki *E. coli* heterologous overexpression culture for 24h, subsequently washed with Tris-HCl buffer for three times and the purity of the captured protein upon release via treatment with 500 mM imidazole in Tris-HCl buffer solution was determined via SDS-PAGE, which revealed captured protein with a purity of ≥99% (Figure 4.15). Importantly, the membrane loaded via the crude extract capture method catalyzed nearly quantitative single step UDP-glycosylation (98 %) and a corresponding notable two-step 4Me-UMB glycosylation yield (80 %) at optimal volume flow rates (Figure 4.16 and Figure 4.17).

Finally, the membrane-immobilized enzyme also displayed notable stability even after two months of cold storage at 4℃. Specifically, the immobilized enzyme $T_{1/2}$ based upon UDP-Glc formation was more than 55 days (Figure 4.9). In addition, the membrane platform is robust and could be reused multiple times via a simple regeneration process (removal of protein with 500 mM imidazole, rinsing with Tris-HCl buffer and subsequent protein reloading).

4.4. Conclusion

In conclusion, we have demonstrated a design for a robust sequential enzyme reaction system immobilized on nano-scale electrodes at the entrance and exit of AAO membranes. The local enzyme concentration at the nano-scale electrodes is much higher compared to homogenous solution and allows precise control of the enzyme residence time of substrates, translating to improvements in overall output via the reduction of unwanted side reactions (hydrolysis) and/or potential product inhibitors. Model sequential reactions using the same format revealed similar advantages wherein a main limitation stems from the need to pair enzymes of similar catalytic efficiencies with overall flow rate. In situations where catalytic efficiencies of catalysts dramatically differ, it is expected that extending the path length (i.e., surface area) for slower catalysts could enable pairing with faster catalytic partners. Additional advantages observed in this study include the ability to rapidly capture target catalysts from crude *E. coli* lysates and the relatively long-term stability of target catalysts and corresponding membrane architecture. As such, this membrane platform offers an opportunity to expand the study and biocatalytic utility of multi-enzyme cascades with directed mass transport.

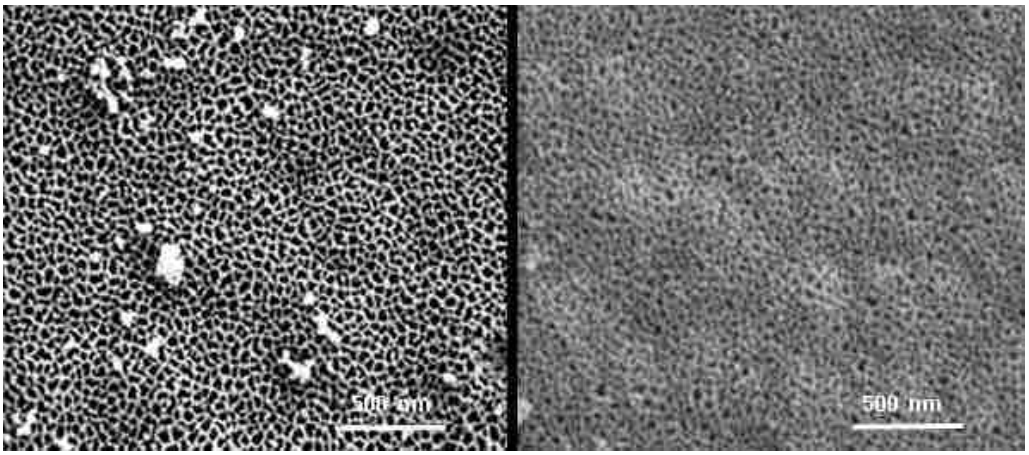

Figure 4.1SEM images of bare AAO membrane and electro-less plated AAO membrane on top surface sputtered seed layer.

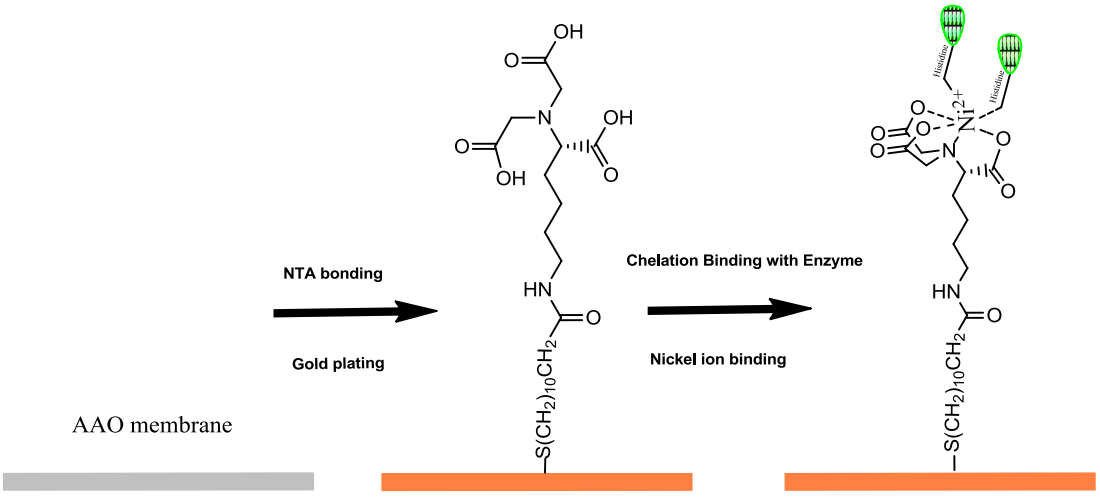

Figure 4.2 Enzyme immobilization process onto Au electrodes at AAO pore entrances. In the presence of excess *N*-His_6-enzyme for 24 h (see experimental section), the 20 nm pore size surface is routinely coated with 30 μg g of enzyme, affording a local surface concentration of 3g/mL.

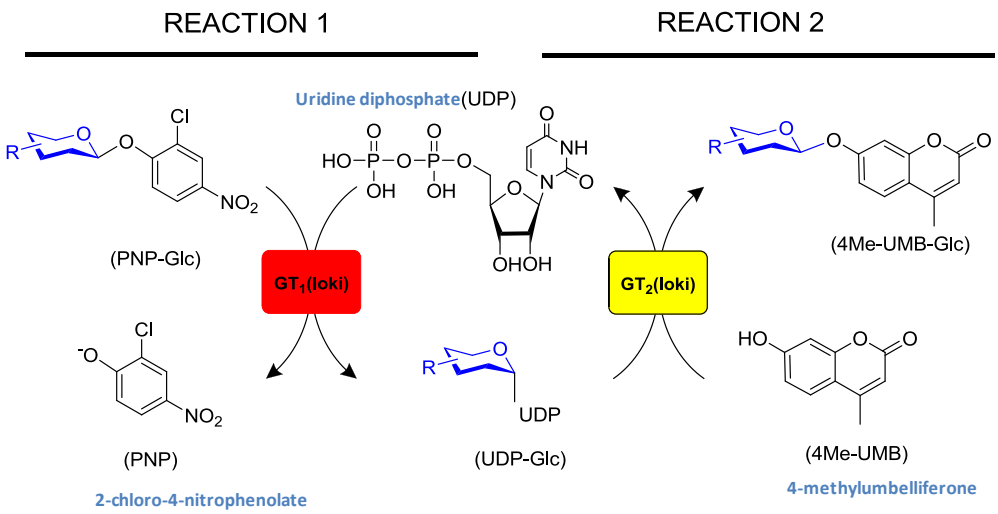

Figure 4.3 Model reactions utilized to assess the immobilized platform. Reaction 1 is a 2-chloro-4-nitrophenyl glucoside (PNP-Glc) driven glycosyltransferase-catalyzed 'reverse' reaction to produce the desired sugar nucleotide UDP-Glc. Reaction 2 is a standard glycosyltransferase-catalyzed glycosylation of the model acceptor 4Me-Umb where the UDP-Glc from reaction 1 serves as the sugar donor in a sequential reaction. For the current study, reaction 1 occurs on the top face while reaction 2 occurs at the bottom face of the reactor membrane, respectively.

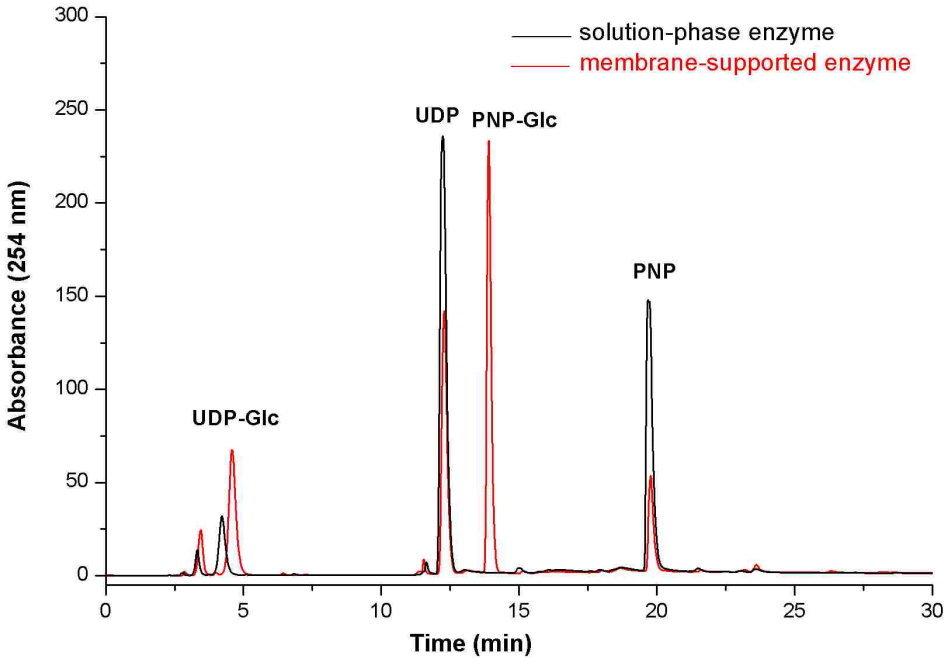

Figure 4.4 Representative HPLC analysis of UDP-Glc production (reaction 1) using solution-phase enzyme and membrane-supported enzyme. The solution-phase reaction contained 2.6 mM glycoside donor, 1 mM UDP, 100 μg/mL OleD Loki in a total volume of 200 μL l50 mM Tris-HCl, pH 8.5 and were incubated at 25 ℃ for 12 h. The immobilized reaction contained 4mL of the same reagent mix (lacking solution-phase OleD Loki) injected through the membrane containing a total of 30 μg immobilized OleD Loki at a flow rate of 1 mL/h at 25 ℃ for 4h. Resulting reactions were subsequently analyzed by HPLC

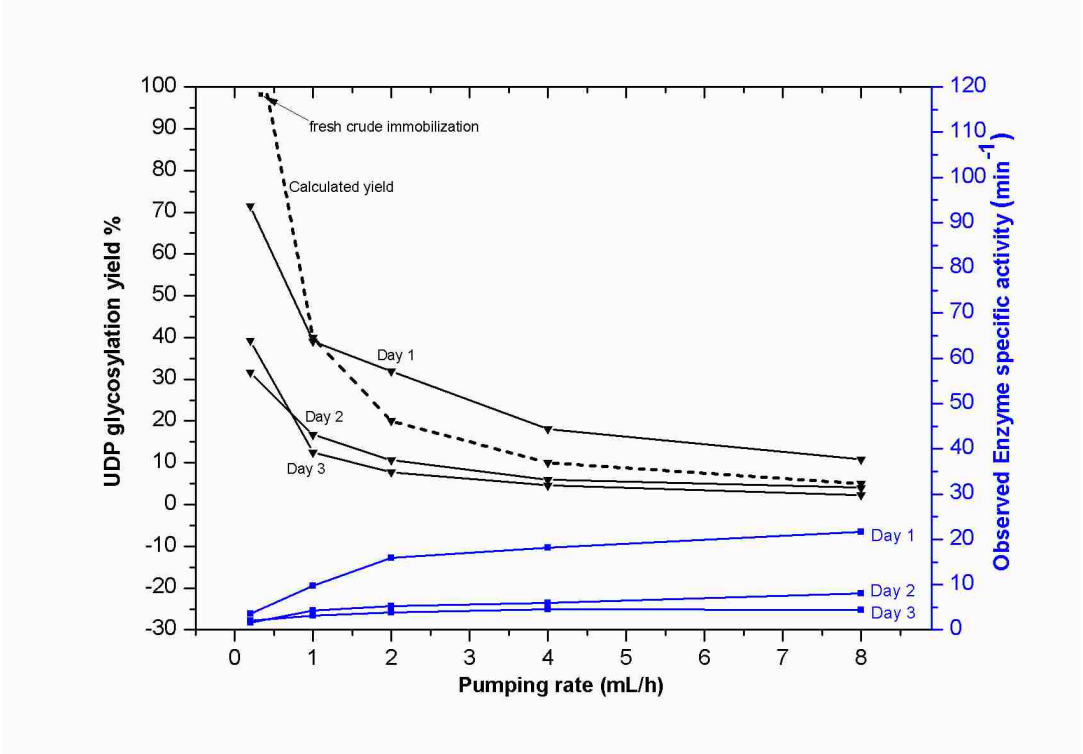

Figure 4.5 Calculated (dotted line) and observed UDP-Glc production as a function of flow rate; for pumping rate 0.2 mL/h, 1 ml/h and 2 mL/h, the pumping time was 4h and for pumping rate 4 mL/h and 8 mL/h, the pumping time was 1h. Day 1 refers to a complete series of runs at specified pumping rates, followed by repeating a 2nd complete series on Day 2, to show enzyme stability.

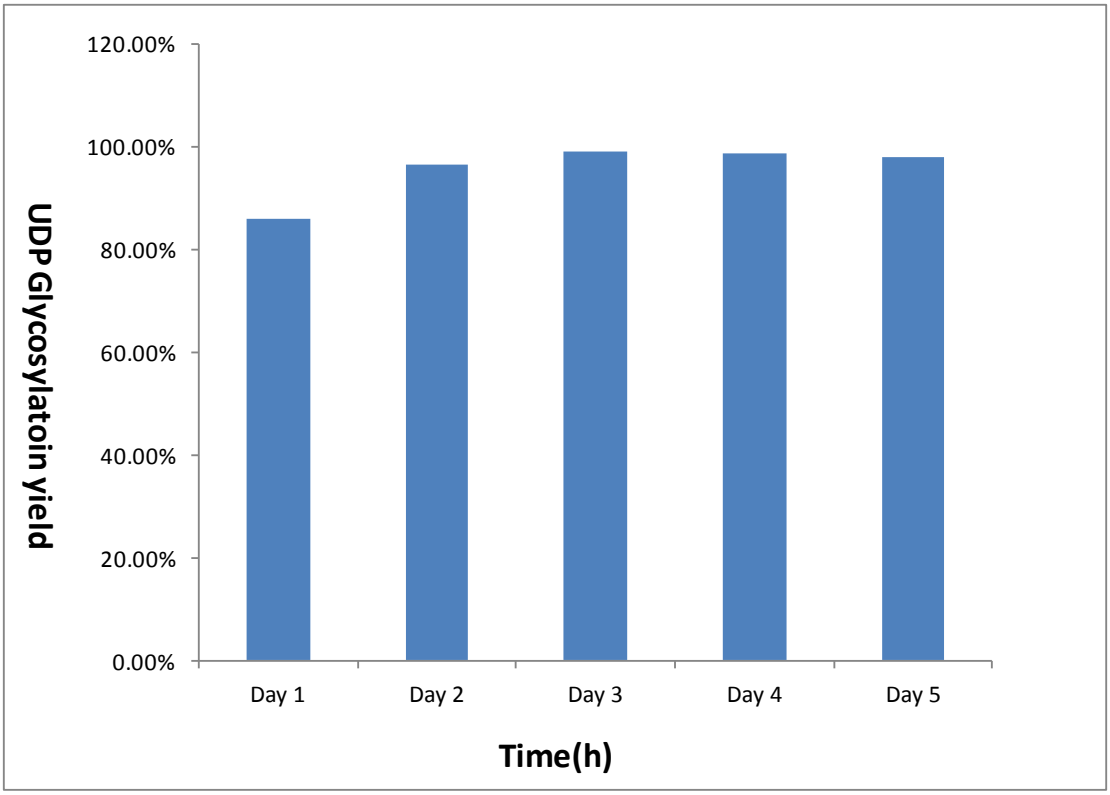

Figure 4.6 Continuous UDP Glycosylation yield through membrane carrying immobilized OleD Loki (from crude extract capture method).The UDP glycosylation reaction was continuously carried out at pumping rate 0.4mL/h with 2.56 mM PNP-Glu and 1Mm UDP using the immobilized enzyme system.

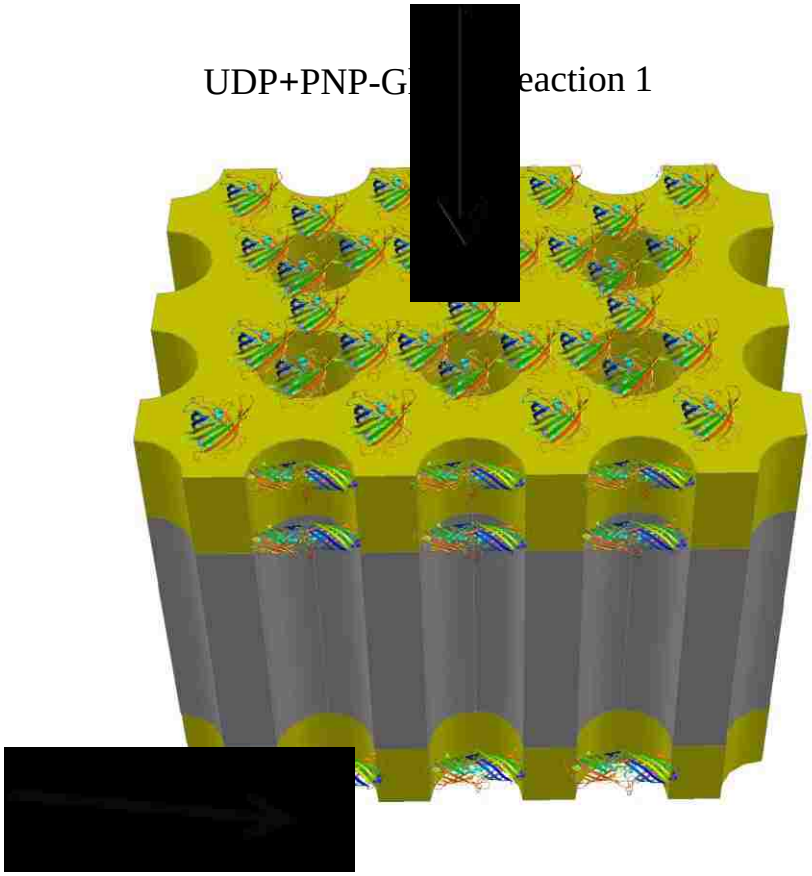

Figure 4.7 The configuration for the solid-phase two-step sequential reaction process (Figure 3 reaction 1, top face; reaction 2, bottom face) catalyzed by AAO membrane-immobilized OleD Loki.

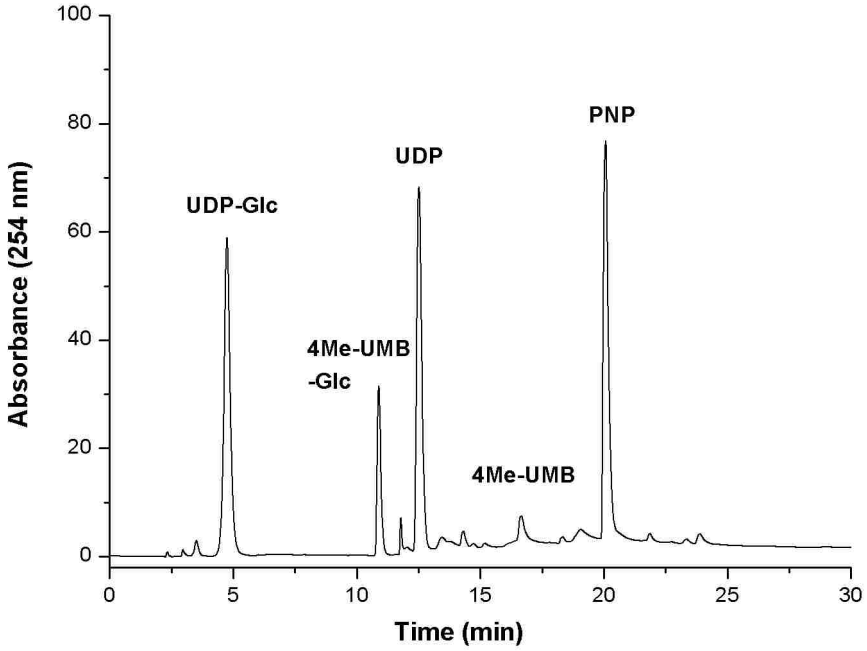

Figure 4.8 HPLC analysis of a representative immobilized sequential reaction containing 2.56 mM PNP-Glc and 1 mM UDP in 50 mM Tris-HCl, pH 8.5 in the upper reactant chamber injected through the membrane carrying immobilized OleD Loki on the top and bottom face into a bottom reaction chamber containing 0.56 mM 4Me-UMB in same buffer. Flow rate for this sequential reaction was 0.5mL/h at 25 ℃ for 4h and the bottom reaction chamber contents were subsequently analyzed by HPLC.

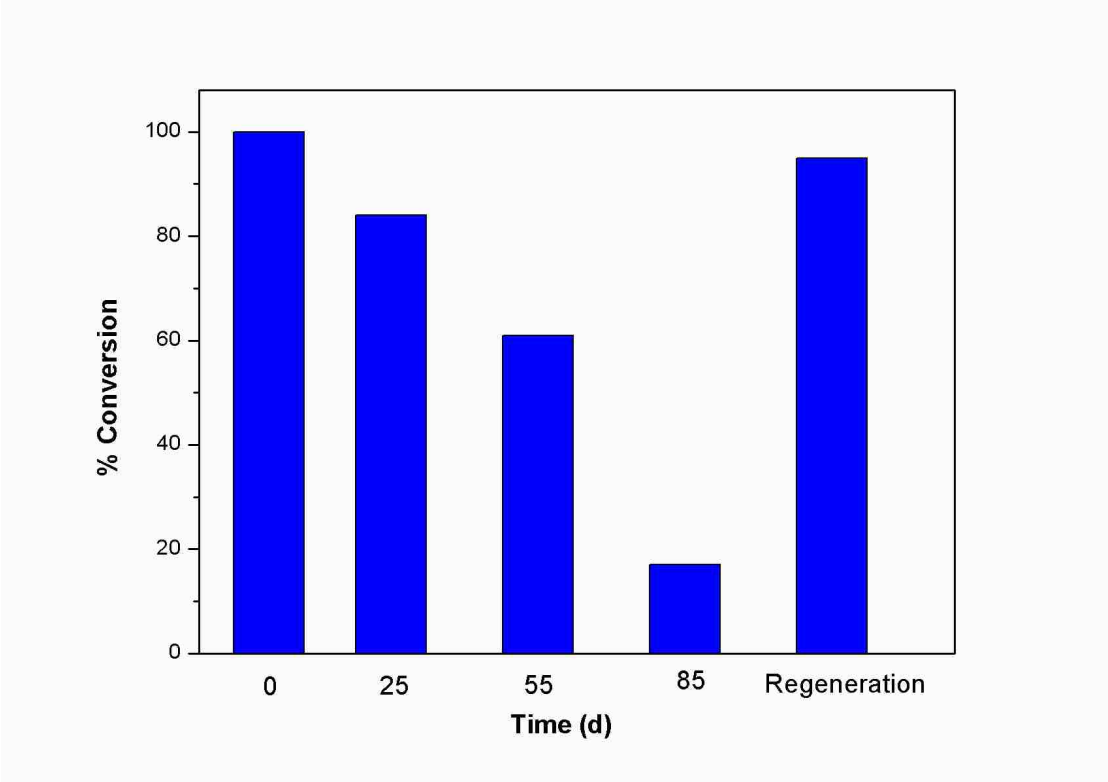

Figure 4.9 Stability of immobilized enzyme stored at 4 ℃ where percent conversion is based upon UDP-Glc formation (reaction 1) as determined via HPLC.

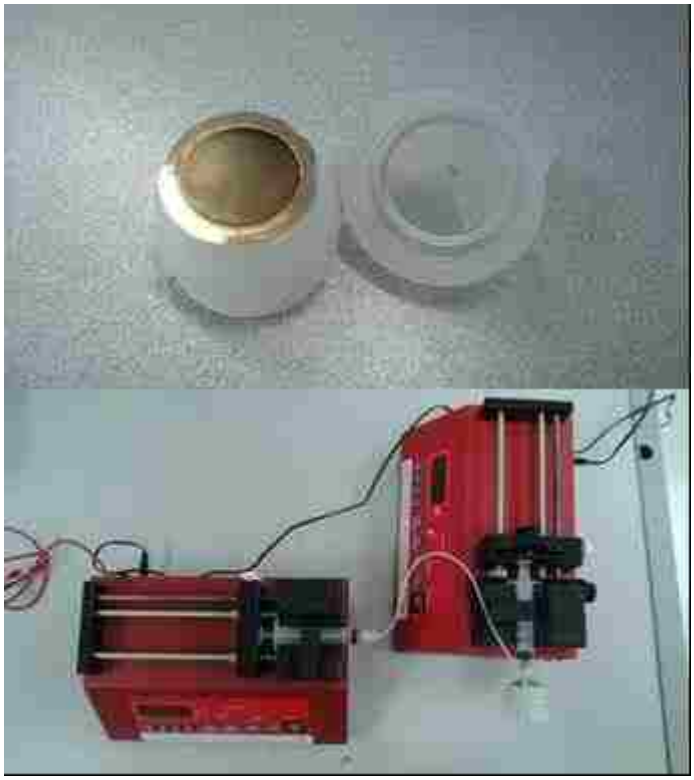

Figure 4.10 Set-up for membrane-based sequential reactions; PNP-Glc and UDP were introduced from the top of the membrane using pump1 (reaction 1) and 4Me-UMB was separately fed across the bottom of the membrane in orthogonal cross-flow using pump 2, both at a flow rate of 0.5 mL/h.

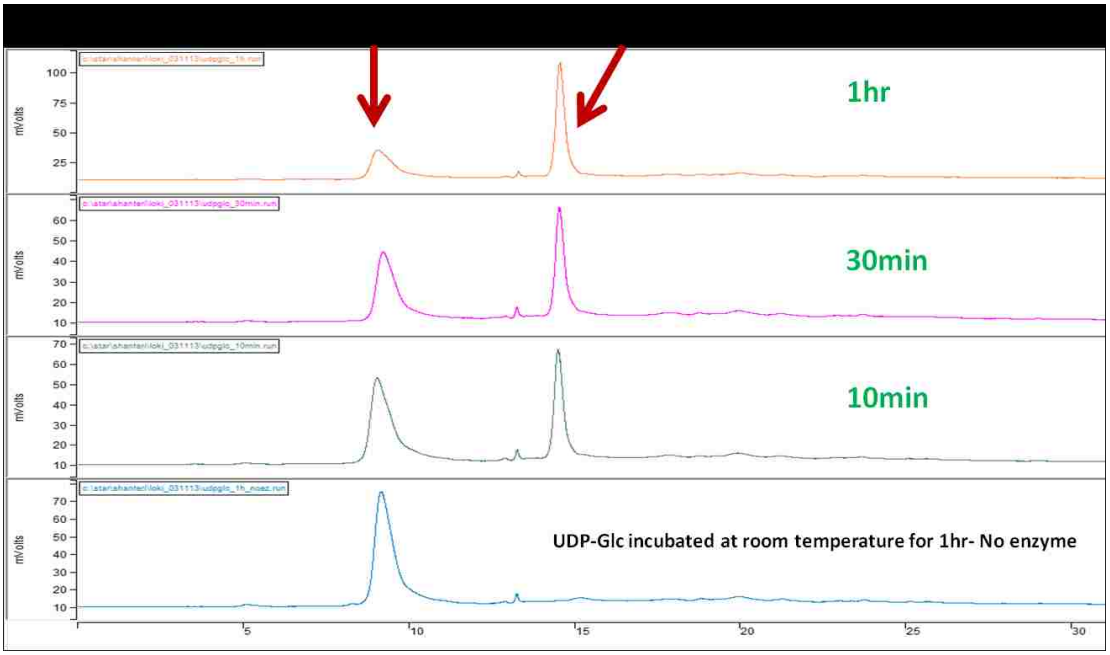

Figure 4.11 Representative hydrolysis of UDP-Glc (reaction 1 product) by OleD Loki at higher concentrations of catalyst in a solution-phase reaction (reaction conditions: 0.5 mM UDP-Glc, 100 µg /mL Loki, 100 µL Tris-HCl, pH 8.0, 25 ^{o}C; at the time points indicated, 30 µL aliquots were quenched with an equal volume of MeOH and analyzed *via* HPLC).

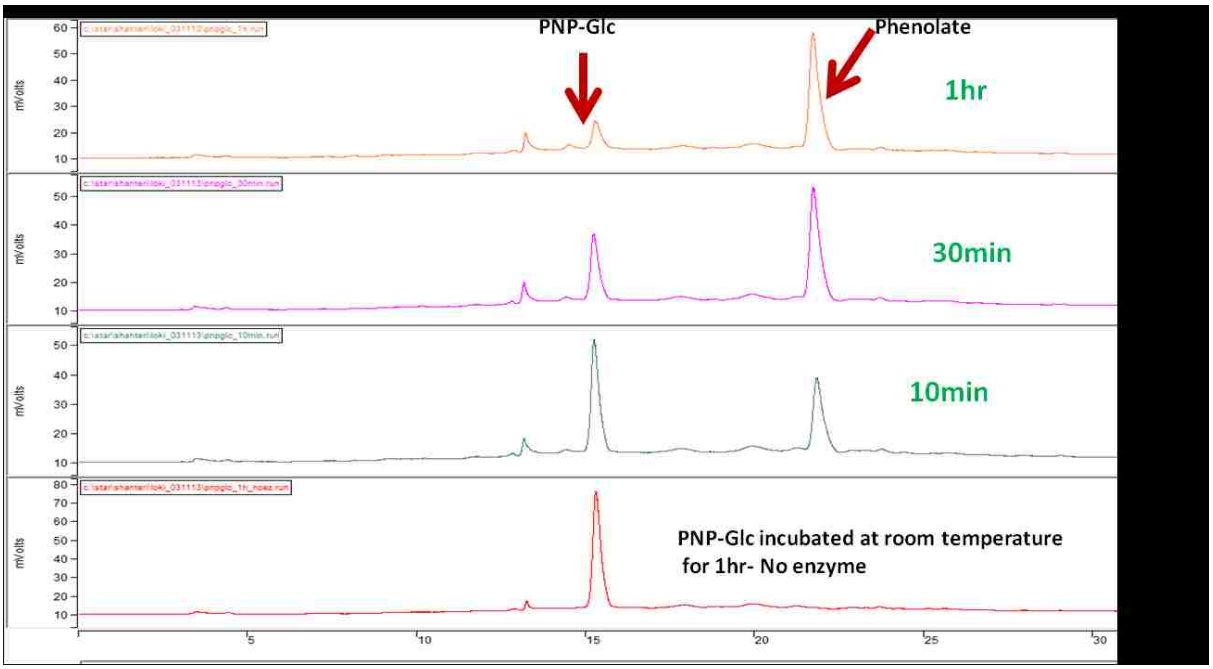

Figure 4.12 Representative hydrolysis of PNP-Glc (reaction 1 substrate) by OleD Loki at higher concentrations of catalyst in a solution-phase reaction (reaction conditions: 0.5 mM UDP-Glc, 100 μg /mL Loki, 100 μL Tris-HCl, pH 8.0, 25 ^{o}C; at the time points indicated, 30 μL aliquots were quenched with an equal volume of MeOH and analyzed *via* HPLC).

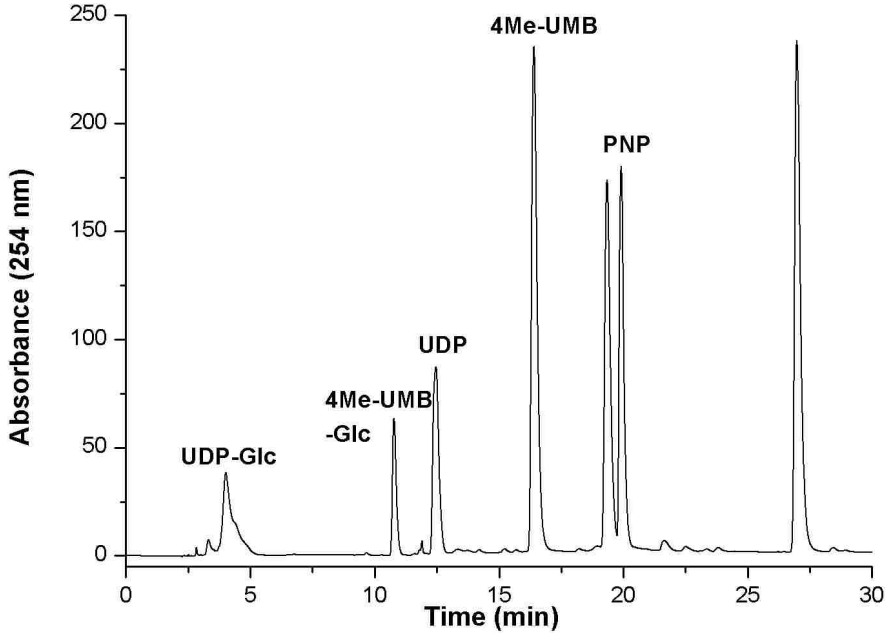

Figure 4.13 HPLC analysis of a representative solution-phase sequential reaction containing 2.56 mM PNP-Glc, 100 ug/mL OleD Loki, 1 mM UDP, 0.56 mM 4Me-UMB, in 200 µl 50 mM Tris-HCl, pH 8.5 incubated at 25 ℃ for 12h.

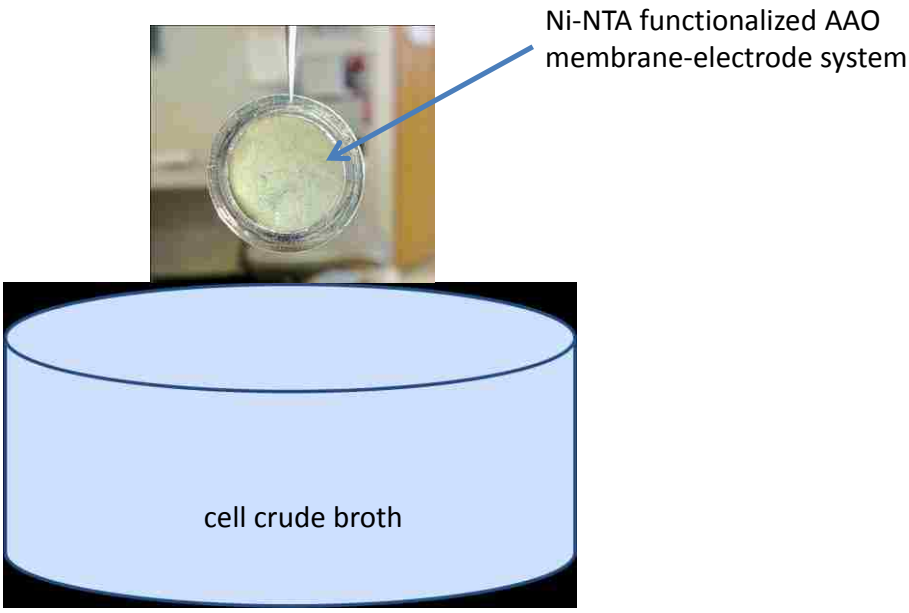

Figure 4.14 Illustration of the one-step capture from an OleD Loki *E. coli* overproduction crude cell extract (see experimental section for details).

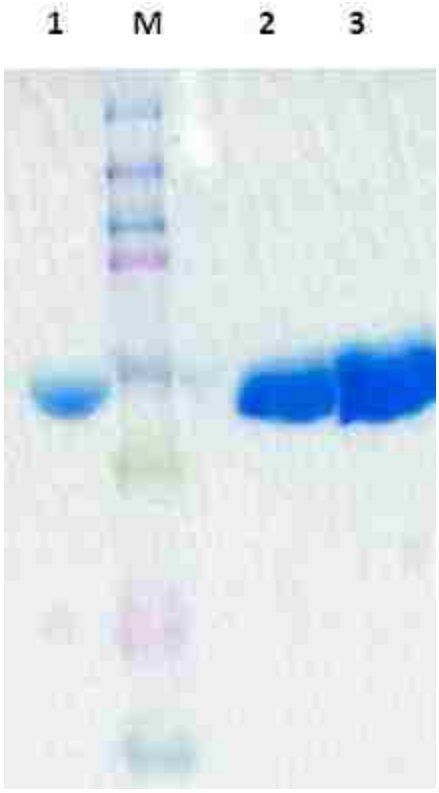

Figure 4.15 Representative SDS-PAGE of OleD Loki released from AAO membrane after one-step capture process. Lanes: 1) pure OleD Loki; M) standard molecular weight markers; 2) 7 μg captured OleD Loki released from AAO membrane; and 3) 14 μg captured OleD Loki released from AAO membrane. Lanes 2 and 3 were purposefully overloaded to delineate potential impurities associated with the capture method.

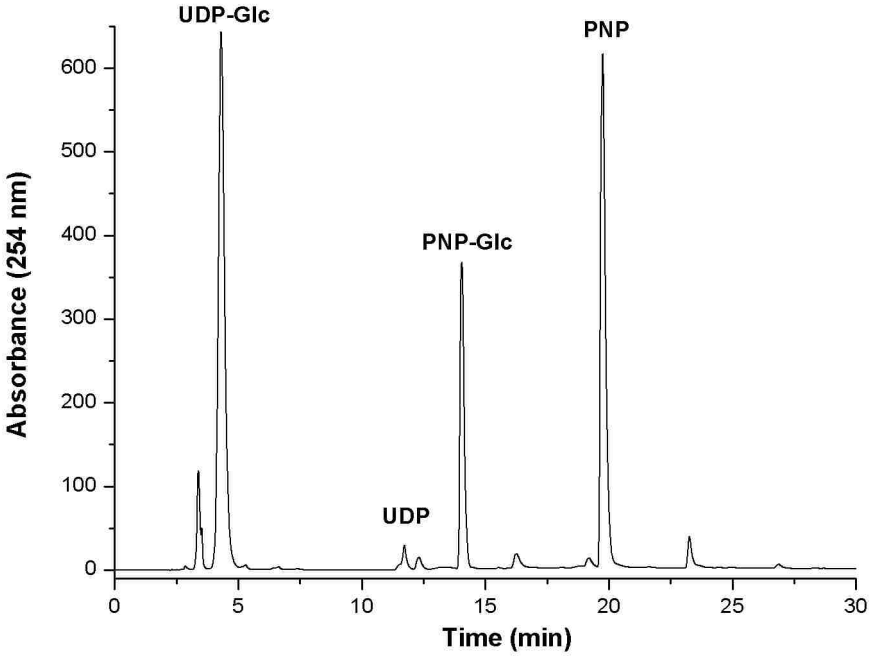

Figure 4.16 Representative HPLC analysis of UDP-Glc production (reaction 1) using membrane-supported enzyme prepared via the crude extract capture method. The solution-phase reaction and were incubated at 25 ℃ for 12 h. The immobilized reaction contained 2.6 mM glycoside donor and 1 mM UDP in a total volume of 2 mL 50 mM Tris-HCl, pH 8.5 injected through the membrane containing a total of 30 μg captured OleD Loki at a flow rate of 0.5 mL/h at 25 ℃ for 4h. Resulting reactions were subsequently analyzed by HPLC. For comparisons, Figure 4 highlights a representative immobilized reaction loaded with previously purified OleD Loki and a representative solution-phase comparator reaction.

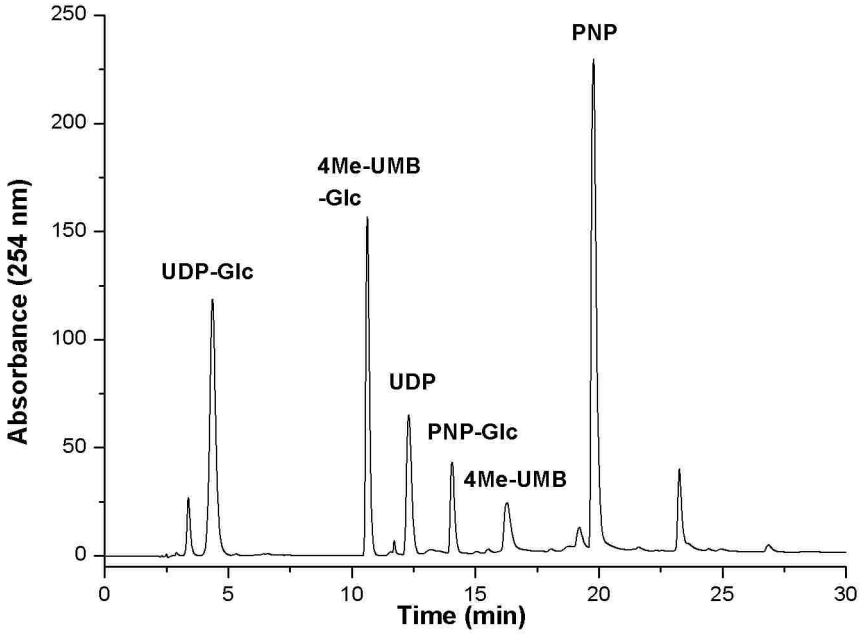

Figure 4.17 HPLC analysis of a representative immobilized sequential reaction containing 2.56 mM PNP-Glc and 1 mM UDP in 50 mM Tris-HCl, pH 8.5 in the upper reactant chamber injected through the membrane carrying immobilized OleD Loki (from crude extract capture method) on the top and bottom face into a bottom reaction chamber containing 0.56 mM 4Me-UMB in same buffer. Flow rate for this sequential reaction was 0.5mL/h at 25 ℃ for 4h and the bottom reaction chamber contents were subsequently analyzed by HPLC.

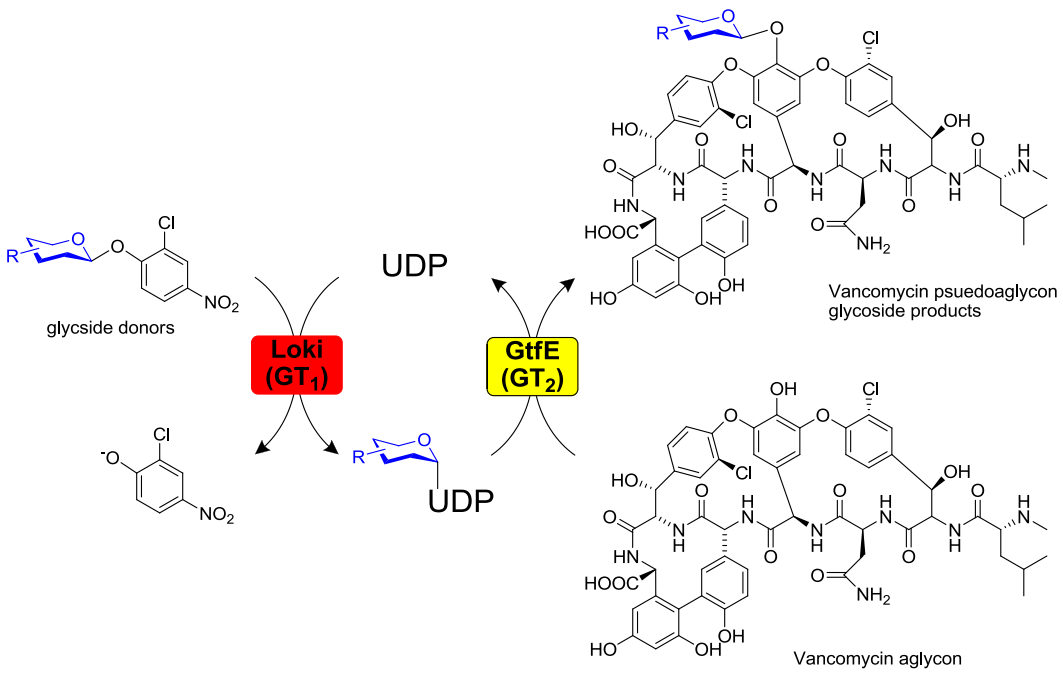

Figure 4.18 Scheme for an OleD Loki/GtfE sequential coupled reaction for glucosylation of the vancomycin aglycon. (Reprinted from Ref [132])

Chapter 5 : Flow-through Electroporation of HL-60 White Blood Cell Suspensions using Nanoporous Membrane Electrodes

5.1 Introduction

The genetic modification of free-flowing white blood cells is highly attractive for therapy. The white blood cells are complex organisms that are able to destroy targeted cells through the expression of specific anti-body receptors on its cell wall. Another approach to utilizing white blood cells is to have these genetically modified cells continually express needed biomolecules to be distributed through the cardiovascular system. In a recent ground-breaking study, white blood t-cells were genetically modified with exogenous DNA (lentivirus vector) and 'programmed' to destroy cancer cells. This method was shown to be an effective treatment for a patient with leukemia [136]. However due to the use of viral vector, immune response and hypogammaglobulinemia were detected. Moreover, it is a delicate balance to modify a t-cell to attack cancer cells and not healthy cells, thus there is a significant inherent risk to permanently modifying all t-cells in a large patient population through a virus vector. For safe treatment, one would be able to modify a controlled number of cells with known lifetime, which in-principle can be achieved with a flow electroporation system.

Recent developments in micro-fabrication technology facilitated the development of microfluidic electroporation to address the disadvantages of traditional electroporation approaches [137, 138, 139, 140]. Here we present a low cost, high cell viability and high-throughput electroporation method based on a novel, microfluidics-based nanoporous membrane/electrodes approach. Gold electrodes were introduced on the entrance and exit

of an Anodic Aluminum Oxide (AAO) membrane through sputtering and gold electro-less plating. Voltages as low as 1V applied across the 60 μm membrane thickness generated sufficient electric field for cellular electroporation at pore entrances. Standard photo-lithography was used to create PDMS micro-channels on the membrane/electrodes system with a channel height matched to Leukocyte dimensions. HL-60 cells (difficult to transfect cells) were continuously squeezed through the micro-channel in contact with the nanoporous electroporation electrode. Low voltage due to nm-scale concentrated electric fields at pore entrances in a periodic array resulted in high cell viability while maintain high transfection rate. Importantly, the transfection model reagent was electrophoretically pumped from the reservoir across the membrane/electrode system to the micro-fluidic channel, which reduced the reagent use by 8 fold.

5.2 Experimental details

5.2.1 Materials

All the chemicals were used as received. 200nm pore diameter Anodic aluminum oxide (AAO) membrane was purchased from Whatman. Gold (I) thiosulfate was purchased from Alfa Aesar. Ascorbic acid was purchased from EM Science. Lucifer yellow CH dilithium salt (LY, MW~457, 428/540 nm) and Propidium iodide (PI, MW~668, 535/617 nm) were purchased from Sigma Aldrich. Isotonic phosphate-buffered saline was purchased from Mediatech. Negative photoresist SU-8 3005 was obtained from MicroChem. Silicon wafers was obtained from University Wafer, South Boston, MA. RTV615 001-KIT (Polydimethylsiloxane prepolymer) was purchased from MG chemicals, Toronto, Canada. Purified water was prepared using a Millipore Milli-Q water

purification system with 18.0 MΩ.cm resistivity.

5.2.2 Cell culture

HL-60 cells were purchased from the American Type Culture Collection (ATCC) and cultured in RPMI 1640 (Invitrogen) media supplemented with 10% Fetal bovine serum (FBS) and 1% penicillin-streptomycin-L-glutamate (PSG, Sigma Aldrich) under standard incubator conditions (i.e., humidified, 5% CO2/95% air environment maintained at 37^{o}C). The cells were fed and split every 2-3days to maintain the cell density within cultures between 2.5×10^5 and 1.0×10^6 cells /ml.

5.2.3 Device fabrication

Nanoporous membrane electrodes were synthesized by gold plating on commercial Anopore aluminum oxide (AAO) membranes. Gold sputtering was first performed to create gold seed for the gold electro-less plating. Sputtering was performed with a Cressington Coating System (Ted-Pella) with calibrated quartz crystal monitor with background pressure of 0.02 mbar at 100W power supply. No intermediate wetting layer (i.e. Ti/TiO2) on Al2O3 was needed for seeding the Au layer. A thin (5 nm) layer of gold was sputtered on both the top and bottom of the AAO membranes followed by electroless plating. Electroless-plating was performed with membrane in 50 mM pH 7.0 phosphate buffer containing 1.6 mM sodium gold (I) thiosulfate and 2.68 mM ascorbic acid.

The micro-channel master was fabricated following standard soft lithography procedures[141]. First, a photo-mask containing clear 7mm ×4mm rectangles was designed using Adobe illustrator and printed on high resolution transparency film. Negative

photoresist SU-8 3005 was pippeted on to a 4cm×4cm silicon wafer and spun coat at 1000 rpm to obtain 10μm thickness photoresist that acts as the channel height during PDMS mold transfer. The wafer was then baked at 95 ℃ for 3 min and exposed to UV light for 12s to replicate the pattern into the photoresist. The wafer was then baked at 95 ℃ for an additional 80s before incubation in SU-8 developer. Finally, the wafer was baked to hardness at 160 ℃ for 2 min. This master was used to generate 7mm length (L), 4mm width (W) and 10μm tall (H) channel for this study. Polydimethylsiloxane (PDMS) prepolymer resin and hardener was mixed with a mass ratio of 10:1. The mixture was stirred with a clean glass stirring rod until it became milky in appearance. The mixture was then evacuated for 2 h to remove any air bubbles in the PDMS, poured onto the master, and baked at 80 ℃ for 1 h. The cured PDMS replica was then peeled off and punched to produce inlet and outlet ports. TYGON® Polyvinyl chloride (PVC) tubing (Amazon) with 0.02 inch inner diameter and 0.06 inch outer diameter was inserted into the inlet an outlet ports respectively.

Finally, gold electrodes/membrane was bonded to the PDMS according to procedures reported by Sunkara and coworkers [142]. The gold electrode was first cleaned with piranha solution (The ratio of concentrated H_2SO_4 and H_2O_2 is 5:1) before treatment with oxygen plasma for 2 min. The oxygen plasma treated electrodes were then incubated in a 10% (volume) aminopropyltriethoxy silane (APTES) aqueous solution for 20 min. The electrode was subsequently washed with DI water and dried under Nitrogen gas for 1min. PDMS mold was also treated with oxygen plasma for 2 min. Finally the activated gold electrode and PDMS device were then placed in conformal contact at room temperature for 12h to form bonding sufficient to prevent leakage during flow experiments.

5.2.4 Electric field model

COMSOL 4.3 (COMSOL, Inc, Burlington, MA) was used to model the electric field of the device. The electric field across the membrane/electrode system was determined by solving the Laplace equation [143]

$$-\nabla \cdot (\sigma \cdot \nabla \varphi) = 0$$

Where σ and φ stand for the electric conductivity and electric potential, respectively. A stationary 2D "Electric Current" mode under AC/DC model was created for the simulation. The model geometry is described as 0.2um pores separated by 0.5um Al_2O_3 wall with a thickness of 60um. Phosphate-buffered saline is filled within the geometry pore. The electric conductivity of the phosphate-buffered saline is 0.127 S/m [144]. The electric conductivity of Al_2O_3 is 10^{-5} S/m. The boundary conditions were a constant 1V potential on the top of Al_2O_3 walls and 0V potential on the bottom of Al_2O_3 walls. The geometry was built with fine element mesh and computed. (see the supporting information for detail COMSOL instructions)

COMSOL Model instructions:

Model Wizard

1. Double click the COMSOL icon on the desktop to create a new model
2. In the select space dimension window, select 2D.
3. In Select Physics, select AC/DC > Electric Currents (ec). Click Add. Click next Study to continue.
4. Click Stationary under Preset Studies. Click done once you have finished.

Geometry

1. Draw a rectangle with 6um width and 60 um Height at (0um, 0um) position

2. Draw eleven rectangles with 0.2 μm width and 60 μm Height at positions (0 μm, 0 μm), (0.5 μm, 0 μm), (1 μm, 0 μm), (1.5 μm, 0 μm), (2 μm, 0 μm), (2.5 μm, 0 μm), (-0.5 μm, 0 μm), (-1 μm, 0 μm), (-1.5 μm, 0 μm), (-2 μm, 0 μm) and (-2.5 μm, 0 μm)

Materials

1. Open Material Browser>Built in>Water, liquid; Click select and rename as Phosphate buffer; in the materials contents column, change the electrical conductivity value to 0.127 S/m.
2. Select Phosphate buffer, in the Geometric Entity Selection area, select the following domains: 2, 4, 6, 8, 10, 12, 14, 16, 18, 20, 22
3. Open Material Browser> Built in>Alumina; Click select; in the materials contents column, change the electrical conductivity value to 10e-5 S/m.
4. Select Alumina, in the Geometric Entity Selection area, select the following domains: 1, 3, 5, 7, 9, 11, 13, 15, 17, 19, 21, 23

Domain Physics and Boundary Conditions

1. In the Model Builder, right-click Electric Currents (ec) and add electric potential
2. Select initial values under the electric currents; Put 0V as the electric potential for all domains' initial value.
3. Select Electric potential 1; manually choose the following boundaries: 3, 9, 15, 21, 27, 33, 39, 45, 51, 57, 63, 69; In the Electric potential column, put 1V as the potential for the selected boundaries.
4. Select Electric potential 2; manually choose the following boundaries: 2, 8, 14, 20, 26, 32, 38, 44, 50, 56, 62, 68; In the Electric potential column, put 0V as the potential for the selected boundaries.

Mesh

1. In the Model Builder, under Component 1 click Mesh 1. In the Mesh settings window, under Mesh Settings, select Fine from the Element size list**.**
2. Click the Build All button on the Mesh settings window toolbar.

Study

1. Right-click Study 1 and select Compute (or press F8)

Displaying results

1. In the Model Builder, right click Result and select 2D plot group
2. Right click 2D plot Group and select surface
3. Select surface and in the expression column put “ec.normE” with unit “V/cm”
4. Plot the result

5.2.5 Static electroporation without PMDS channel

Suspended cell electroporation without vacuum filtration: 1.4 mL of solution of HL60 cells in RPMI media at a concentration of 1.3 million cells per milliliter was suspended on top of the gold-plated AAO membrane tissue culture insert (Nunc Anopore® Membranes).The working electrode was connected to the top bottom electrode/membrane surface, while the counter/reference electrodes to the bottom electrode/membrane surface. Cells were electroporated at 1V with 20 ms pulses of electricity spaced 1 s apart. A total of ten pulses of electricity were applied. The insert was then allowed to sit in the holding for 35 minutes. The cell solution was then centrifuged and the supernatant was removed. Fresh cell media was added, and the process was repeated twice more, to remove extracellular LY from solution before cell visualization under the fluorescent microscope as described before.

Cell electroporation with vacuum filtration: The cell insert was sealed above a vacuum filtration flask for 3 hours to allow the cells to come in direct contact with the AAO membrane before performing the electroporation.

5.2.6 Flow-through electroporation

A syringe pump (The New Era Pump Systems, Inc) was connected to the inlet end of the device through clear PVC tubing. A potentiostat (EA164 QuadStat, eDAQ Pty Ltd) controlled by an e-corder 410 (eDAQ Pty Ltd) with ChartTM software was used as a pulse generator. The working electrode was connected to the top electrode/membrane surface, while the counter/reference electrodes to the bottom electrode/membrane surface, as shown in Fig.4. The channel was flushed with phosphate-buffered saline for 3min at 1ml/min to remove impurities within the channel.

Prior to electroporation, HL-60 cells were centrifuged at 200g for 5 min and re-suspended in phosphate-buffered saline containing 1mg/ml Lucifer Yellow to a final concentration of 1×10^6 cells /ml. The cells/Lucifer Yellow mixture was subsequently flowed through the device for electroporation while a pulse voltage (20ms per pulse in 1 sec intervals) across the membrane was applied. Cells were collected from the outlet and incubated in room temperature for 35mins. The cells were then ringed three times with phosphate-buffered saline prior to transfection and viability assay.

In a separate experiment to show the efficient electrophoretic pumping of Lucifer Yellow reagent across the membrane, only cells in PBS buffer were flowed through the channel while 1mg/ml Lucifer Yellow was placed beneath the electrode/membrane device during the electroporation process.

5.2.7 Transfection and viability assays

A final 1ug/ml propidium iodide (PI) was added to the washed cells for cell viability assay.

Both phase contrast and fluorescent images of cells were captured using an Eclipse LV100D-U fluorescence microscope (Nikon) with NIS-Elements BR 3.0 software (Nikon). An LSR II flow cytometer (Becton -Dickinson) with Becton - Dickinson interfaced to FACsDiva computer software was used to quantify dye uptake by electroporated cells and cell viability. At least 10,000 HL-60 cells were acquired at a rate up to 1000 cells/s for each sample. A 488-nm line of an argon laser (Innova, Coherent, Palo Alto, CA) was used to excite LY in transfected cells and PI in dead cells. The two filters used were Percp-Cy5.5 filter (695/40) for PI emission detection and FITC (530/30) for LY emission detection. Spectral compensation was conducted to account for the overlap in emission between propidium iodide into the Lucifer yellow.

5.3 Results and Discussion

To achieve cellular electroporation at low voltages, micron-scale distance between the two electrodes is required. This can be easily achieved with electrodes on each side of commercially available AAO membranes that are 60μm thick. Gold sputtering deposition on both the top and bottom of AAO membrane served as catalytic seeds for the subsequent electro-less plating of thicker gold layers to reduce pore size and overall porosity. Figure 5.1 shows the typical SEM images of the bare membrane and the membrane after sputtering and electro-less plating fabrication steps.

Figure 5.2 shows the simulated electric field distribution at top entrance of

membrane/electrodes using COMSOL modeling software. The modeling of electric field (EF) concentration at pore entrance shows a "butterfly EF distribution shape" with EF as high as 540V/cm at the pore edges and EF as low as 100 V/cm in the pore center. The bulk pore EF is near 167 V/cm, which is simply approximated by applied voltage divided by thickness (1V/60μm). Table 1 summarizes the voltages applied in the experiments and the resulting field intensities in the bulk pore and at pore entrance. The maximum EF field at the pore entrance is proportion (3.2 times) the bulk applied field. In the common electroporation process, the whole cell is placed between electrodes for electroporation with the entire area of the plasma membrane perpendicular to desired electric field (150-424 V/cm). This gives the fundamental reason for the difficulty of finding an appropriate electroporation voltage in the conventional geometry: too high a voltage and large area damage to the plasma membrane is not physiologically repairable thereby killing the cell, while at too low a voltage there is no pore formation. Ideally one would localize strong electric in nm-scale areas with a regular arrayed pitch allowing for high poration that is repairable and inject the transfection reagent during the voltage pulse. By injecting the reagent during poration, it is possible to have the cell nearly immediately repair electroporation damage, thereby increasing cell viability. Our gold electrode/membranes system has the strongest electric field at the pore entrances which is a relatively small (~5%) percentage of the cell's plasma membrane area with regular 200nm spacing. Also charged transfection reagents can be electrophoretically pumped across the membrane into the cell.

To take advantage of this geometry, the cells must be in direct contact with the membrane/electrode surface. Experiments with suspended cells above AAO/electrode

membranes failed to transfect until a filtering vacuum was applied to make cells contact the electrode, however this approach is not scalable to large numbers of cells (Figure 5.9 in supporting information). Due to the nature of the vascular system constricting to cellular sizes, white blood cells are robust to mechanical deformation and can be flowed through channels with cellular dimension to give contact with the membrane/electrode surface. HL-60 cells have 10-20 μm diameters thereby requiring a channel height 10 μm above the Au/AAO membrane surface to squeeze the cells into direct contact with the pore entrances. Figure 5.4 shows the schematic setup for the flow-through electroporation of HL-60 cells using the PDMS channel over the electrodes/membrane system.

Fluorescence microscopy of cells flowed through the device, in Figure 5.5, demonstrate the successful electroporation of cells to introduce cell-impermeable Lucifer yellow as a transfection agent model compound. When HL-60 cells flow through the micro-channel, the cell wall is forced into intimate contact with the electrode pore entrance and exposed to a 20 ms voltage pulse to porate the cell. In this case the Lucifer yellow (LY) transfection model reagent is in the bulk carrier solution and enters the cells. Since the living cell repairs the porated cell wall, the cell wall impermeable LY is trapped inside the cell allowing fluorescent microscopy imaging of transfected cell (green). To image dead cells, those highly permeable walls are readily stained with propidium iodide. Importantly there were no imaged transfected cells and minimal dead cells in the control (0V) experiment showing that the act of flowing of white blood cells through the micro-channel over the membrane does not damage/porate the cell walls. As the applied voltage is increased from 1 to 4V, the electric field within the electrode pore entrance is increased,

resulting in an increased cell transfection. This applied voltage is significantly low than commonly used 20-100V and prior reports (9V) with adherent cells on AAO membranes. Unlike traditional cuvette electroporation process, there were very few dead cells imaged in this process. Fluorescent microscopy suffers from low statistical sampling, thus detailed cell viability and cell transfection efficiency were determined using high-throughput and automated flow cytometry using the same fluorescent transfection marker (green) and dead cell marker (red). As shown in Figure 5.6, when the voltage increased from 0V to 4V, the cell population exhibits a fluorescence intensity shift from live non-transfected (zone Q3) to live transfected (zone Q1), which indicated the statistically valid increase of cell transfection while retaining high cell viability.

Traditionally, the cell transfection efficiency and cell viability are trade-off parameters with an inherent non-ideal maximum. At low voltage, the cell transfection efficiency is low and the cell viability is high because cells undergo a low level of reversible electroporation before the transfection reagent can enter the cell. At high voltage, the cell transfection efficiency is high with significant irreversible poration resulting in low cell viability. Our electroporation device, however, showed high cell viability at high transfection rates, as shown in figure 5.7. At 1 V applied voltage the device showed ~30% cell transfection efficiency and >90% cell viability while at 4 V applied voltage device showed ~65% cell transfection efficiency with similar >90% cell viability.

There are two likely reasons to account for the high cell viability in our device. First, unlike traditional electroporation processes where the whole cell membrane is exposed to high voltage (or is it high current) electric fields, only a small part of the cell membrane

(~5%) is exposed to the nm-scale focused electric field at pore entrances in our device in a periodic array of the AAO membrane (~250nm spacing). This focused electroporation reduces the possibilities of irreversible electroporation and cell death. In traditional electroporation process, however, the whole cell was exposed to unfocused strong electric field, thus there is a much higher possibility of large areas irreversible electroporation. Second, the electric current induced joule heating in our device is much lower than the conventional electroporation device, where temperatures can increase as high as 10 K [140]. The electric current ranges from 1 uA to 8 uA when the applied 20ms pulse voltage at 1s interval ranges from 1 V to 4 V. The joule heating induced temperature rise can be calculated using the following equation:

$$U \times I \times t = c \times m \times \Delta T \qquad (1)$$

Where U is applied pulse voltage, I is current, t is time, c is the water specific heat capacity, m is the flowing water total mass and ΔT is the rising temperature. In the worst case (with the flow rate of 1 mL/h, the highest voltage 4 V, and the highest current of 8 uA), the calculated joule heating induced temperature gain is 5×10^{-6} K, thus eliminating that potential mechanism of cell stress.

Another critical merit to this device design is that the transfection reagents can be electrophoretically pumped from the reservoir across the membrane/electrode system into the cell. This can dramatically reduce the amount of expensive-to-produce transfection reagents that are traditionally mixed with the flowing cell solution and need to be at concentrations high enough to enter the cell before the porated cell wall is repaired. Thus, only a small part of the reagents are transferred into the cell and the rest are not reused and are usually discarded. Typically, 10^9 cells are needed for a clinical application, which

often would require 1 L 10^6cells/ml mixed with 1mg/ml reagents solution. With our Lucifer yellow model transfection reagents the total amount needed for a single clinical trial would be 1000 mg. By electrophoretically injecting the transfection agent into cells from a reservoir located under the membrane/electrode we can greatly reduce the amount of expensive reagents used during the transfection process. To demonstrate this, aliquots (2 mL) of 1mg/ml Lucifer yellow was placed beneath the membrane/electrode system (Figure 5.4). The negatively charged Lucifer yellow would be electrophoretically pumped to the micro-channel and delivered into the cell membrane under high electric field generated by the pulse voltage. As shown in figure 5.8, the simultaneous electrophoresis pumping of Lucifer yellow and electroporation of HL-60 cells show similar cell transfection efficiency and viability as shown in Figure 5.6. The amount of Lucifer yellow being pumped across the 4mm×7mm channel during 20ms electrophoretic pumping can be calculated by

$$m = \mu \times E \times c \times t \times S \times 50\% \qquad (2),$$

where μ=8×10^{-5} cm^2/(V.s) is the Lucifer yellow electrophoretic mobility [145], E=167 V/cm is the electric field, c =1mg/ml is the Lucifer yellow concentration, t=0.02s is the pumping duration, S is the channel area, and 50% is the average membrane porosity. Based on equation 1, the amount of Lucifer yellow pumped across the 4mm×7mm channel per pulse is 3.7×10^{-5} mg. To process 1000ml 10^6cells/ml cells at pumping rate 1ml/h, the needed electrophoretic pulse number is 3.6×10^6, requiring 135 mg Lucifer yellow provided beneath the membrane system. This is 8 fold less (13.5%) than the amount needed when LY is simply mixed with HL-60 cell solution in a conventional flow electroporation approach.

The last merit of the flowing electroporation system is that it can continuously transfect a large number of cells. Traditionally, the cells and biomolecules are mixed together for electroporation in a fixed-volume cuvette with two plate electrodes. Thus, electroporation is performed in a batch mode with a small number of cells. In our device, cells can be continuously flowed through 10 μm height channels with the pumping rate controlled by the syringe pump. More importantly, our device can be easily scaled up by increasing the width and length of the PDMS channel and increasing the voltage pulse frequency. In our experiment, a single 20 ms pulse duration (t_p) was chosen for the HL-60 transfection process which was applied every second to match the cell residence time in the channel. The cell residence time can be determined by the channel dimensions (H, L, W) and the cell solution volume flow rate (v).

$$t = \frac{HWL}{v} \text{ (s)} \qquad (2)$$

With a flow rate 1ml/h, channel width (W) 4 mm, channel length (L) 7 mm and channel height (H) 10 μm, a 1s cell residence time was chosen according to equation 1 for our experiment. The minimum transit time for cells to receive a single electroporation pulse and purge the channel is twice the time of the 20ms voltage pulse duration (t_p). With commonly available concentration of cells ~1×10^6 /ml, a 1L/h flow rate for one hour would deliver the 10^9 cells required for clinical trials [146]. By rearranging Equation 2, the required planar membrane active area (A=L×W) is given by:

$$A = \frac{2t_p v}{H} \qquad (3)$$

Thus using equation (3), a 3.3cm x 3.3 cm membrane with 40 ms pulse period would give the necessary 1 L/h flow rates for clinical use. This is an area readily achievable with

commercially available materials.

5.4 Conclusions

A robust nanoporous membrane/gold electrodes system has demonstrated the continuous electroporation of HL-60 cells in a flowing white blood cell suspension culture. COMSOL simulation showed that low voltages (1-4 V) can generate sufficient electric field for electroporation at the electrode pore entrances with nm-scale focus and regular periodicity. The low voltages, low joule heating and periodic poration sites allow for high cell viability (>90%) and 65% cell transfection efficiency. HL-60 cells (10-20 μm diameter), a cell line recognized to be difficult to transfect, can be "forced" to interact with the electrode pore entrance and exposed to high electric field when passing through a 10 μm height micro-fluidic channel above the membrane/electrodes. This device can be scaled up to increase the cell sample volume by simply varying the geometry of the micro-fluidic channel and/or pulse voltage frequency for faster residence time. Finally, we demonstrated that Lucifer yellow can be electrophoretically pumped across the membrane/electrodes system during the electroporation process from a reservoir located below the flow chamber, which greatly reduced (8 fold) the amount of expensive biomolecules used during the transfection process. We envision that this membrane/electrode system will show promise in clinical applications where low-cost, high cell viability and high volume transfected methods are needed without the risk of viral vectors. In particular the genetic modification freely mobile white blood cells to either target disease cells or express needed protein/enzyme biomolecules is an important target platform enabled by this device system.

Table 5.1 The applied voltages across the device (V) and the resulted field intensities

V(V)	**0**	**1**	**2**	**4**
Bulk Pore Field (V/cm)	0	167	334	668
Maximum Field (V/cm)	0	540	1080	2160

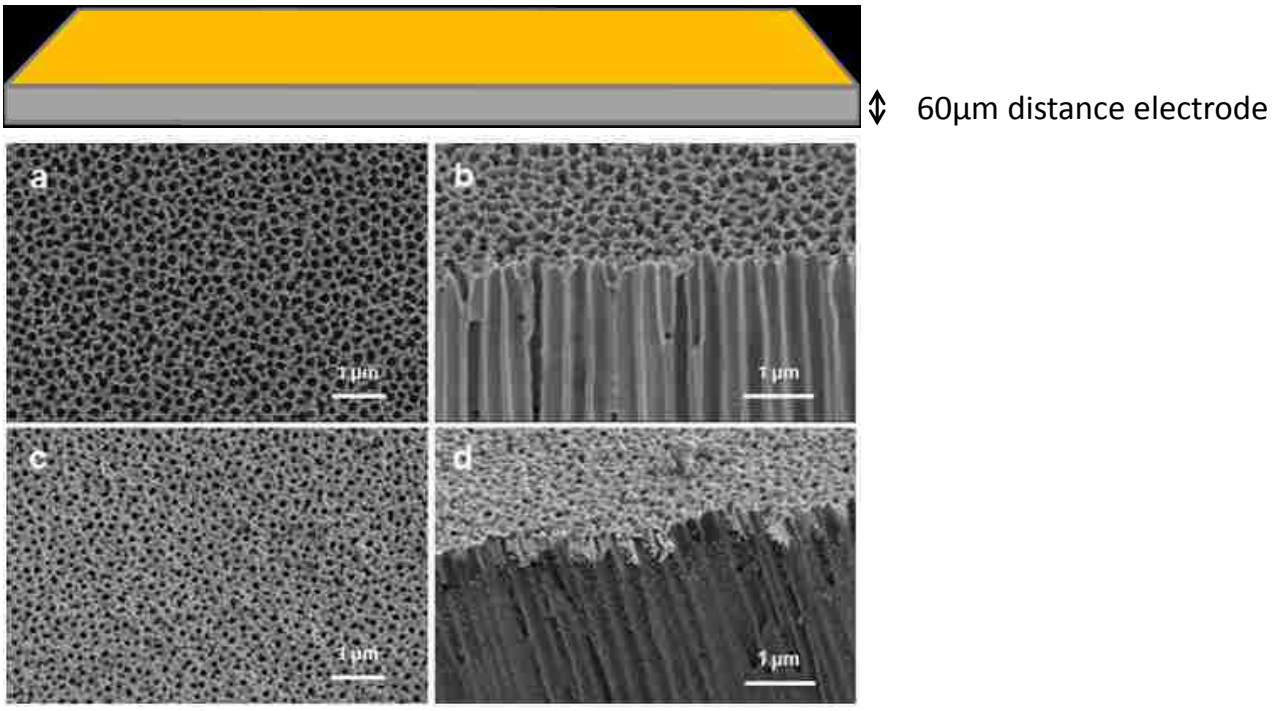

Figure 5.1 SEM images of cell culture side of AAO membrane. (a) Top view of bare membrane. (b) Cross section of bare membrane. (c) Top view of gold-coated membrane. (d) Cross section of gold-coated membrane.

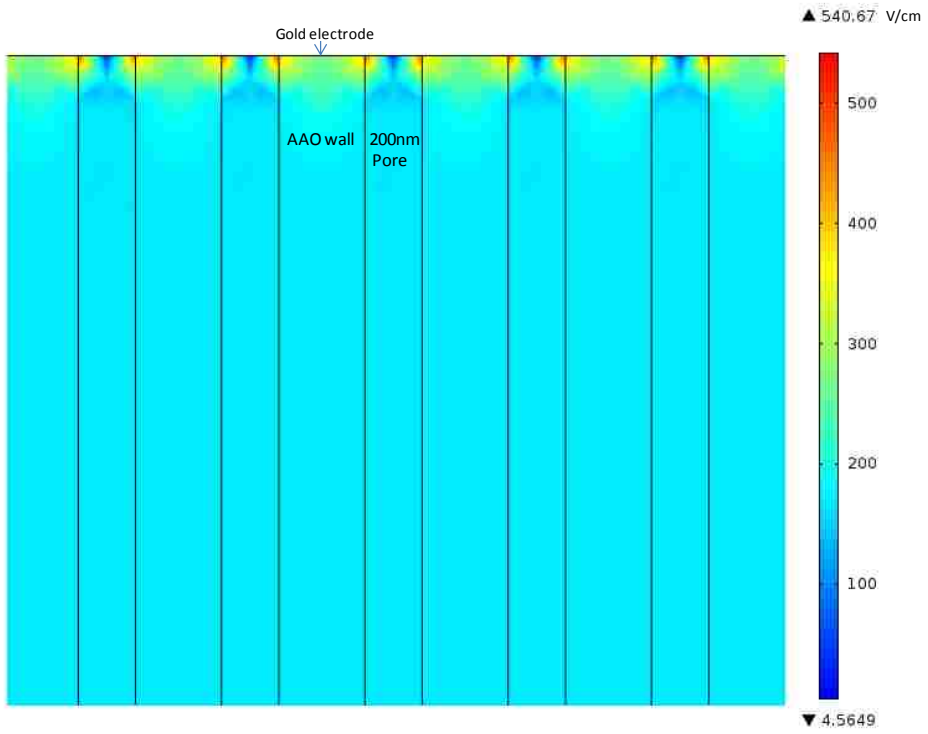

Figure 5.2 COMSOL simulation of electric field (EF) distribution at the top of membrane/electrode system at 1V applied voltage

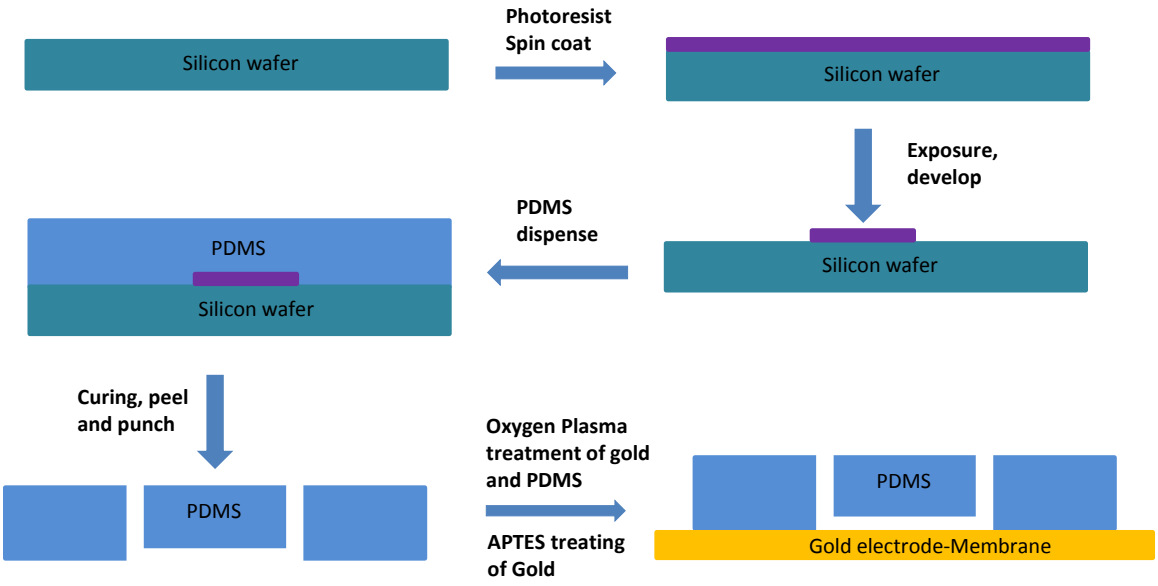

Figure 5.3 Fabrication process of PDMS-membrane/electrodes device for cellular electroporation

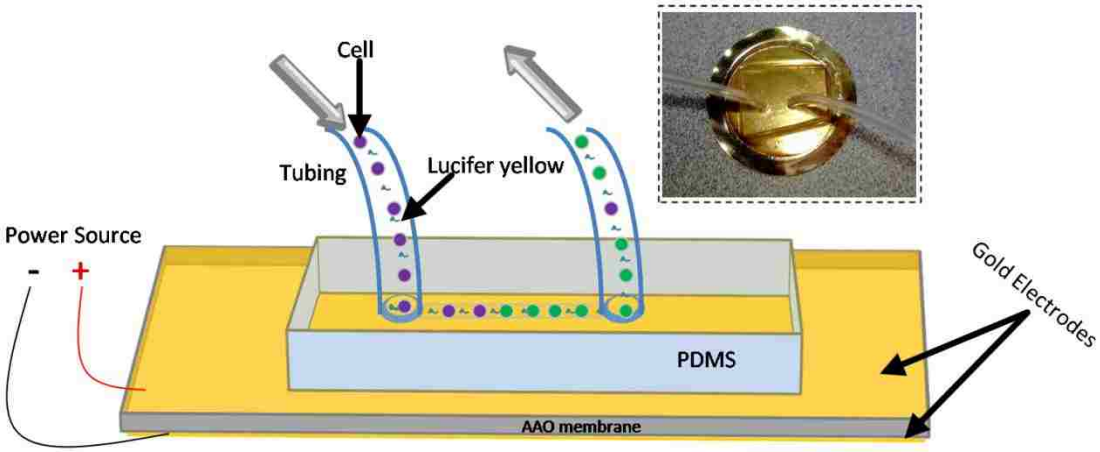

Figure 5.4 Schematic illustration of the setup for large-volume flowing cell transfection

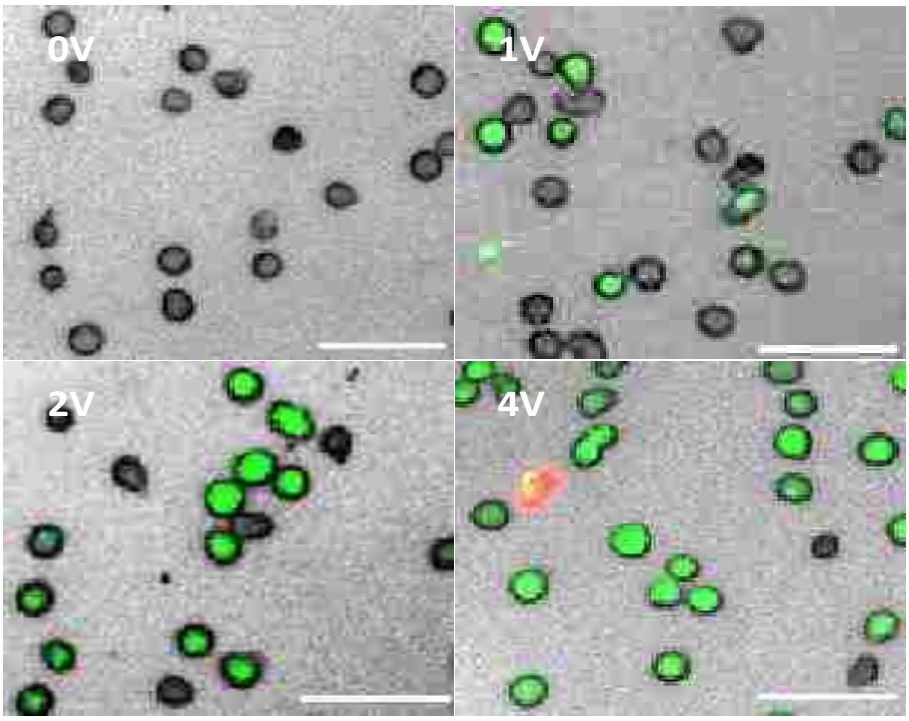

Figure 5.5 Fluorescent image overlay after cellular electroporation using the micro-channel device.

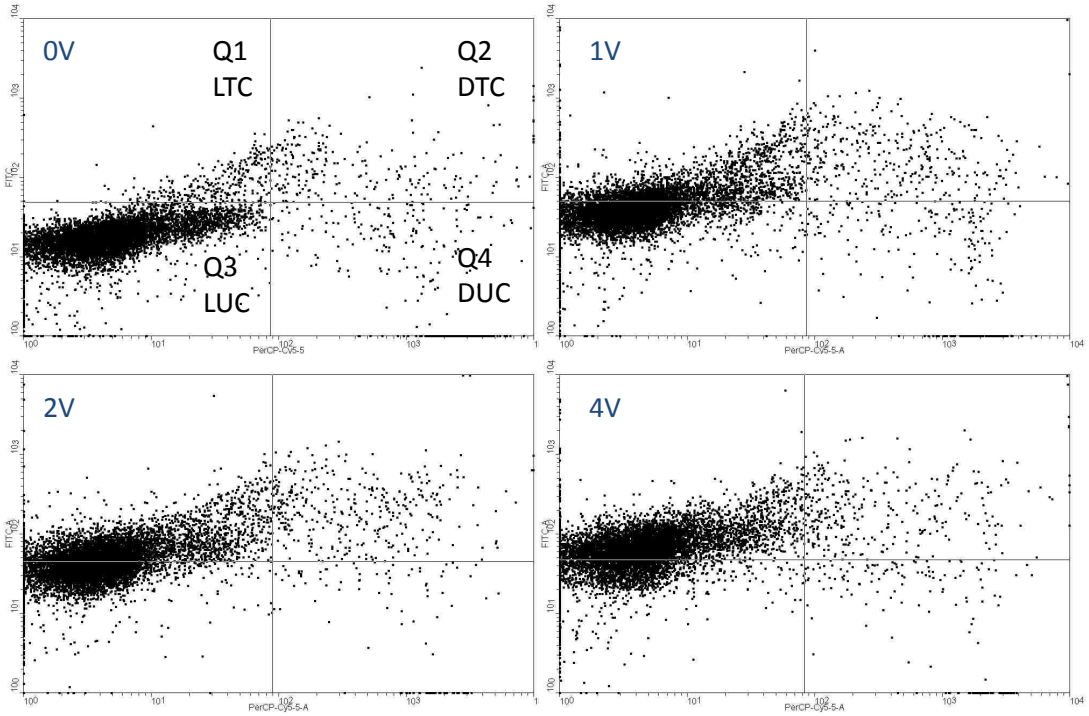

Figure 5.6 Representative two dimensions dot plot of flow cytometry data after different electroporation voltages. Quandrants are live transfected cells (Q1, LTC), dead transfected cells (Q2, DTC), live un-transfected cells (Q3, LUC) and dead un-transfected cells (Q4, DUC).

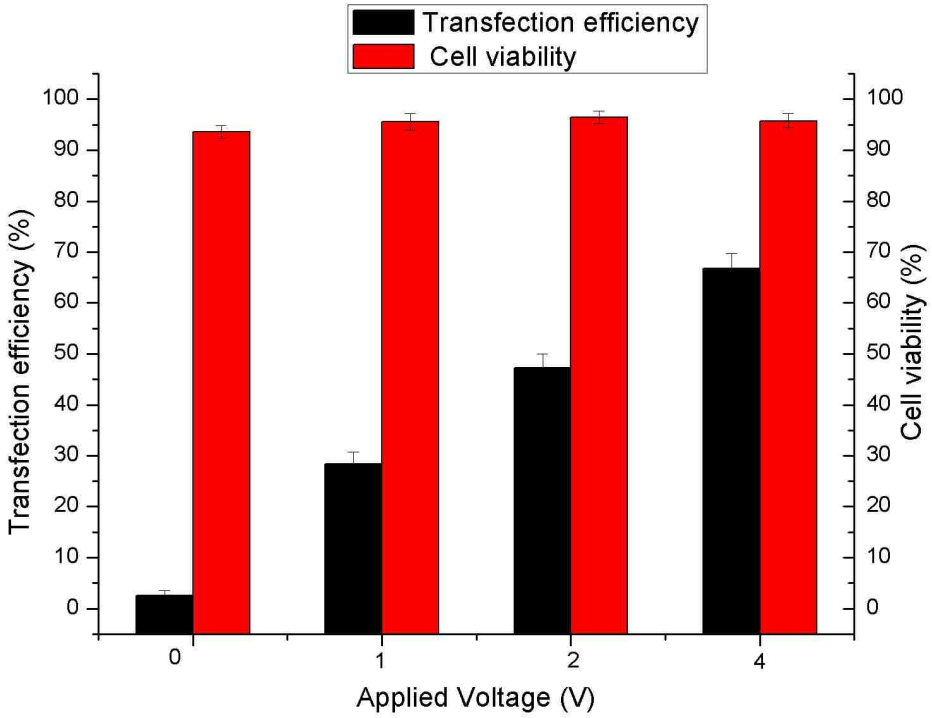

Figure 5.7 Cell transfection efficiency (electroporated live cells/ total live cells= $\frac{Q1}{Q1+Q3}$, and cell viability (live cells/total cells = ($\frac{Q1+Q3}{Q1+Q2+Q3+Q4}$) as a function of applied electroporation voltage. Data shown are the mean ± S.D. of results obtained from three independent transfection experiments with .flow cytometry data (total number of cells analyzed is 10,000 in each run)

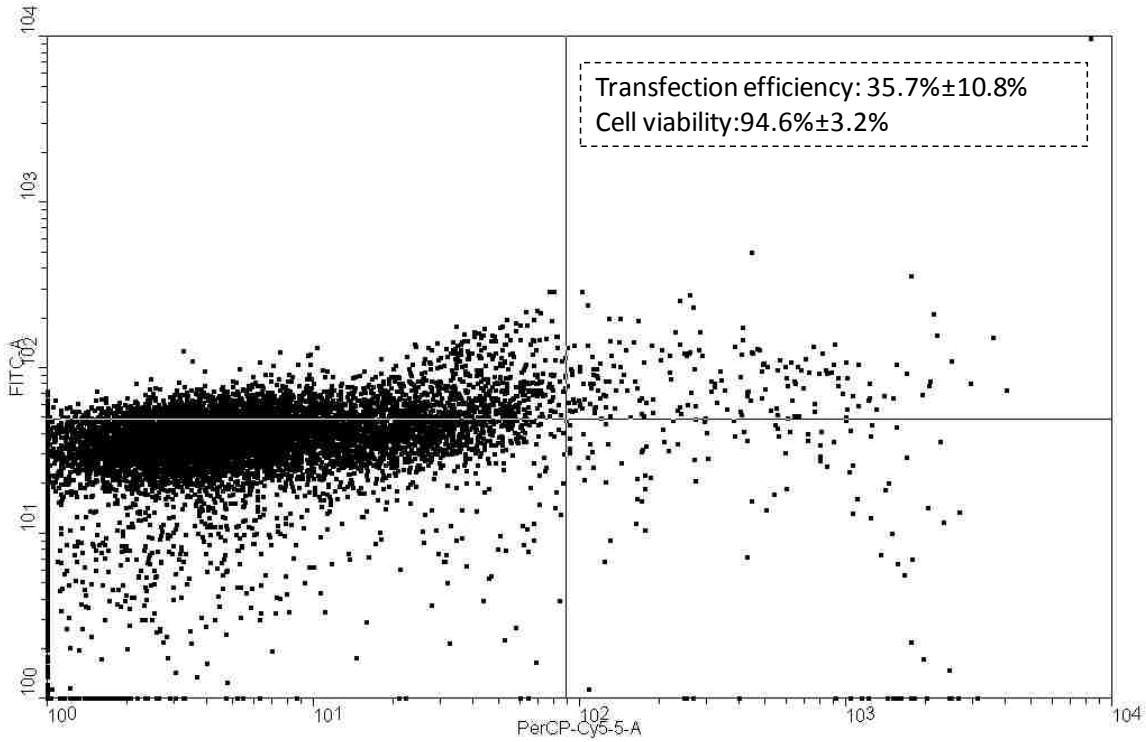

Figure 5.8 Representative two dimensions dot plot of flow cytometry data for simultaneous electrophoresis pumping of Lucifer yellow and transfection of HL-60 cells at 1v applied voltage. Quadrants 1-4 are as defined in Figure 5.6.

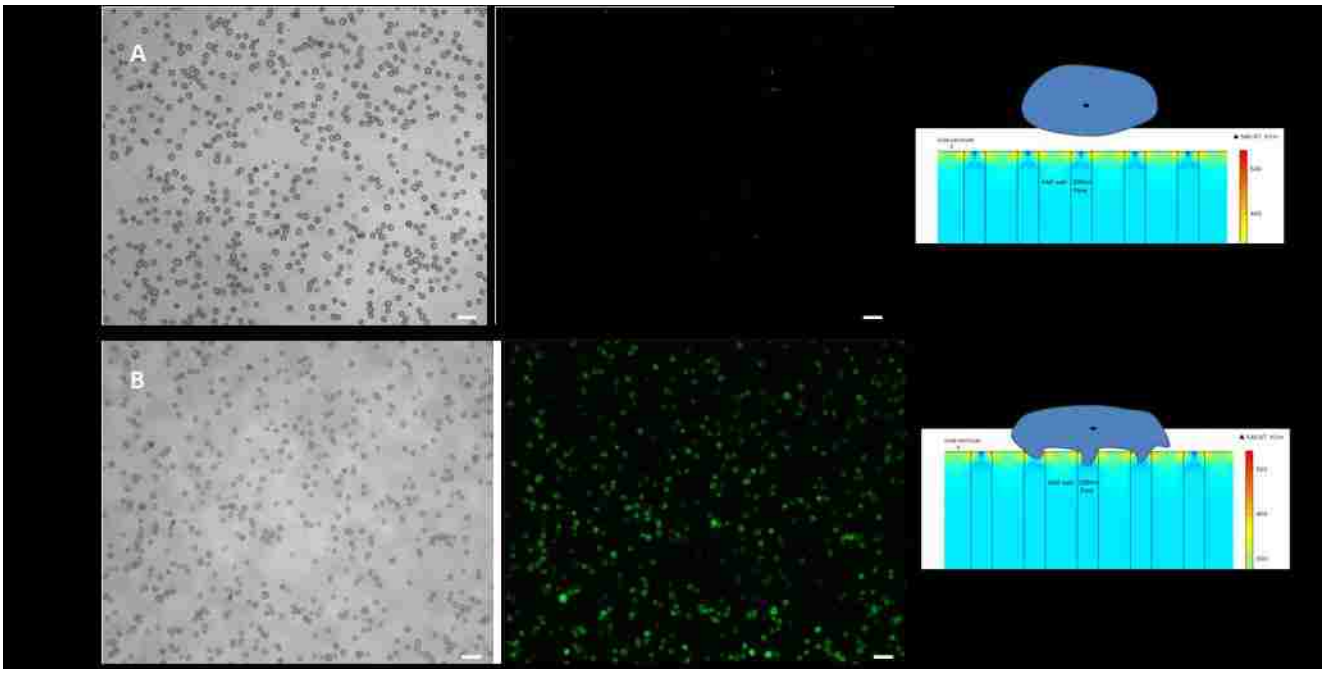

Figure 5.9 Optical and fluorescent images of HL-60 cells before and after electroporation without (A) and with (B) vacuum filtration; scale bars, 50 μm. Good contact between cells and electrodes is necessary for efficient transfection.

Chapter 6 : Conclusion

AAO membrane is an attractive platform for biopharmaceutical applications due to its minimal auto-fluorescence, nontoxicity, and non-specific binding. In this dissertation, a gold electro-less plating method was developed to introduce gold electrodes on the entrance and exit of AAO membranes. Gold electro-less plating on the pore entrance of AAO membranes brings three benefits. First, the surface of gold can be easily modified with different chemistry for the attachment of receptor chemistry and enzyme immobilization. Second, voltage can be applied on the micro-scale distance gold electrode on top and bottom of AAO membranes to generate high electric field and facilitate the ion transportation within the AAO membrane. Third, the pore size of AAO membrane can be easily controlled by changing the electro-less plating time onto the initial Au seed layer to a pore size match to protein or enzyme dimension. These three benefits of the nano-scale membrane electrodes are the basis for the three bio-applications reported in this dissertation.

An active membrane system based on nm-scale electrodes for continuous protein purification was first demonstrated in this dissertation. The electrodes are located at the first 20nm of pore entrances to specifically capture targeted proteins and block non-specific protein transport through the pores during the binding cycle. During the release cycle, concentration of imidazole is controlled to keep the pore blocked while releasing proteins at the bottom edge of the electrode. Numerical simulation of the pulse pumping cycles coupled with His-GFP releasing kinetic was used to determine and optimize pulse pumping condition, enabling mimic biological membranes for efficient protein separation. A separation factor for GFP:BSA of 9.7 was achieved with observed GFP electrophoretic

mobility of 3.1×10^{-6} cm^2 s^{-1} V^{-1} at optimal pulse pumping conditions. Most importantly, the membrane electrode pulse pumping process show the ability to purify His_6-OleD Loki variant directly from crude *E. coli* extracts expression broth, simplifying the separation process as well as reducing biopharmaceutical production costs.

Nano-scale electrodes at the entrance and exit of AAO membranes for enzyme immobilized were demonstrated to mimic natural complex-enzyme system. Genetically modified His-tagged OleD Loki variant was immobilized onto nm-scale electrodes at the pore entrances/exits of modified AAO membranes through His_6-tag affinity. Immobilized enzyme on membrane-electrodes system allows precise control of the substrates residence time through the enzyme, thus eliminating unwanted hydrolytic side reactions observed on solution-based enzymatic reaction. Two-step sequential reactions were demonstrated to mimic natural complex-enzyme system with the ability of discrete control of each independent step *via* selective reagent feedstock composition exposure of the top and/or bottom surface of immobilized membrane/electrode system. Finally, the system allows a convenient one-step immobilization and purification of *N*-His_6-OleD Loki variant directly from crude *E. coli* extracts expression broth. This AAO membrane/electrode system offers an opportunity to expand the study and bio-catalytic utility of multi-enzyme cascades with directed mass transport

A robust nanoporous membrane/gold electrodes system has demonstrated the continuous electroporation of HL-60 cells in a flowing white blood cell suspension culture. Gold electrodes were introduced on the entrance and exit of an AAO membrane through sputtering and gold electro-less plating. Voltages as low as 1V applied across the 60 μm membrane thickness generated sufficient electric field, as simulated by COMSOL,

for cellular electroporation at pore entrances. PDMS micro-channels on the membrane/electrodes system with the 10 micron channel heights were created using standard soft-lithography designed to squeeze the leukocyte dimensions (~15 μm) into the high electric field electrode pore entrance. The low voltages, low joule heating and periodic poration sites allow for high cell viability (>90%) and 65% cell transfection efficiency. This device can be scaled up to increase the cell sample volume by simply varying the geometry of the micro-fluidic channel and/or pulse voltage frequency for enhanced residence time. Importantly, transfection reagent was electrophoretically pumped from a microscale reservoir across the membrane/electrode system to the micro-fluidic channel, which reduced the amount reagent used by 8 fold compared to traditional electroporation strategies. In particular genetic modification of circulating white blood cells or diseased cells to express target protein/enzyme biomolecules is an important target platform enabled by this device system.

LIST OF ABBREVIATIONS

4-Me-Umb	4-methylumbelliferone
AAO	Aluminum oxide
APTES	Aminopropyltriethoxy silane
BSA	Bovine serum albumin
CNT	Carbon nanotube
His-GFP	His-tagged green fluorescence protein
IMAC	Immobilized metal ion affinity chromatography
LY	Lucifer yellow
NTA	Nα, Nα-Bis(carboxymethyl)-L-lysine
PI	Propidium iodide
PNP-Glc	2-chloro-4-nitro-phenyl-β-D-glucopyranoside
PDMS	Polydimethylsiloxane
PVC	Polyvinylchloride
PTFE	Polytetrafluoroethylene
PVDF	Polyvinylidene fluoride
PE	Polyethylene
PCTE	Polycarbonate track-etch
SEM	Scanning Electron Microscope
TIRF	Total internal reflection fluorescence
UDP	Uridine Diphosphate
IEC	Ionic exchange chromatography
HIC	Hydrophobic interaction chromatography
SEC	Size exclusion chromatography

REFERENCES

1. Strathmann, H.; Giorno, L.; Drioli, E. An introduction to Membrane Science and Technology, *Ufficio Pubblicazioni e Informazioni Scientifiche*, Roma, **2006**, pp.8–9

2. Ulbricht, M. Advanced functional polymer membranes. *Polymer.* **2006**, *47*, 2217-2262.

3. Karagiannis, I. C; Soldatos, P. S. Water desalination cost literature: review and assessment. *Desalinatio.* **2008**, *23*, 448-456.

4. Fritzmann ,C.; L öwenberg, J.; Wintgens, T.; Melin, T. State-of-the-art of reverse osmosis desalination. *Desalinatio.* **2007**, *216*, 1-76.

5. Ho, M. T.; Allinson, G. W.; Wiley, D. E. Reducing the Cost of CO2 Capture from Flue Gases Using Membrane Technology. *Ind. Eng. Chem. Res*. **2008**, *47*, 1562–1568.

6. Yao, Jingyuan, "FABRICATION OF SWNT s FOR WATER DESALINATION AND MULTILAYER STRUCTURE FOR DNA SEQUENCING" (2012). Theses and Dissertations--Mechanical Engineering. Paper 12. http://uknowledge. uky .edu/me_etds/12.

7. Baker, R.W. Membrane technology and applications (2nd ed) Wiley, Chichester (**2004**)

8 . Kowalczyk, S.W.; Blosser, T. R. Dekker, C. Biomimetic nanopores: learning from and about nature. *Trends in Biotechnology.* **2011**, *29*, 607-614.

9. Hibino, H.; Inanobe, A.; Furutani, K.; Murakami, S.; Findlay, I.; Kurachi, Y. Inwardly Rectifying Potassium Channels: Their Structure, Function, and Physiological Roles. *Physiological review.* **2010,** *90*, 291-366.

10. Castillia, C. S. D.; Niepel, M.; Rout, M. P. The nuclear pore complex: bridging nuclear transport and gene regulation. *Nature Reviews Molecular Cell Biology*. **2000,** *11*, 490-501.

11.Steinbrecht, R. A. Pore structures in insect olfactory sensilla: a review of data and concepts. *Int. J. Insect Morphol. Embryol*. **1997,** *26*, 229–245.

12.Yusko, E. C. *et al*. Controlling protein translocation through nanopores with bio-inspired fluid walls. *Nature nanotechnology*. **2011**, *6*, 253-260.

13. http://harunyahya.com/en/books/21657/The-Miracle-In-The-Cell Membrane/chapter/8206/Complex-Transportation-Systems-in-The-Cell-Membrane

14. Hinds, B. J. Dramatic Transport Properties of Carbon Nanotube Membranes for a robust protein channel mimetic platform. *Curr. Opin. in Solid. State & Mater. Sci*. **2012**, *16*, 1-9.

15. Murata, K.; Mitsuoka, K.; Hirai, T.; Walz, T.; Agre, P.; Heymann, J. B. Structural determinants of water permeation through aquaporin. *Nature* **2000,** *407*, 599–605

16. Li, J. et al. Ion-beam sculpting at nanometer length scales. *Nature* **2001**, *412*, 166–169.

17. Storm, A.J. et al. Fabrication of solid-state nanopores with single-nanometre precision. *Nat. Mater.* **2003**, 2, 537–540.

18. Caspi, Y. *et al.* Synthetic mimic of selective transport through the nuclear pore complex. *Nano Lett.* **2008**, *8*, 3728–3734.

19. Tian, Y. *et al.* A biomimetic zinc activated ion channel. *Chem. Commun.* **2010**, *46*, 1682–1684.

20. Yameen, B.B. *et al.* Synthetic proton-gated ion channels via single solid-state nanochannels modified with responsive polymer. *Nano Lett.* 2**009**, *9*, 2788–2793.

21. Hinds, B. J.; Chopra, N.; Rantell, T.; Andrews, R.; Gavalas, V.; Bachas, L. G. Aligned Multiwalled Carbon Nanotube Membrane. *Science.* **2004**, *303*, 62–65.

22. Majumder, M.; Chopra, N.; Andrews, R; Hinds, B.J. Nanoscale hydrodynamics: Enhanced flow in carbon nanotubes. *Nature.* **2005**, *438*, 44.

23. Majumder, M.; Zhan, X.; Andrews, R.; Hinds, B. J. Voltage Gated Carbon Nanotube Membranes. *Langmuir* **2007,** *23*, 8624-8631.

24. Majumder, M.; Stinchcomb, A.; Hinds B. J. Towards mimicking natural protein channels with aligned carbon nanotube membranes for active drug delivery. *Life Sciences* **2010,** *86*, 563-568.

25. Wu, J.; Zhan, X.; Hinds, B. J. Ionic Rectification by Electrostatically Actuated Tethers on Single Walled Carbon Nanotube Membranes. *Chemical Communication*. **2012,** *48*, 7979-7981.

26. Nednoor, P.; Chopra, N.; Gavalas, V.; Bachas, L. G., Hinds, B. J. Reversible biochemical switching of ionic transport through aligned carbon nanotube membranes. *Chem Mater*. **2005,** *17*, 3595–3599.

27. Nednoor, P.; Gavalasm V. G.; Chopra, N.; Hinds, B. J.; Bachas, L. G. Carbon nanotube based biomimetic membranes: mimicking protein channels regulated by phosphorylation. *J Mater Chem.* **2007,** *17*, 1755–1757.

28. Stephan, M.; Kramer, C.; Steinem, C.; Janshoff, A. Binding assay for low molecular weight analytes based on reflectometry of absorbing molecules in porous substrates. *Analyst*, **2014**, *139*, 1987–1992.

29. Dhathathreyan, A. Real-Time Monitoring of Invertase Activity Immobilized in Nanoporous Aluminum Oxide. *J. Phys. Chem. B* **2011**, *115*, 6678–6682.

30. Osmanbeyoglu, H. U.; Hur, T. B.; Kim, H. K. Thin alumina nanoporous membranes for similar size biomolecule separation. *Journal of Membrane Science*. **2009**, *343*, 1-6.

31. Jain, P.; Sun, L.; Dai, J.; Baker, G. L.; Bruening, M. L. High-Capacity Purification of His-tagged Proteins by Affinity Membranes Containing Functionalized Polymer Brushes Biomacromolecules **2007**, *8*, 3102-3107.

32. Jirage, K. B.; Hulteen, J. C.; Martin, C. R. Nanotubule-Based Molecular-Filtration Membranes. *Science*, **1997,** 278, 655-658.

33. Yu, S.; Lee, S. B.; Kang, M.; Martin, C. R. Size-Based Protein Separations in Poly (ethylene glycol)-Derivatized Gold Nanotubule Membranes. *Nano letters*. **2001,** *1*, 495-498.

34. Lee, S. B.; Mitchell, D. T.; Trofin, L.; Nevanen, T. K.; Soderlund, H.; Martin, C. R. Antibody-Based Bio-Nanotube Membranes for Enantiomeric Drug Separations. *Science*, **2002,** *296*, 2198-2200.

35. Jirage, K. B.; Hulteen, J. C.; Martin, C. R. Effect of Thiol Chemisorption on the Transport Properties of Gold Nanotubule Membranes. *Anal. Chem.* **1999**, *71*, 4913-4918.

36. Yu, S.; Lee, S. B.; Martin, C. R. Electrophoretic Protein Transport in Gold. Nanotube Membranes. *Anal. Chem.* **2003**, *75*, 1239-1244.

37. Kohli, P.; Wharton, J. E.; Braide, O.; Martin, C. Template synthesis of gold nanotubes in an anodic alumina membrane. *J Nanosci Nanotechnol.* **2004,** 4, 605-10.

38. Lam, P., Kumar, K., Winek, G., Przybycien, T. M. Electroless Gold Plating of 316 L Stainless Steel Beads. *J. Electrochem. Soc.* **1999,** *146*, 2517-2521.

39. GE Healthcare. Strategies for Protein Purification. General Electric Company- GE Healthcare Bio Sciences. Sweden. AB, Björkgatan 30, 75184 Uppsala, **2010.**

40. Janson, Jan-Christer, ed. Protein purification: principles, high resolution methods, and applications. Vol. 151. John Wiley & Sons, **2012.**

41. GE Healthcare. Hydrophobic Interaction and Reversed Phase Chromatography. General Electric Company- GE Healthcare Bio Sciences. Sweden. AB, Björkgatan 30, 75184 Uppsala, **2006.**

42. GE Healthcare. Gel filtration. General Electric Company- GE Healthcare Bio Sciences. Sweden. AB, Björkgatan 30, 75184 Uppsala, **2010.**

43. GE Healthcare. Affinity Chromatography. General Electric Company- GE Healthcare Bio Sciences. Sweden. AB, Björkgatan 30, 75184 Uppsala, **2007.**

44. Akay, G.; Erhan, E.; Keskinler, B; Algur, O. F. Removal of phenol from wastewater using membrane-immobilized enzymes: Part II. Cross-flow filtration. *Journal of Membrane Science.* **2002**, *206*, 61-68.

45. Mateo, C.; Palomo, J. M.; van Langen, L. M.; Rantwijk, F. V.; Sheldon, R. A. A new, mild cross-linking methodology to prepare cross-linked enzyme aggregates. *Biotechnol. Bioeng.* **2004,** *86*, 273–276.

46. Pchelintsev, N. A.; Youshko, M. I.; Svedas, V. K. Quantitative characteristic of the catalytic properties and microstructure of cross-linked enzyme aggregates of penicillin acylase. *J Mol Catal B.* **2009**, *56*, 202–207.

47. Mateo, C.; Palomo, J. M.; Fernandez-Lorente, G.; Guisan, J. M.; Fernandez-Lafuente, R. Improvement of enzyme activity, stability and selectivity via immobilization techniques. *Enzyme Microb. Technol*. **2007,** *40*, 1451–1463.

48. Hernandez, K.; Fernandez-Lafuente, R. Control of protein immobilization: Coupling immobilization and site-directed mutagenesis to improve biocatalyst or biosensor performanceReview Article. *Enzyme Microb. Technol*. **2011,** *48*, 107–122.

49. Laporte, L. D.; Rea, J. C.; Shea L. D. Design of modular non-viral gene therapy vectors. *Biomaterials.* **2006,** *27*, 947-954.

50. Liu, G. J.; Ma, S. B.; Li, S. K.; Cheng, R.; Meng, F. H.; Liu H. Y.; Zhong, Z. Y. The highly efficient delivery of exogenous proteins into cells mediated by biodegradable chimaeric polymersomes. *Biomaterials*. **2010,** *31*, 7575-7585.

51. Pedraza, C. E.; Bassett, D. C.; McKee, M. D.; Nelea, V.; Gbureck, U.; Barralet, J. E. The importance of particle size and DNA condensation salt for calcium phosphate nanoparticle transfection. *Biomaterials.* **2008,** *29*, 3384-3392.

52. Felgner, P. L.; Ringold, G. M. Cationic liposome-mediated transfection. *Nature.*

1989, *337,* 387-388.

53. Li, W.; Nicol, F.; Szoka; F.C.; GALA: a designed synthetic pH-responsive amphipathic peptide with applications in drug and gene delivery, *Adv. Drug Deliv.Rev.* **2004,** *56,* 967–985.

54. Condreay, J. P., Witherspoon, S. M., Clay, W. C., and Kost, T. A. Transient and stable gene expression in mammalian cells transduced with a recombinant baculovirus vector. *Proc. Natl. Acad. Sci. U. S. A.* **1999,** *96,* 127-132.

55. Cone, R.D.; Mulligan, R.C. High-efficiency gene transfer into mammalian cells: generation of helper-free recombinant retrovirus with broad mammalian host range, *Proc. Natl. Acad. Sci. U.S.A.* **1984,** *81,* 6349–6353.

56. Yin, L. H.; Fu, S. Q.; Nanakorn, T.; Garcia-Sanchez, F.; Chung, I.; Cote, R.; Pissorno, G.; Hanania, E.; Heimfeld, S.; Crystal, R.; Deisseroth, A. Results of retroviral and adenoviral approaches to cancer gene therapy. *Stem Cells,* **1998,** *16,* 247–250

57. Liu, Q.; Muruve, D. A. Molecular basis of the inflammatory response to adenovirus vectors, Gene Ther. 10 (2003) 935–940Tomanin, R., and Scarpa, M. Why do we need new gene therapy viral vectors? Characteristics, limitations and future perspectives of viral vector transduction. *Curr. Gene Ther.* **2004,** *4,* 357-372.

58. Tomanin, R.; Scarpa, M. Why do we need new gene therapy viral vectors? Characteristics, limitations and future perspectives of viral vector transduction. *Curr. Gene Ther.* **2004,** *4,* 357-372.

59. Guignet, E. G.; and Meyer, T. Suspended-drop electroporation for high-throughput delivery of biomolecules into cells. *Nature methods,* **2008,** 5, 393-395.
60. Wang, H.Y.; Lu, C. Electroporation of Mammalian Cells in a Microfluidic Channel with Geometric Variation. *Anal. Chem.* **2006**, *78,* 5158-5164.

61. Kim, J. A.; Cho, K.; Shin, M. S.; Lee, W. G.; Jung, N.; Chung, C.; Chang, J. K. A novel electroporation method using a capillary and wire-type electrode. *Biosensors and Bioelectronics*. **2008**, *23*, 1353–1360.

62. Ganatella, P. J.; Karr, J. F.; Petros, J. A.; Prausnitz, M. R. Quantitative Study of Electroporation-Mediated Molecular Uptake and Cell Viability. *Biophysical Journal.* **2001**, *80,* 755-764.

63. Movahed, S.; Li, D. Microfluidics cell electroporation. *Microfluid Nanofluid.* 2011, *10,* 703–734.

64. Dower, W. J.; Miller, J.; Ragsdale C. W. High efficiency transformation of E.coli by high voltage electroporation. *Nucleic Acids Research.* **1988,** *16,* 6127-6145.

65. Lin, Y.; Li, M.; Wu, C. Simulation and experimental demonstration of the electric field assisted electroporation microchip for in vitro gene delivery enhancement. *Lab Chip*, **2004,** *4*, 104–108.

66. Ishibashi, T.; Takoh, K.; Kaji, H.; Abe, T.; Nishizawa, M. A porous membrane-based culture substrate for localized in situ electroporation of adherent mammalian cells. *Sensors and Actuators B*, **2007,** *128*, 5-11.

67. Walsh, G. Biopharmaceutical benchmarks 2010. *Nat. Biotechnol.* **2010**, *28*, 917–924.

68. Leader, B.; Baca, Q. J.; Golan, D. E. Protein therapeutics: a summary and pharmacological classification. *Nature* **2008**, *7*, 21-39.

69. Pavlou, A. K.; Reichert, J. M. Recombinant protein therapeutics-success rates, market trends and values to 2010. *Nat. Biotechnol.***2004**, *22*, 1513–1519.

70. Ghosh, R.; Cui, Z.F. Protein purification by ultrafiltration with pre-treated membrane. *Journal of Membrane Science* **2000,** *167*, 47–53.

71. Uedaa, E.K.M.; Goutb, P.W.; Morgantia, L. Current and prospective applications of metal ion–protein binding. *Journal of Chromatography A.* **2003,** *988*, 1-23.

72. Luo, Q.; Zou, H.; Xiao, X.; Guo, Z.; Kong, L.; Mao, X. Chromatographic separation of proteins on metal immobilized iminodiacetic acid-bound molded monolithic rods of macroporous poly(glycidyl methacrylate–co-ethylene dimethacrylate). *Journal of Chromatography A.* **2001,** *926*, 255–264.

73. Cheang, B.; Zydney, A. L. A two-stage ultrafiltration process for fractionation of whey protein isolate. *Journal of Membrane Science.* **2004,** *231*, 159-167.

74. Zydney, A. L. Protein Separations Using Membrane Filtration: New Opportunities for Whey Fractionation. *International Dairy Journal.* **1998,** *8*, 243-250.

75. Osmanbeyoglua, H. U.; Hurb, T. B.; Kimb, H. K. Thin alumina nanoporous membranes for similar size biomolecule separation. *Journal of Membrane Science.* **2009**, *343*, 1-6.

76. Savariar, E. L.; Krishnamoorthy, K.; Thayumanavan, S. Molecular discrimination inside polymer nanotubules. *Nature Nanotechnology.* **2008**, *3*, 112-117.

77. Huisman, I. H.; Prádanos, P.; Hernández, A. The effect of protein–protein and protein–membrane interactions on membrane fouling in ultrafiltration. *Journal of Membrane Science.* **2000,** *179*, 79-90.

78. Wu, J.; Gerstandt, K.; Zhang, H.; Liu, J.; Hinds, B. J. Electrophoretically induced aqueous flow through single-walled carbon nanotube membranes. *Nature Nanotechnology*. **2012,** *7*, 133-139.

79. Sun, X.; Su, X.; Wu, J.; Hinds, B. J. Electrophoretic Transport of Biomolecules through Carbon Nanotube Membranes. *Langmuir.* **2011,** *27*, 3150–3156.

80. Striemer, C. C.; Gaborski, T. R.; McGrath, J. L. Charge- and size-based separation of macromolecules using ultrathin silicon membranes. *Nature.* **2007,** *445*, 749-753.

81. Ghosh, R. Protein separation using membrane chromatography: opportunities and challenges. J. *Chromatogr., A.* **2002,** *952*, 13–27.

82. Hinds, B. J. Dramatic transport properties of carbon nanotube membranes for a robust protein channel mimetic platform. *Current Opinion in Solid State and Materials Science.* **2012,** *16*, 1–9.

83. Adebuer, A.; Chehimi, M. M.; Gallardo, I.; Pinson, J.; Vila, N. Electrochemical Oxidation of Aliphatic Amines and Their Attachment to Carbon and Metal Surfaces. *Langmuir*. **2004,** *20*, 8243-8253.

84. Dayel, M. J.; Hom, E. F. Y.; Verkman, A. S. Diffusion of Green Fluorescent Protein in the Aqueous-Phase Lumen of Endoplasmic Reticulum. *Biophysical Journal.* **1999,** *76*, 2843-2851.

85. Losic, D.; Cole, M.A.; Dollmann, B.; Vasilev, K.; Griesser, H. J. Surface modification of nanoporous alumina membranes by plasma polymerization. *Nanotechnology*. **2008**, 19-245704. p. 7

86. Adebuer, A.; Chehimi, M. M.; Gallardo, I.; Pinson, J.; Vila, N. Electrochemical Oxidation of Aliphatic Amines and Their Attachment to Carbon and Metal Surfaces. *Langmuir*. **2004,** *20*, 8243-8253.

87. Love, J. C.; Estroff, L. A.; Kriebel, J. K.; Nuzzo, R. G.; Whitesides, G. M. Self-Assembled Monolayers of Thiolates on Metals as a Form of Nanotechnology. *Chem. Rev.* **2005,** *105*, 1103−1169

88. Arnau, J.; Lauritzen, C.; Peterson, G. E.; Pedersen, J. Current strategies for the use of affinity tags and tag removal for the purification of recombinant proteins. *Protein Expression Purif.* **2006**, *48*, 1-13.

89. Leader, B.; Baca, Q. J.; Golan, D. E. Protein therapeutics: a summary and pharmacological classification. *Nature*. **2008**, *7*, 21-39.

90. Waegeman, H.; Soetaert, W. Increasing recombinant protein production in *Escherichia coli* through metabolic and genetic engineering. *J Ind Microbiol Biotechnol*. **2011**, *38*, 1891–1910

91. Terpe, K. Overview of tag protein fusions: from molecular and biochemical fundamentals to commercial systems. *Appl Microbiol Biotechnol*. **2003**, *60*, 523–533.

92. Porath, J. Immobilized metal ion affinity chromatography. Protein Expression and Purification. *Protein Expression and Purification*. **1992.** *3*, 263-281.

93. Janson, J. C. Protein purification: principles, high resolution methods, and applications. Vol. 151. John Wiley & Sons, **2012**.

94. Özkara, S.; Yavuz, H.; Denizli, A. Purification of immunoglobulin G from human plasma by metal-chelate affinity chromatography. *J. Appl. Polym. Sci*.**2003**. *89*, 1567-1572.

95. Zou, H.; Luo, Q.; Zhou. D. Affinity membrane chromatography for the analysis and purification of proteins. *J. Biochem. Biophys. Methods*. **2001**. *49*, 199-2240.

96. Clairbois, A.-S.; Letourneur, D.; Muller, D.; Jozefonvicz, J. High-performance affinity chromatography for the purification of heparin-binding proteins from detergent-solubilized smooth muscle cell membranes. *J. Chromatogr. B* **1998,** *706*, 55−62.

97. Charcosset, C. Purification of Proteins by Membrane Chromatography. *J. Chem. T echnol. Biotechnol.* **1998**, *71*, 95-110.

98. Thömmes, J.; Kula, M.-R. Membrane Chromatography—An Integrative Concept in the Downstream Processing of Proteins. *Biotechnol. Progr.* **1995,** *11*, 357-367.

99. Jain, P.; Sun, L.; Dai, J.; Baker, G. L.; Bruening, M. L. High-Capacity Purification of His-tagged Proteins by Affinity Membranes Containing Functionalized Polymer Brushes. *Biomacromolecules*, **2007,** *8*, 3102–3107.

100. Boi, C.; Cattoli, F.; Facchini, R.; Sorci, M.; Sarti, G. C. Adsorption of lectins on affinity membranes. *J. Membr. Sci.* **2006,** *273*, 12-19.

101. Chen, Z.; Chen, T.; Sun, X.; Hinds, B. J. Dynamic Electrochemical Membranes for Continuous Affinity Protein Separation. Advanced Functional Materials. **In press.**

102. Bao, J.; Chen, W.; Liu, T.; Zhu, Y.; Jin, P.; Wang, L.; Liu, J.; Wei, Y.; Li, Y. Bifunctional Au-Fe3O4 Nanoparticles forProtein Separation. *ACS Nano*. **2007,** *1*, 293-298

103. Lata, S.; Piehler, J. Stable and Functional Immobilization of Histidine-Tagged Proteins via Multivalent Chelator Headgroups on a Molecular Poly(ethylene glycol) Brush. *Anal. Chem.* **2005**, *77*, 1096-1105.

104. Zhang, C.; Griffith, B. R.; Fu, Q.; Albermann, C.; Fu, X.; Lee, I. K.; Li, L.; Thorson, J. S. Exploiting the Reversibility of Natural Product Glycosyltransferase-catalyzed Reactions. *Science* **2006**, 313, 1291-1294.

105. Zhang, C.; Albermann, C.; Fu, X.; Thorson, J. S. The in Vitro Characterization of the Iterative Avermectin Glycosyltransferase AveBI Reveals Reaction Reversibility and Sugar Nucleotide Flexibility. *J. Am. Chem. Soc*., **2006**, *128*, 16420–16421.

106 . Zhang, C.; Fu, Q.; Albermann, C.; Li, L.; Thorson, J. S. The In Vitro Characterization of the Erythronolide Mycarosyltransferase EryBV and Its Utility in Macrolide Diversification. *ChemBioChem* **2007**, *8*, 385 – 390.

107. Gantt, R.W.; Peltier-Pain, P.; Cournoyer, W. J.; Thorson, J. S. Using Simple Donors to Drive the Equilibria of Glycosyltransferase-catalyzed Reactions. *Nat. Chem. Biol.* **2011**, *7*, 685-691.

108. Riva, S. Laccases: Blue Enzymes for Green Chemistry. *Trends Biotechnol.* **2006**, *24*, 219-226.

109. Meynial, S. I.; Forchhammer, N.; Croux, C.; Girbal, L.; Soucaille, P. Evolution of A *Saccharomyces cerevisiae* Metabolic Pathway in *Escherichia coli*. *Metab Eng*. **2007**, *9*, 152-159.

110. Conrado, R. J.; Varner, J. D.; DeLisa, M. P. Engineering the Spatial Organization of Metabolic Enzymes: Mimicking Nature's Synergy. *Curr. Opin. Biotechnol*. **2008**, *19*, 492–499.

111. Liu, Y.; Du, J.; Yan, M.; Lao, M. Y.; Hu, J.; Han, H.; Yang, O. O.; Liang, S.; Wei, W.; Wang, H. *et al.* Biomimetic Enzyme Nanocomplexes and Their Use as Antidotes and Preventive Measures for Alcohol Intoxication. *Nat. Nanotechnol*. **2013**, *8*, 187-192.

112. Schoffelen, S.; Hest, J. C. M. Multi-Enzyme Systems: Bringing Enzymes Together in Vitro. *Soft Matter*. **2012**, *8*, 1736–1746.

113. Kristensen, C.; Morant, M.; Olsen, C. E.; Ekstrom, C. T.; Galbraith, D. W.; Moller, B. L.; Bak, S. Metabolic Engineering of Dhurrin in Transgenic Arabidopsis Plants with Marginal Inadvertent Effects on the Metabolome and Transcriptome. *Proc. Natl. Acad. Sci. U. S. A.* **2005**, *102*, 1779-1784.

114. Fierobe, H. P.; Bayer, E. A.; Tardif, C.; Czjzek, M.; Mechaly, A.; B éda ïch, A.; Lamed, R.; Shoham, Y.; B éda ïch, J. P. Degradation of Cellulose Substrates by Cellulosome Chimeras. Substrate Targeting versus Proximity of Enzyme Components. *J. Biol. Chem*. **2002**, *277*, 49621–49630.

115. Sheikh, F. G.; Pahan, K.; Khan, M.; Barbosa, E.; Singh, I. Abnormality in Catalase Import into Peroxisomes Leads to Severe Neurological Disorder. *Proc. Natl. Acad. Sci. U. S. A.* **1998**, *95*, 2961–2966.

116. Kholodenko, B. N.; Westerhoff, H. V.; Cascante, M. Effect of Channelling on the Concentration of Bulk-phase Intermediates as Cytosolic Proteins become More Xoncentrated. *Biochem J.* **1996,** *313*,921-926.

117. Gallego, F. L.; Dannert, C. S. Multi-Enzymatic Synthesis. *Curr. Opin. Chem. Biol.* **2010**, *14*, 174-183.

118. Mosbach, K.; Mattiasson, B. Matrix-Bound Enzymes. Part II: Studies on a Matrix-Bound Two-Enzyme-System. *Acta Chem. Scand*. **1970**, *24*, 2093-2100.

119. Mateo, C.; Chmura, A.; Rustler, S.; Rantwijk, F. V.; Stolz, A.; Sheldon, R. A. Synthesis of Enantiomerically Pure (S)-mandelic Acid using an Oxynitrilase–nitrilase Bienzymatic Cascade: A Nitrilase Surprisingly Shows Nitrile Hydratase Activity. *Tetrahedron: Asymmetry*, **2006**, *17*, 320–323.

120. Srere, P. A.; Mattiasson, B.; Mosbach, K. An immobilized Three-Enzyme System: A Model for Microenvironmental Compartmentation in Mitochondria. *Proc. Natl. Acad. Sci. U. S. A.* **1973**, *70*, 2534-2538.

121 . Kreft, O.; Prevot, M.; Mohwald, H. and Sukhorukov, G. B. Shell-in-Shell Microcapsules: A Novel Tool for Integrated, Spatially Confined Enzymatic Reactions. *Angew. Chem., Int. Ed*., **2007**, *46*, 5605–5608.

122. Chen, X.; Fang, J.; Zhang, J.; Liu, Z.; Shao, J.; Kowal, P.; Andreana, P.; Wang, P. G. Sugar Nucleotide Regeneration Beads (Superbeads): A Versatile Tool for the Practical Synthesis of Oligosaccharides. *J. Am. Chem. Soc.* **2001**, *123*, 2081-2082.

123. Nahalka, J.; Liu, Z.; Chen, X.; Wang, P. G. Superbeads: Immobilization in "Sweet" Chemistry. *Chem. Eur. J.* **2003**, *9*, 372-377.

124. Onda, M.; Lvov, Y.; Ariga, K.; Kunitake, T. Sequential Actions of Glucose Oxidase and Peroxidase in Molecular Films Assembled by Layer-by-Layer Alternate Adsorption. *Biotechnol. Bioeng.* **1996**, *51*, 163-167.

125. Lewis, S.R.; Datta, S.; Gui, M.; Coker, E.L.; Huggins, F. E.; Daunert, S.; Bachas, L.; Bhattacharyya, D. Reactive Nanostructured Membranes for Water Purification. *Proc. Natl. Acad. Sci. U. S. A.* **2011**, *108,* 8577-8582.

126 .Tanvir, S.; Pantigny, J.; Bounois, P.; Pulvin, S. Covalent Immobilization of Recombinant Human Cytochrome CYP2E1 and Glucose-6-phosphate Dehydrogenase in Alumina Membrane for Drug Screening Applications. *J. Membr. Sci.* **2009,** *329,* 85–90.

127. Oliveira, G. B.; Filho, J. L. L.; Chaves, M. E. C.; Azevedo, W. M.; Carvalho, L. B. Enzyme Immobilization on Anodic Aluminum Oxide/Polyethyleneimine or Polyaniline Composites. *React. Funct. Polym.***2008**, *68*, 27–32.

128. Milka, P.; Krest, I.; Keusgen, M. Immobilization of Alliinase on Porous Aluminum Oxide. *Biotechnol Bioeng.* **2000**, *69,* 344-348.

129. Gantt, R.W., Peltier-pain, P., Singh, S., Zhou, M., Thorson, J.S. Broadening the scope of glycosyltransferase-catalyzed sugar nucleotide synthesis. *Proc. Natl. Acad. Sci. USA*, **2013**, *110*, 7648-7653.

130. Sigal, G. B.; Bamdad, C.; Barberis, A.; Strominger, J.; Whitesides, G. M. A Self-Assembled Monolayer for the Binding and Study of Histidine-Tagged Proteins by Surface Plasmon Resonance. *Anal. Chem.* **1996**, *68,* 490-497.

131. Peltier-Pain, P.; Marchillo, K.; Zhou, M.; Andes, D. R.; Thorson, J. S. Natural Product Disaccharide Engineering through Tandem Glycosyltransferase Catalysis Reversibility and Neoglycosylation. *Org. Lett*. **2012**, *14,* 5086-5089.

132. Losey, H. C.; Jiang, J.; Biggins, J. B.; Oberthür, M.; Ye, X.Y.; Dong, S. D.; Kahne, D.; Thorson, J. S.; Walsh, C. T. Incorporation of glucose analogs by GtfE and GtfD from the Vancomycin Biosynthetic Pathway to Generate Variant Glycopeptides. *Chem. Biol.* **2002**, *9*, 1305-1314.

133. Bolam, D.N.; Roberts, S.; Proctor, M.R.; Turkenburg, J. P.; Dodson, E. J.; Martinez-Fleites, C.; Yang, M.; Davis, B.G.; Davies, G.J. The Crystal Structure of Two Macrolide Glycosyltransferases Provides a Blueprint for Host Cell Antibiotic Immunity. *Proc. Natl. Acad. Sci. U. S. A.* **2007**, *104,* 5336 –5341.

134. Biggins, J. B.; Onwueme, K.C.; Thorson, J. S. The Mechanism of CalC: Resistance to Enediyne Antitumor Antibiotics by Self-sacrifice. *Science* **2003,** *301,* 1537-1541.

135. Singh, S.; Hager, M. H.; Zhang, C.; Griffith, B. R.; Lee, M. S.; Hallenga, K.; Markley, J. L.; Thorson, J. S. Structural Insight into the Self-sacrifice Mechanism of Enediyne Resistance. *ACS Chem. Biol.* **2006**, *1*, 451-460.

136. Porter, D. L.; Levine, B. L.; Kalos, M.; Bagg, A.; June, C. H. Chimeric Antigen Receptor–Modified T Cells in Chronic Lymphoid Leukemia. *New England J. of Medicine*; **2011,** *365*,725-733.

137. Lin, Y.; Li, M.; Wu, C. Simulation and experimental demonstration of the electric field assisted electroporation microchip for in vitro gene delivery enhancement. *Lab Chip*, **2004,** *4*, 104–108.

138. Zhan, Y.; Wang, J.; Bao, N.; and Lu C. Electroporation of Cells in Microfluidic Droplets. *Anal. Chem.* **2009,** *81*, 2027–2031.

139. Lu, H.; Schmidt, M. A.; Jensen, K. F. A microfluidic electroporation device for cell lysis. *Lab Chip,* **2005,** *5*, 23–29.

140. Fox, M. B.; Esveld, D. C.; Valero, A.; Luttge, R.; Mastwijk, H. C.; Bartels, P. V.; Berg, V. D.; Boom, R. M. Electroporation of cells in microfluidic devices: a review. *Anal Bioanal Chem*, **2006,** *385*, 474–485.

141. Geng, T.; Zhan, Y.; Wang, J.; Lu, C. Transfection of cells using flow-through electroporation based on constant voltage. *Nature protocols*. 2011, *6*, 1192-1208.

142. Sunkara, V.; Park, D. K.; and Cho, Y. K. Versatile method for bonding hard and soft materials. *RSC Advances*, **2012,** *2*, 9066–9070.

143. Corovic, S.; Zupanic, A.; Miklavcic, D. Numerical modeling and optimization of electric field distribution in subcutaneous tumor treated with electrochemotherapy using needle electrodes. *IEEE TRANSACTIONS ON PLASMA SCIENCE*. **2000,** *36*, 1665-1672.

144. Wang, H.; Lu, C. Microfluidic electroporation for delivery of small molecules and genes into cells using a common DC power supply. *Biotechnology and Bioengineering.* **2008**, *100*, 579-586.

145. Polson, N. A.; Hayes, M.A. Electroosmotic Flow Control of Fluids on a Capillary Electrophoresis Microdevice Using an Applied External Voltage. *Anal. Chem*. **2000**, *72*, 1088-1092.

146. Geng, T.; Zhan, Y.; Wang, H. Y.; Witting, S. R.; Cornetta, K. G.; Lu, C. Flow-through electroporation based on constant voltage for large-volume transfection of cells. *Journal of Controlled Release*. **2010,** *144*, 91–100.

VITA

Zhiqiang Chen was born in Putian China. He completed his high school from Daji Middle School, Putian in 2006. He obtained his bachelor degree (Pharmaceutical Engineering) from Tianjin University in 2010. Right after he got his bachelor degree, he joined Dr. Hinds' group in the University of Kentucky for Ph.D study.

Publications

1. Dynamic Electrochemical Membranes for Continuous affinity protein separation. Z. Chen, T. Chen, X. Sun and B.J. Hinds. *Advanced Functional Materials,* **2014,** 24, 4317-4323.
2. A functionalized Anodic Aluminum Oxide Membrane-electrode System for Enzyme Immobilization. Z. Chen, J. Zhang, S, Singh, J. S. Thorson, and B.J. Hinds. *ACS Nano,* **In press**
3. Fouling Characteristics and Electrochemical Recovery of Carbon Nanotube Membranes. X. Sun, J. Wu, Z. Chen, X. Su and B.J. Hinds, *Advanced Functional Materials*, **2013**, 23(12), 1500-1506.
4. Single-step electrochemical functionalization of double-walled carbon nanotube membranes and the demonstration of ionic rectification. X. Zhan, J. Wu, Z. Chen and B.J. Hinds, *Nanoscale Research letters*, **2013**, 8, 279.
5. Flow-through Electroporation of large-scale HL-60 Cell Suspensions using Nanoporous Membrane Electrodes. Z. Chen, H. Sapper, M. Akenhead, X. Sun, H. Shin and B.J. Hinds. *Biotechnology&Bioengineering,* **to be submitted**
6. Numerical study of Two-step Continuous Affinity Protein Separation with Nanometer-Scale Membrane Electrode Systems. Z. Chen, A. Fox, C. Richards and B.J. Hinds, **In preparation**